SPECTROSCOPIC PROPERTIES OF SELF-ASSEMBLED LATERAL QUANTUM DOT MOLECULES

by

Xinran Zhou

A dissertation submitted to the Faculty of the University of Delaware in partial fulfillment of the requirements for the degree of Doctor of Philosophy in Materials Science and Engineering

Spring 2015

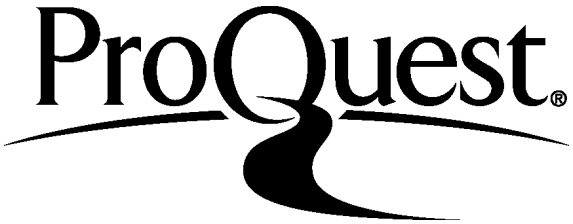

SPECTROSCOPIC PROPERTIES OF SELF-ASSEMBLED LATERAL QUANTUM DOT MOLECULES

by

Xinran Zhou

Approved: _____

Darrin Pochan, Ph.D.
Chair of the Department of Materials Science and Engineering

Approved: _____

Babatunde Ogunnaike, Ph.D.
Dean of the College of Engineering

Approved: _____

James G. Richards, Ph.D.
Vice Provost for Graduate and Professional Education

I certify that I have read this dissertation and that in my opinion it meets the academic and professional standard required by the University as a dissertation for the degree of Doctor of Philosophy.

Signed: _____

Matthew Doty, Ph.D.
Professor in charge of dissertation

I certify that I have read this dissertation and that in my opinion it meets the academic and professional standard required by the University as a dissertation for the degree of Doctor of Philosophy.

Signed: _____

Robert Opila, Ph.D.
Member of dissertation committee

I certify that I have read this dissertation and that in my opinion it meets the academic and professional standard required by the University as a dissertation for the degree of Doctor of Philosophy.

Signed: _____

Juejun Hu, Ph. D.
Member of dissertation committee

I certify that I have read this dissertation and that in my opinion it meets the academic and professional standard required by the University as a dissertation for the degree of Doctor of Philosophy.

Signed: _____

Dennis Prather, Ph. D.
Member of dissertation committee

ACKNOWLEDGEMENTS

Five years ago, when I just came to University of Delaware, I basically know nothing about the realm of quantum physics. After five-years' study, I still know very little, compared with the big world of knowledge. I clearly remember the first time when I start to read articles about quantum dot molecules. The feeling of confused and panic is still like yesterday. However, I got the most precious gift in my PhD track. I understand that as a small and meaningless component in the world, I do have the ability to improve the world a little bit, and I do not need to be scared or feel shame about my ignorance. I become stronger because all of you. You made my life shinning every day.

I would like to express my deepest appreciation to my advisor Dr. Matthew Doty. You are an awesome person, a true mentor and a role model of my scientific career and life. I used to feel that I can never be a person who really enjoy her work. But now it is no doubt that I am the top 0.1% happiest PhD in the world, because I wisely joined your team five years ago. You not only patiently lead me through every obstacle of my research, but also give me constructive advice when I get confused in my life. I hope I can transfer this energy to my future student or employee, without any lose.

I would also like to thank my committee member: Dr. Robert Opila, Dr. Juejun Hu and Dr. Dennis Prather. Every committee meeting brings us new directions of our research. Thanks a lot for sharing your advice, experience and idea with me. I also want to say thanks to Dr. Bruce Chase and the magic box: you are the king of optic experiments.

I also greatly appreciate my group members: Dr. Weiwen Liu, Dr. Diane Seller, Dr. Chelsea Haughn, Laura Vanderhoef, Xiangyu Ma, Eric Chen, Anagha Kulkarni,

and Evan Sinicin. It has been a lot of fun to work with you guys. I am proud to be a part of this team. Thanks for the caring and help from Kjeld and other folks work in nanofab. I will never forget to thank my dear ARS close-cycled cryostat. Thank you for running tens thousands of hours. Please be nice to the next person work with you.

Many thanks to all my friends in UD. I will try to draft a list in appendix.

Finally I would like to thank the most special persons in my life. Xueqi, your suddenly panic attack during the dissertation writing encouraged me to start drafting my own dissertation. Ning, you were my tutor when I first started doing research; you were my best partner when I were struggling all night in the lab; you were my shrink when I were driven crazy by the frustrations during work. Whenever I need someone in my life, I know you will be there. Dad and mom, I know you will always be by my side, no matter how far away we are.

TABLE OF CONTENTS

LIST OF TABLES

LIST OF FIGURES

ABSTRACT

In the 20^{th} century the first transistor was invented and the first computing device based on it was built. Since then, people have been looking for various ways to reduce the size and cost of the electronic devices used in computers, cell phones and other electronic products. When the feature sizes of these devices reach the nanometer scale, the deterministic properties of materials are replaced by the uncertainty caused by quantum effects. This brings challenges to the improvement of traditional devices but also presents opportunities for the development of electronics based on quantum mechanics. Quantum dots (QDs), semiconductor materials with quantum confinement in all three dimensions, are a very important material platform for the implementation of quantum mechanical devices.

III-V semiconductor self-assembled quantum dot molecules (QDMs), consisting of two closely-spaced QDs, are of great interest as potential components for next-generation optoelectronic devices. One of the attractive features of QDMs is the ability to manipulate, *in-situ*, the formation of delocalized molecular states with unique optoelectronic and spin properties. The structure, geometry and compositional profile of a QDM together determine the electronic and optical properties of that QDM. Lateral QDMs (LQDMs), in particular, consist of two or more QDs placed close to each other with a molecular axis perpendicular to the growth direction of the heterostructure, creating a QD complex structure with outstanding properties. LQDMs have good scalability and provide the opportunity to independently control charge occupancy and quantum coupling. LQDMs grown by molecular beam epitaxy (MBE) using partial GaAs capping and *in-situ* annealing of single InAs QDs create LQDMs with a small inter-dot spacing and relatively homogeneous geometry. However, there has been substantially less work on LQDMs than in Vertical QDMs (VQDMs) because

the growth control in LQDMs is less precise and the energy level structure in LQDMs is more complex than in VQDMs.

This dissertation focuses on the spectroscopic characterization of the optoelectronic properties of these LQDMs under electric and magnetic fields. It covers the experimental and theoretical foundation of the energy structure and optical properties of LQDMs and techniques for manipulating the delocalized states in a single LQDM. In chapter 5, a quantitative study of Coulomb interactions and charging effects in the LQDMs' ground states, combining both experimental and theoretical results. By measuring the photoluminescence (PL) emitted by LQDMs as a function of both electric field along the growth direction and excitation laser power density we verify the existence of delocalized molecular ground states under certain charge occupation. In chapter 6 I present results and analysis that experimentally verify the existence of delocalized molecular states in the first excited electron states of InGaAs LQDMs. In chapter 7 I report the behavior of single LQDM photoluminescence from different charge states and energy shells as a function of applied magnetic field. The paramagnetic shift in the first excited states of LQDMs and the variation of g-factors in different charge states suggests the electrons in the excited states can be localized in individual dots by the magnetic fields. In chapter 8, I proposed a design for a four-terminal device, in which a controllable vector electric field (including electric fields along and perpendicular to the growth direction of the LQDMs) can be applied.

Chapter 1

QUANTUM DOTS AND THEIR APPLICATIONS

1.1 Quantum Dots

Since the late 19^{th} century, the development of semiconductors has been one of the greatest driving forces in the progress of human civilization. The special energy structure of semiconductors, with gaps between conduction and valence bands, has enabled various applications such as transistors, light-emitting diodes (LEDs), solar cells and many other optoelectronic devices that are being widely used. By combining semiconductors with different bandgaps together, people can tailor the band structure of the resulting heterostructures and implement functions that cannot be realized by traditional materials. With the improvement of fabrication technology, novel devices have been developed from heterostructures at the nanoscale including super lattices, nanowires, and quantum dots (QD). QDs and their size effects were first discovered in 1981 by Ekimov et al. in solids.[20] In 1983, Brus et al. discovered the same phenomena in colloidal QDs system.[21] In the beginning of the 21^{st} century, the commercialization of ensemble QD-based devices began and continues to move forward towards applications at the single dot level.

A quantum dot is a semiconductor material whose charge carriers are confined in all three spatial dimensions by a surrounding material with a higher band gap. The three dimensional confinement leads to discrete energy levels exactly following the standard "particle in a box" model of quantum mechanics. Because of these discrete energy levels, QDs are often referred to as "artificial atoms." The energy levels of the QDs can be controlled by growth conditions and subsequent processing that alters the dimensions and geometry of the QDs. Because of this control, the optoelectronic properties of QDs can be tailored for different device applications.

A schematic plot of the energy structure of a QD is shown in Fig. 1.1 (a) and (b). When the QD material (e.g. InAs) is surrounded by a material with larger band gap (e.g. GaAs), charges are confined in a three-dimensional potential well. Additional growth techniques that alter the size of the QD [7, 8] can be used to control the confined energy levels. The smaller the QD, the larger the gap between the confined states of the conduction band and valance band within the QD.

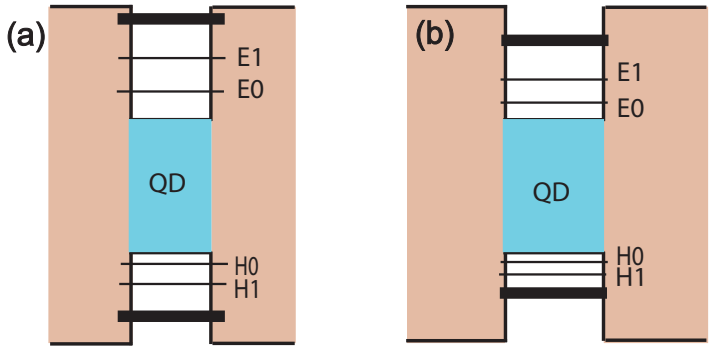

Figure 1.1: The energy structure of QDs of different size. A smaller QD (a) will have larger energy difference between quantized electron and hole states.

The energy states of QDs can be characterized with steady-state photoluminescence (PL), absorption, reflection and PL excitation spectroscopy. Time-resolved PL spectroscopy can be used to investigate the dynamics of charge-carrier excitation, tunneling, and relaxation within the QDs. As shown in Fig. 1.2 (b), the PL spectrum of a single QD shows discrete lines characteristic of the confined energy states. In an ensemble of QDs, the PL spectrum consists of broad peaks with a full width at half maximum (FWHM) of a few tens of meV (Fig 1.2 (a)). This broadening is a consequence of the inhomogeneous distribution in QD size, strain, and alloy composition inherent to QD growth.

1.2 Different Types of Quantum Dots and their Applications

There are several types of quantum dots which are produced by various methods. Applications of quantum dots range from quantum computing devices to biological

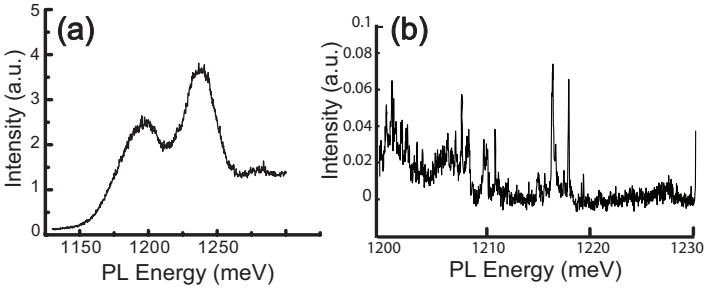

Figure 1.2: The PL spectrum of ensemble (a) and individual (b) QDs.

trackers based on their forms and properties. Solid state quantum dots are produced by either a bottom-up process such as self-assembly (resulting in self assembled QDs, SADs) or a top-down process such as lithography. These solid state quantum dots have potential for the study and application of single QDs. On the other hand, quantum dots produced by colloidal synthesis have attracted more attention in the area of biomedicine and energy harvesting as quasi-bulk materials with tunable band gaps.

1.2.1 Colloidal quantum dots

Chemical synthesis is one of the most simple approaches to producing QDs in colloidal form. The chemical precursors in a solution are decomposed during heating and nucleate into colloidal nanoparticles. The most crucial aspect for synthesis of colloidal QDs is controlling the nucleation time in order to produce QDs with desirable sizes and well defined, monodisperse bandgaps. An example is shown in Figure 1.3: with a nuclearation time difference of seconds, we can synthesis QDs with emission wavelength ranges all over the visible spectrum.

The controllable bandgaps in colloidal QDs offers full-spectrum photon harvesting and emission, which can be widely applied in optoelectronic devices such as light emitting diodes[22], photovoltaic devices[23], photo-detectors[24], biological sensors[25] and field-effect transistors[26]. The low-cost and relatively easy processing also makes the research and commercialization of colloidal QDs very accessible.

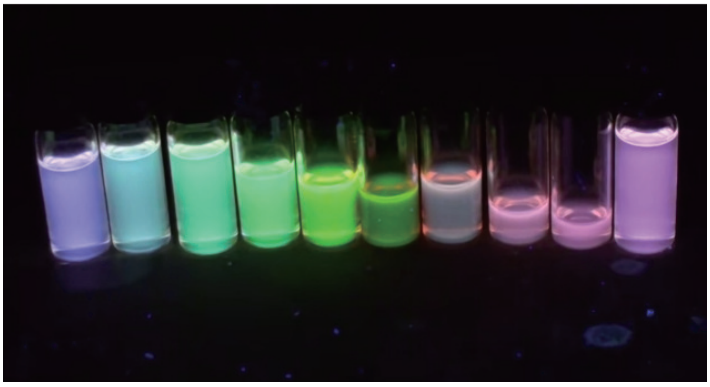

Figure 1.3: Colloidal CdSe QDs synthesized with nucleation time difference of seconds.[1]

Although the synthesis is relatively straight forward, colloidal quantum dots have more defects and surface states than self-assembled QDs, which can quench luminescence and charge mobility. Furthermore, the lack of precise control during the synthesis of QDs also increases the size distribution in the colloidal QDs. This make them a more complex system for fundamental research, especially for single QD applications or quantum information processing. To enhance the localization of electron-hole pairs and passivate the surface states of the colloidal QDs, overcoated shell layers of wide-bandgap materials surrounding the QDs are commonly applied.[27] Another effect in colloidal QDs that influences performance is the "blinking" of the photoluminescence emission of single quantum dots. The blinking is also related to surface states and similar core-shell structures can substantially suppress the blinking.

1.2.2 Gate-defined quantum dots

Many developments in quantum information processing based on QDs has focused on GaAs-based gate-defined QDs (lithographic QDs). As is shown in Fig 1.4, this type of QD is fabricated from GaAs / AlGaAs heterostructures that are epitaxially grown[2]. A two-dimensional electron gas (2DEG) with thickness of a few nanometers is formed by doping an AlGaAs layer underneath the top surface of the wafer. A set

of metal gates are defined by electron-beam lithography on top of the heterostructures to apply a negative voltage that locally depletes the 2DEG in an area of a few tens of nanometers. This depletion provides the third-dimension of confinement to create a quantum dot whose quantum properties emerge when the temperature is well below 1 K. Lithography techniques can easily be used to create laterally-oriented pairs of these quantum dots.

Usually, quantum confinement and coupling in gate-defined QDs are studied via electronic transport properties such as current or the number of electrons in the QDs. The three-dimensional confinement makes it possible to detect and control individual spins. Moreover, the nanofabrication techniques used to create this type of QD can be scaled up to create more complex quantum circuits or spintronic devices. This leads to a series of different spintronic devices. However, these types of devices are not optically active because only electrons are spatially confined in three dimensions. Recently Schinner et al. reported the approach to confine an electron and hole in two separated quantum well layers of one gate-defined QDM, which realized optical excitation and emission in gate-defined QDs.[28]

Graphene QDs have recently attracted considerable attention as a new type of gate defined QD, [29, 30, 3] because of their very long spin-coherence time that arises due to the absence of hyperfine coupling and small spin-orbit coupling. These properties makes graphene QDs an excellent material for spin qubits. Defined by e-beam lithography, the graphene layer serves as both the QD and the electrodes. Gate-defined one-dimensional materials have also attracted broad attention[4]. By simply depositing multiple narrow gates perpendicular to the nanowires, controllably-coupled QD molecules can be achieved. (See Fig. 1.4.) Electrical measurements demonstrate the control over electron tunneling in such devices.

1.3 Self-assembled Quantum Dots and their Applications

The self-assembly process for preparing solid-state QDs is driven by the strain induced by the lattice mismatch of two different crystals. When a material with a

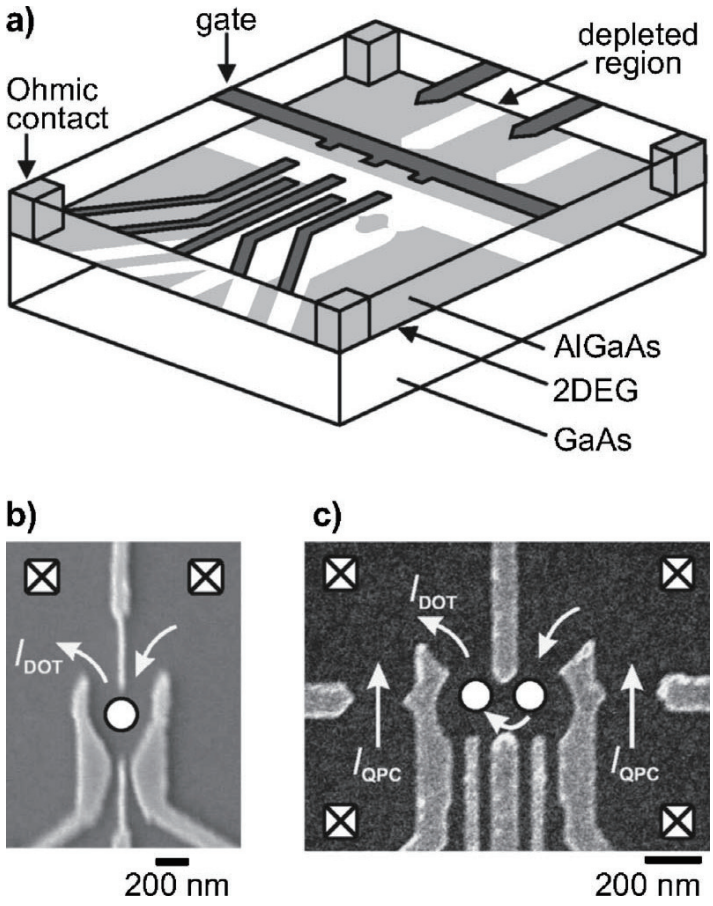

Figure 1.4: QD device defined by electrodes on top surface of GaAs/ AlGaAs 2DEG. (a) Schematic of the device. SEM image of (b) single-dot device and (c) double dot device.[2]

large lattice constant is deposited on a substrate with a smaller lattice constant, strain accumulates rapidly. When more than a few monolayers accumulate, an island of the large lattice constant material is generated in order to release the strain. Compared with the sol-gel process for producing colloidal QDs, self-assemby can produce QDs with controllable locations, better uniformity and fewer surface states, which makes them an ideal testbed for fundamental research into the physical properties of QDs. In chapter 3, a more detailed introduction to the QD self-assembly process by MBE is given.

Depending on the degree of lattice mismatch, the self-assembly technique can

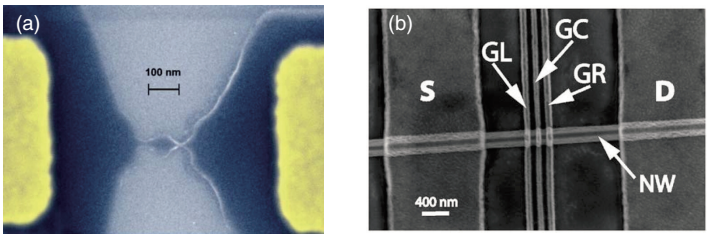

Figure 1.5: (a) One typical design for gate-defined graphene QDs. Dark areas are coverd by PMMA mask to protect graphene underneath from plasma etching. The yellow areas are Au/ Ti contacts.[3] (b) SEM image of gate-defined double QDs in InAs nanowire. The nanowire between source (S) and drain (D) ohmic contacts are isolated by three top gates (GL, GC and GR) into sections.[4]

be applied to many different systems. These include group IV materials (Si/Ge), group III-V materials (InAs/ GaAs, InAs/ InP, GaN/ AlN), and QDs grown in III-V nanowires. The advantage for self-assembled Ge/Si quantum dots is that they can utilize advanced Si-based technology for device integration. For the development of group III-V QD systems other than InAs/ GaAs, the most important driving force for research is choosing materials with different bandgaps or lattice mismatch, which can be utilized in laser emitters in blue (GaN/ AlGaN [31]) or infrared (InAs/ InP[32]) wavelengths. The self-assembled QDs embedded in nanowires also show outstanding performance as candidate single-photon emitters and nano-sensors. The nanowires serve as single-mode waveguides for the photon emitted from the QDs and enhance the efficiency of photon extraction[5] (See Fig 1.6).

To find a balance between controllable location and ease of optical manipulation, we focus specifically on epitaxially-grown QDs fabricated by InAs deposited on GaAs. The growth technique of such QDs has been well-established. The most exciting applications for InAs/GaAs QDs are in quantum information processing. The single spins of electrons[33, 34] or holes[35, 36] in such QDs have long been considered to be a promising candidate for quantum bits.

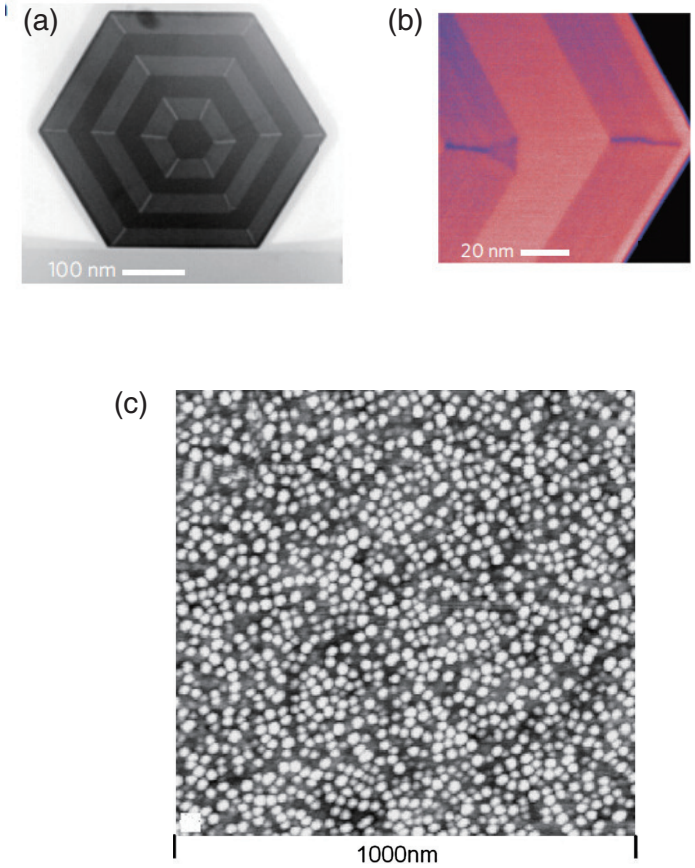

Figure 1.6: Different types of self-assembled QDs. (a) Cross-sectional image of AlGaAs multi-layer nanowires with QDs embedded. (b) Zoom-in of (a). The QDs are in the triangular zone[5]. (b) The AFM images of InAs QDs matched to InP (3 1 1)B substrate after deposition of 3.5 MLs InAs layers.

Chapter 2

QUANTUM CONFINEMENT AND COUPLING IN QUANTUM DOT MOLECULES

2.1 Confinement of Single Quantum Dots

When the motion of electrons and holes are confined in a semiconductor structure, their allowed energy levels are defined by the model of particles in a finite square potential well. We suppose the potential of the square well is V_0, which should be the band-edge difference between two semiconductor materials. We can describe the wavefunction of the charges ψ by Schrodinger's equation, as is represented below.

$$\begin{cases} E\psi(\mathbf{R}) = -\frac{\hbar^2}{2m}\frac{\partial^2\psi(\mathbf{R})}{\partial\mathbf{R}^2} + V_0\psi(\mathbf{R}) & \text{outside the well} \\ \\ E\psi(\mathbf{R}) = -\frac{\hbar^2}{2m}\frac{\partial^2\psi(\mathbf{R})}{\partial\mathbf{R}^2} & \text{inside the well} \end{cases} \tag{2.1}$$

where m is the effective mass of the charge carrier and $\mathbf{R}$ is the spatial location of the charge. The dimension of $\mathbf{R}$ depends on the dimension of the confinement. In a QD, the confinement is in all three spatial dimensions. To simplify the question, we start by solving the one-dimensional confinement problem and utilize it to qualitatively study the problem in a QD. Therefore, we use a scalar z to represent the spatial location in one dimension.

The wavefunction inside the well has form similar to an infinitely deep well. It can be written as

$$\psi(z) = C \begin{Bmatrix} cos \\ sin \end{Bmatrix} kz \tag{2.2}$$

where k is defined in terms of the energy $\epsilon = \hbar^2 k^2/2m$ and C is an arbitrary constant. Outside the well, $\psi(z)$ can be written as

$$\psi(z) = Dexp(\pm\kappa z) \tag{2.3}$$

. where κ is defined in terms of the energy $V_0 - \epsilon = \hbar^2\kappa^2/2m$ and D is an arbitrary constant. To solve these equations and find the allowed energy in this well, we need to consider two factors: 1) It must be possible to normalize this wavefunction and 2) The wavefunctions and their derivatives must be continuous at the edge of the well. Based on these requirements, we get a transcendental equation for k:

$$\left\{ \begin{matrix} tan \\ -cot \end{matrix} \right\} (ka/2) = \sqrt{\frac{2mV_0}{\hbar^2 k^2} - 1} \tag{2.4}$$

By solving this equation, the allowed bound states are found. (See Fig. 2.1) In a three-dimensional (3D) potential well system, the wavefunctions of the charges are a product of sine waves in each dimension. In the case of infinite potential wells, the energies can be given by

$$\varepsilon_{n_x,n_y,n_z} = \frac{\hbar^2\pi^2}{2m}(\frac{n_x^2}{a^2} + \frac{n_y^2}{b^2} + \frac{n_z^2}{c^2}) \tag{2.5}$$

Using similar methods to calculate energies in a one dimensional finite well, we can calculate the energies in such a 3D system with finite confinements. Both electrons and holes in a InAs QD are confined in this way. A schematic band diagram of type I and type II QDs is represented in Fig. 2.1. Most research has been focued on type I QDs in which electron and holes are confined in the same location. The strong overlap of electron and hole wavefunctions leads to a strong optical activity (i.e. absorption and emission). Type II QDs are fabricated by materials such as GaSb/GaAs and Si/Ge[37] in which the electron and holes are confined in different spatial locations. The lateral QDMs we studied are usually considered type I QDs but have some similarity to the type II system.

In the real world, the confinement in a self-assembled QD also depends on its morphology. For example, in the lateral direction, the confinement in the xy plane

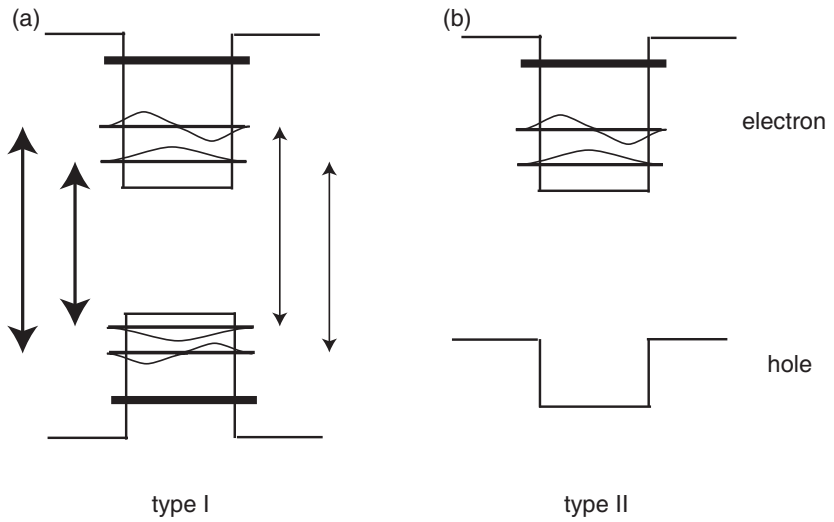

Figure 2.1: Schematic band diagram of (a) type I and (b) type II QDs. The wavefunctions of confined electron and hole energy states are also demonstrated. The width of the arrows between energy states in (a) indication the strength of the interband transition.

is more like a parabolic well. For a QD that has been through an In flush process for height truncation, the shape of the confinement in the growth direction will be more like a square well. The alloying during the growth, which modifies the barriers of the InAs/GaAs interface, should also be considered during the simulation of QD confinements [38].

The intraband spacing of the energy states increases when the size of the confinement decreases. In large heterostructures, the intraband energy level spacing is smaller than the energy available from the temperature, kT, and individual bands cannot be observed. When the energy level spacing exceeds the phonon energy at a specific temperature, the material will show quantum properties[6]. It is worth mentioning that the quantized bandgap can only been observed in semiconductors. In metals, the Fermi level lies in the center of a band, and this makes electrical and optical properties remain constant with the decrease of the particle size. A schematic illustration of the density of states in metal and semiconductor particles is shown in Fig. 2.2 (a).

Normally, the size effect is able to be observed when the particle sizes is smaller than the exciton Bohr radius of the QD materials. The exciton Bohr radius of bulk InAs is 35 nm, which is much larger than the vertical size of a normal self-assembled InAs QD. Fig. 2.2 (b) exhibits the densities of states in one band of a semiconductor as

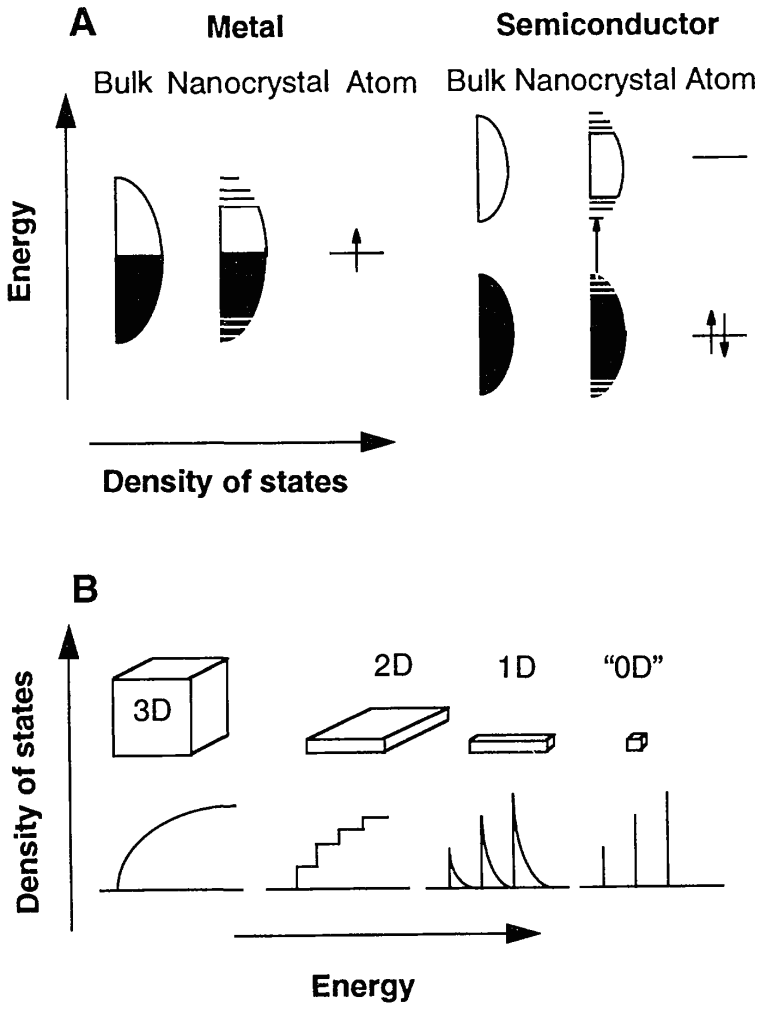

Figure 2.2: (a) Schematic of the density of states in metal and semiconductor nanoparticles. (b) Schematic of density of states as a function of dimension[6].

a function of dimension. The three-dimensional confinement in a QD makes its energy

states completely quantized, just like the orbitals in an atom. Since both electrons and holes are Fermions, according to the Pauli exclusion principle, each allowed energy state can be occupied by only two charges with opposite spin orientations. Therefore, there will be finite number of charges in a QD. However, the optical and electrical properties are especially sensitive to the number of charges in QDs because the tight confinement drastically increases the wavefunction overlap between charges. Utilizing these effects, QDs can be used to build transistors and memory storage devices[39, 40].

2.2 Optical Properties of Quantum Dots

The measurement of photoluminescence emission is one of the most convenient methods to detect the energy structure of QDs. A schematic that shows the mechanism for the emission of the photoluminescence in an InAs/GaAs QD is provided in Fig. 2.3. In a non-resonant photoluminescence excitation and emission process, electrons in bulk GaAs are excited and leave holes in the valence band of GaAs. Both carriers then relax into QDs, recombine and emit PL. The energy of the PL emitted from the QD is equal to the energy difference between the conduction and valence band states. The Hamiltonian of PL energies is the difference between the initial state and final state, which can be represented as:

$$H_{PL} = H_i - H_f \tag{2.6}$$

Under low excitation laser power, only the PL from the lowest unoccupied energy states can be observed. With increasing laser power, more excitons occupy the lowest energy levels and PL from the higher energies can also be observed. At cryogenic temperatures, the PL emitted from single QDs should be sharp and discrete peaks with linewidth much smaller than 1 meV.

2.2.1 Selection rules

The transition rates in different energy states in QDs can be derived from Fermi's golden rule, in which the intensity of optical transitions can be simplified to depend

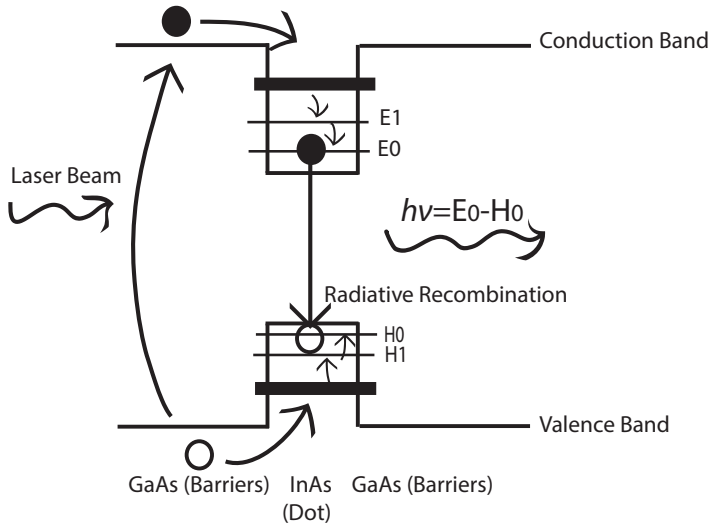

Figure 2.3: Schematic of the process of PL emission in QDs.

on a matrix element including the Bloch functions of different energy states. In an interband transition, the matrix element is

$$\int \phi_j^*(z)\phi_i(z)dz, \tag{2.7}$$

an integral over the product of the envelope functions of the conduction and valence bands. Note that the full matrix element includes the dipole operator, which is antisymmetric, and the Bloch functions for the electron and hole, which have opposite symmetry. This adds a constant term and thus the net matrix element is proportional only to the integral of envelope wavefunctions as shown in Equation 2.7. In a three-dimensional infinite square potential well, only transitions between electron and hole energy states with the same indexes ($\delta n = 0$) are allowed. Although this rule does not strictly apply to finite well models, the $\delta n = 0$ transitions still have the dominant. A more complete set of selection rules includes the fact that the interdot transition is allowed when the wavefunctions for both states have the same parity. A schematic is also shown in Fig. 2.1

On the other hand, the selection rules for intraband transitions (transitions

within conduction bands or within valence bands) is the opposite: the transition rate will be non-zero only if the parity of one state is even and the other odd. This is because the matrix elements for intraband transition is

$$< j|\hat{P}_z|i >= -i\hbar \int \phi_j^*(z)\frac{d}{dz}\phi_i(z)dz. \tag{2.8}$$

The momentum operator $\hat{p}$ is still antisymmetric, but the two Bloch states within a single band have the same parity.

The optical transitions in a real QD may break these selection rules because the QD geometry leads to wavefunctions that are not perfectly symmetrical. However, the allowed states as shown in the selection rules still strongly dominate. We usually do not consider the possible transitions that contradict the selection rules when analyzing the experimental results.

2.2.2 Photoluminescence perturbation from electric field

The influence of electric field in a QD system can be divided into two parts. First, the electric field tilts the shape of the confinement. As is shown in Fig. 2.4, this tilting will drive the electrons and holes in the QD to opposite sides. The change of PL energy caused by band bending driven by the electric field is called the Stark shift. In a QD, the energy of spectral lines normally shifts toward the low energy side with the increase of the electric field. The maximum separation between electrons and holes depends on the size of the confinement along the electric field. Because of the small size of the self-assembled QDs in the growth direction, the Stark shift caused by the vertical electric field are normally subtle. However, by applying electric field along the lateral direction, the energy can be tuned by the Stark effect over a relatively large range. Therefore, applying a local electric field in the planar direction might be a promising method to tune PL energies and overcome the non-uniformity of different self assembled QDs.[41]

Another feature is that self-assembled QDs can be grown on a doped substrate that can be used to inject charge carriers into the QDs and therefore cause Coulomb

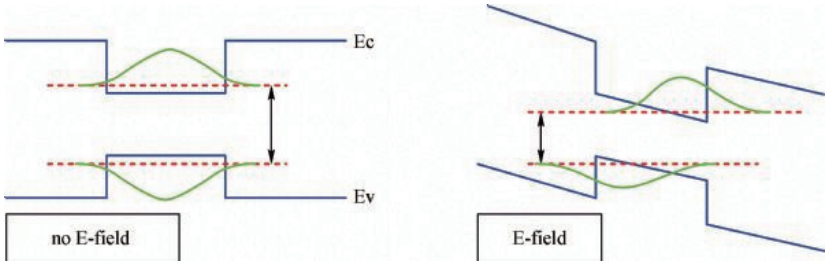

Figure 2.4: The band structure of a quantum well without (left) and with (right) electric field. The electric field tilts both the valence and conduction bands and lowers the energies of confined states for both electrons and holes. The shapes of the wavefunctions are also perturbed.[7]

forces to influence the excitons. The injection of charges will cause a sharp PL energy shift in the single QD PL, which is usually called a Coulomb shift. The direction of Coulomb shift depends on the net effect of the spectator charge carrier on the electron and hole in the exciton. Normally, the injection of one spectator electron will cause a red shift of 4-6 meV in the PL energy of a single QD relative to the emission energy of the neutral exciton containing only one electron and hole. This Coulomb shift is considered a fingerprint in the PL signature of single QDs.

A comprehensive study of the Coulomb shift and many-body interactions in single QDs has been done by Ediger, et al.[42] Fig. 2.5 (a) represents the PL energy shifts of a single QD as function of the voltage applied along the growth (vertical) direction. The vertical lines trace the Coulomb shift and mark the charging events. Based on the different possible spin interactions in the initial and final states, the PL energy from recombination between states with the same total charge occupation can be different, which is called fine structure splitting. Fig. 2.5 (b) and (c) shows the calculated PL spectra for charge states X- and X2-. It can be seen that the fine structure splitting in X2- is caused by the final states with different spin orientations.

When a QD complex includes two or more QDs, the charge occupation is determined by both Coulomb interaction and interdot coupling. A pronounced example is the PL of self-assembled vertical quantum dot molecules under an electric field applied

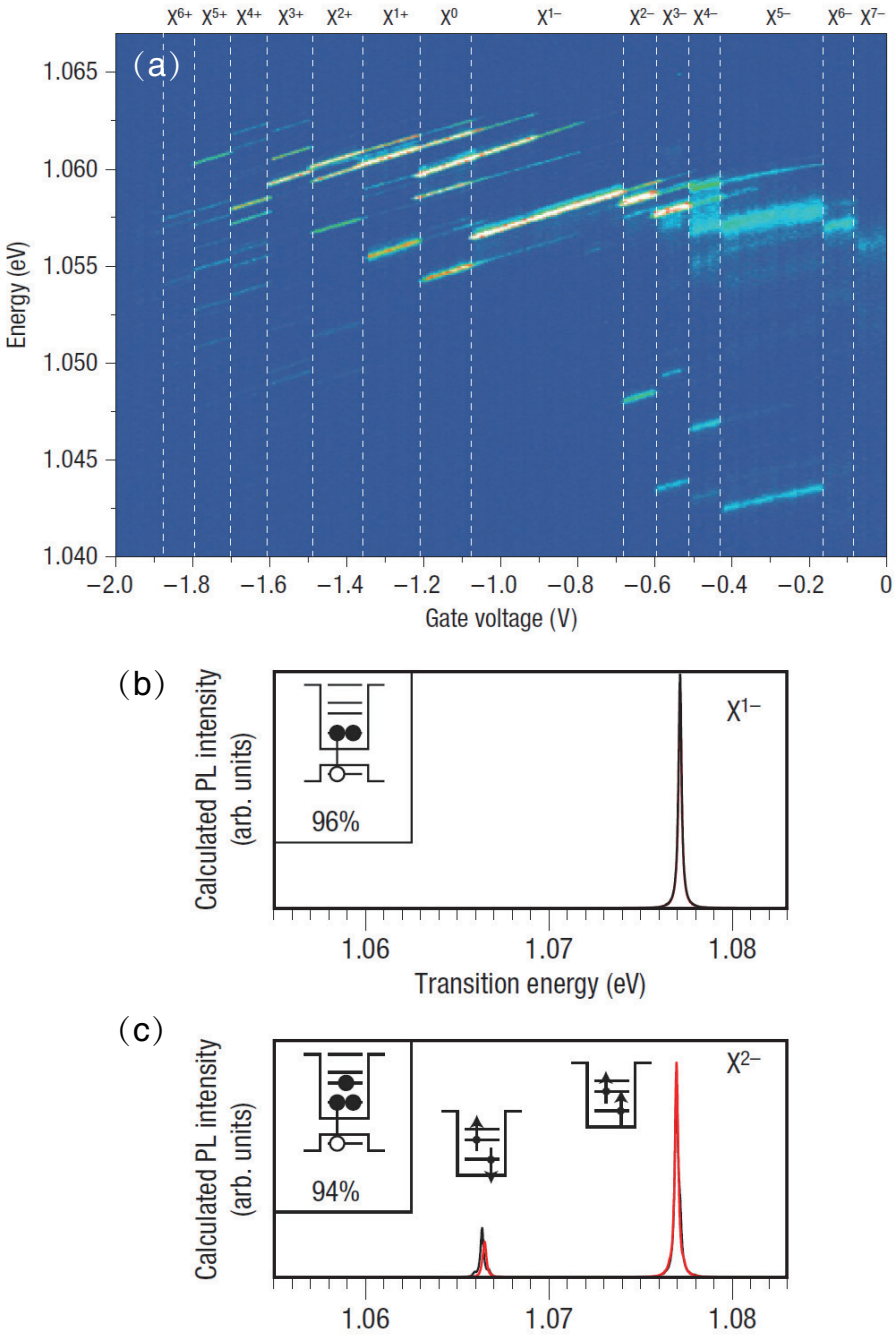

Figure 2.5: (a) PL energy as a function of voltage along the growth direction of a single QD. The intensity is represented with a color scale. The charging events are marked by vertical lines. The calculated PL spectra for X- and X2- states in a single cylindrical InAs QD is represented in (b) and (c) respectively. The insets show the configuration of the initial states and the charge carriers involved in the PL emissions. The black and red lines represent PL with different polarizations.[8]

along the growth direction. The electrons are injected into the QDs sequentially with the increase of the electric field. When the energy levels in two QDs are degenerate under the field, the electron (or hole) will be able to be delocalized over the two QDs. A more detailed discussion of the tunneling of charge carriers in QDM is provided in Sec. 2.3.

2.2.3 Photoluminescence perturbation from magnetic field

2.2.3.1 Zeeman splitting

Zeeman splitting is an effect that can be observed in quantum confined systems under applied magnetic field. At zero magnetic field, the energies of charge carriers with different non-zero spin states are degenerate. The spin "up" or "down" leads to a magnetic moment parallel or antiparallel to the magnetic field. The magnetic field will therefore split the energies of different spin orientations in initial and final states. In low magnetic field, Zeeman splitting can be observed as a doubled PL peaks with the energy difference linearly proportional to the static magnetic field. The perturbation of the PL emission energy, also referred to as the Zeeman splitting is

$$\Delta E_{Zeeman} = -\mu_B g_{ex} B \tag{2.9}$$

The strength of Zeeman splitting is determined by g_{ex}, which is an essential property of an electron-hole pair. g is the Lande g-factor, or dimensionless magnetic moment. g is typically viewed as a set property of a specific material, but in the case of QDs or QDMs it can be interpreted to arise from a weighted integral over the materials within the extension of the envelope wavefunction of charge carriers.[43] The g-factor for the spin of free electrons is 2. In a heterostructure, the g-factor influenced by factors such as spin-orbit coupling. The two PL emission lines associated with two Landau levels should be left or right-hand circularly polarized, respectively. In a QD with strong confinement, the strength of Zeeman splitting in different charge configurations should be basically the same because they are all determined by the difference of initial and final states, in which one electron and one hole are always included.[44] In the real

case, the charge occupation may influence the confinement in a dot and this will cause the g factors of excitons in different charge states to be different.

2.2.3.2 Diamagnetic shift

The charge carriers in free space orbit in the plane normal to **B** at a cyclotron angular frequency given by:

$$\omega_c = \left| \frac{eB}{m} \right| \tag{2.10}$$

With 3D confinement, the movement of charge carriers will be confined by both magnetic field and the heterostructure. For theoretical simplification, we usually model the lateral confinement in a single QD as a 2D parabolic well. This leads to the well-known Fock-Darwin energy spectrum, which shows that the direction of the diamagnetic shift in ground and excited shells have opposite direction in low magnetic field range [9], which is given by

$$H = -\frac{\hbar^2 \nabla^2}{2M} + \frac{1}{2}\omega_c L_z + \frac{1}{8} M \omega_c^2 r^2 \tag{2.11}$$

where M is the confined charge's mass, ω_c is the cyclotron frequency, Lz is the angular momentum in z direction and r is the radius of the wavefunction. The calculated Fock-Darwin spectrum have criss-cross patterns as is shown in Fig. 2.6[9]. Compared with the calculated Fock-Darwin spectrum in Fig. 2.6 (b), the experimental results show a signature with more complexity, which comes from the many-body interactions in the QDs.

The quadratic positive energy shift of the excitons in the ground states of the QDs is usually called the diamagnetic shift and is proportional to the area of the wave functions of charge carriers. Both theoretical and experimental evidence shows that the diamagnetic shift is strongly dependent on spectator charges[45] and the spatial confinement structure of QDs[46]. A reversal in sign of the conventional diamagnetic shift has been observed in type-II QD systems and type-I QDs with special charge configurations.

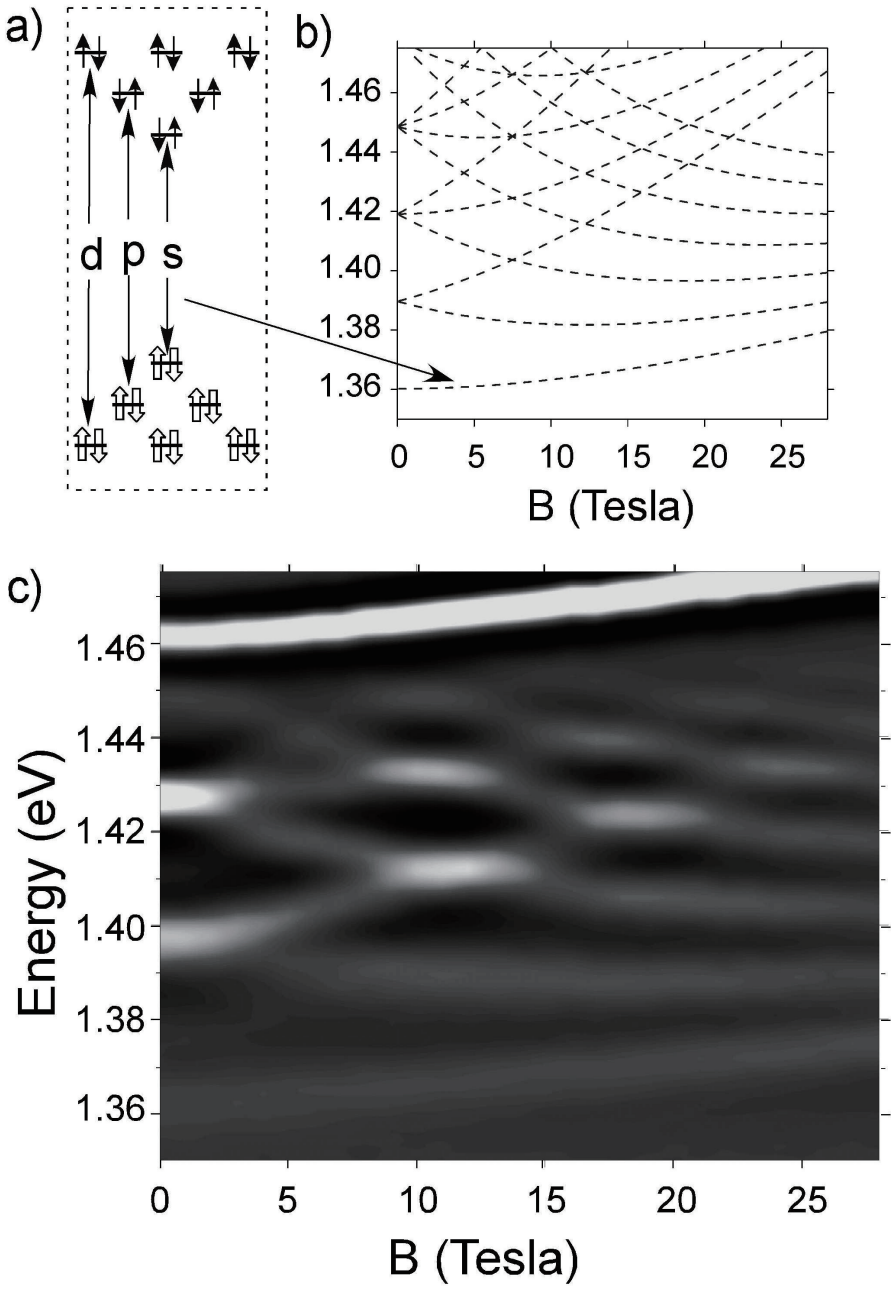

Figure 2.6: The computational Fock-Darwin spectrum (b) of a QD system as is schematically shown in (a). (c) shows the experimental results of a set of quasi-homogeneous QDs under magnetic fields, in which the Zeeman fine splitting is unable to be observed.[9]

Together with the Zeeman splitting, the PL energy E_{pl} under magnetic field of B can be fit by

$$E_{pl}(B) = E_{pl}(0) \pm 1/2\mu_B g_{ex} B + a_{ex} B^2 \tag{2.12}$$

where Epl(0) is the PL energy at 0 T, g_{ex} is the g factor of the exciton and a_{ex} is the diamagnetic coefficient of the exciton.

In a quantum ring system with magnetic field along the growth direction, the Aharonov-Bohm (A-B) effect is expected to be observed. Electrons are transferred through the different sides of a quantum ring structure and their phase-change rates will be increased or decreased by the magnetic field: this causes a phase difference of the electrons on the both sides of the ring that oscillates as a function of magnetic field. This effect has been observed in the quantum ring structures[47] and type-II quantum dots[48] as the oscillation of photon emission energy as a function of magnetic field.

2.3 Inter-dot Coupling in Quantum Dot Molecules

The most simple QD molecule (QDM) contains two coupled dots separated by a barrier. Because of the wavelike nature of the particles in quantum mechanics, the electrons or holes in one QD will be able to penetrate through the barrier and be trapped in the neighbor QD. The electron-hole recombination can happen to charges in the same dot or different dots. Recombination of an electron and hole in the same or different QDs are called direct and indirect transitions, respectively. The behavior of coupled QDMs is analogus to hydrogen molecules except for the fact that no two QDs are alike. The growth of self-assembled QDMs is driven by the lattice mismatch between two different materials. It is impossible to fully eliminate the inhomogeneity during the self-assembly and grow two identical QDs.

Krenner and Stinaff were the first to report observation of coupling in QDMs as a function of applied electric field,[49]. Subsequent reports from these same groups demonstrated that electric fields can be used to tune the energy levels of electron and hole states of vertically-stacked quantum dots in and out of resonance and that the presence of additional charges significantly alters the signatures of coupling due to both

Coulomb and spin interactions.[10, 43, 50, 51, 52] Fig. 2.7 schematically depict the idea of electrically controlling the interdot coupling for the hole states. To overcome the inhomogeneity of QDs, an electric field is usually applied *in-situ* along the molecular axis of QDMs to tune the different confined states of the two QDs relative to one another. Fig. 2.7 (c) shows the energy of the neutral exciton (X_0) as a function of applied electric field. With the increase of electric field, the recombination energy of the indirect transition will be altered linearly while the direct transition is perturbed very little.

When the electric field aligns the electron or hole states of the two QDs, the recombination energy of direct and indirect transitions should be indistinguishable and the coherent coupling in a QDM will be turned on. The molecular state is split into bonding and antibonding states with different parity in the wavefunction. These two states have an energy splitting δ that depends on the tunneling rate of charge carriers: the narrower the interdot barrier is, the larger the tunneling rate will be and the larger the energy splitting between the two states will be.

A signature called anticrossing, which occurs at F_{X^0} in Fig. 2.7 is the fingerprint of the coupling between two QDs. Anticrossing occurs when there is interaction between two states. For example, the Hamiltonian of initial states in the neutral exciton of vertical QDMs can be simply described as

$$H_{PL} = \begin{pmatrix} E_{X0} & -t_{X0} \\ -t_{X0} & E_{X0} + edF \end{pmatrix} \tag{2.13}$$

in the basis of the direct recombination and indirect recombination. E_{X0} represents the PL energy of direct recombination of neutral exciton, d is the distance between the two QDs and -t_{X0} is the tunneling rate. Because there are no charges in the final state, the PL signature of neutral exciton recombination is determined only by the energy of the initial state. For the trion states with one charge remaining in the final state, the tunneling in the final state also plays a role: the PL will include the anticrossing patterns in both initial and final states.

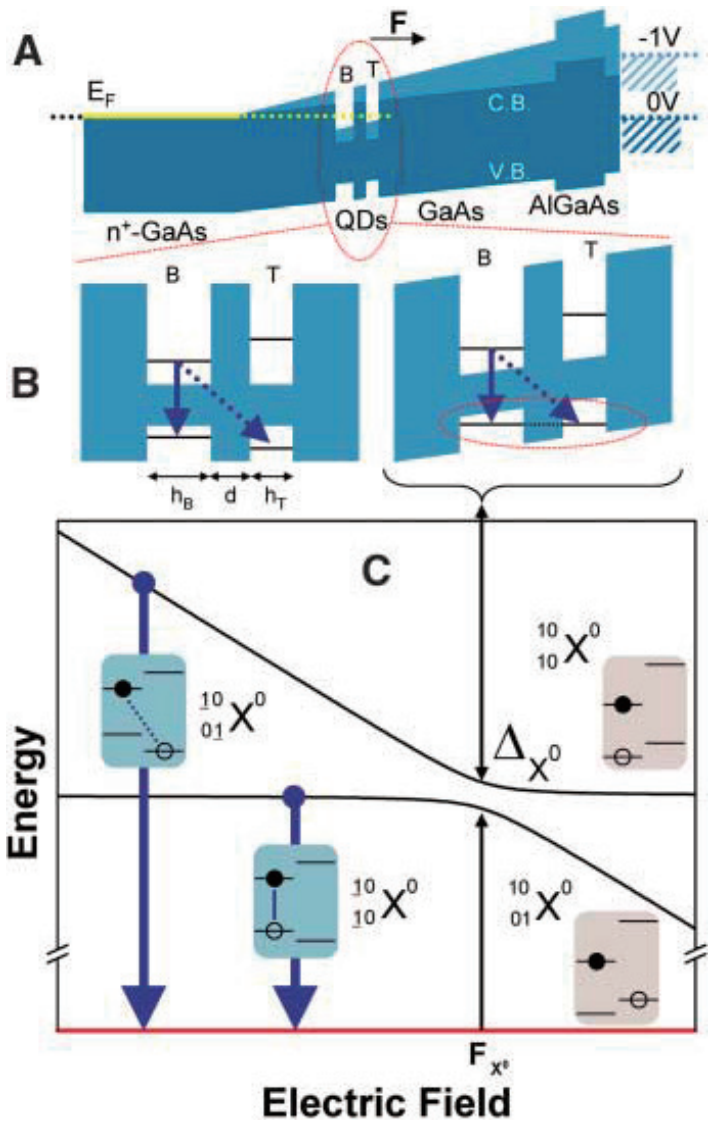

Figure 2.7: (a) Band diagram for the device that tune the energy levels in a VQDM by electric field in the molecular axis. (b)Schematic of the band diagram of the QDM when non-resonant (left) or resonant (right) coupling is occurred. (c) Schematic of the initial and final states of neutral exciton state in the QDM as a function of electric field.[10]

Chapter 3

INAS / GAAS QUANTUM DOTS MOLECULES

Developments in molecular beam epitaxy have enabled the growth of a variety of complex QD structures including quantum dot molecules[16], quantum rings[53] and quantum dot clusters[54]. Systems have been built with QDs spatially and energetically close to each other, in order to overlap the wavefunctions and enhance the controllable interaction between single QDs. The photon emission energies of indirect transitions in a complexes of QDs tune strongly with applied electric field because they involve electron and holes predominantly located in separated QDs. Among these structures, stacked vertical QD molecules (VQDMs), consisting of two QDs stacked along the growth direction, have drawn much attention [55, 52, 56, 57] because of the precise control over geometry available in the VQDM configuration and the potential applications in quantum information processing. On the other hand, laterally aligned QD molecules (LQDMs) provide opportunities to independently control the charging/ inter-dot coupling and potential scalability.

In this chapter, I introduced the growth mechanism of self-assembled InGaAs QDs, VQDMs and LQDMs. The research progress for different complexes of QDs and current interests in this field are also summarized.

3.1 InAs / GaAs Quantum Dots

3.1.1 Advantages of III-V self-assembled quantum dots

In the most simple system of self-assembled QDs, each single QD can be considered as an individual building block. In such a system, QDs are fabricated from one-step growth [58] and arbitrarily separated from each other spatially, They can also be deterministically located in a position fixed by nanofabrication processes before

growth, but numerous challenges to simultaneously controlling location and preserving high optical quality remain. Such QD materials can be utilized to build up devices such as light-emitting diodes, lasers, and single photon sources.

Compared with semiconductors in group IV, the III-V compounds have good electron mobility and luminescence efficiency. Because the zinc blend lattice structure in the III-V compound leads to stronger ionic character, the intrinsic mobilities of both electrons and holes in III-V materials are larger than Si, which makes them a better candidate for high-speed computation applications. Moreover, the direct bandgaps in III-V materials make them optically active, which makes them suitable for optoelectronic device applications and control operations within the spin coherence time via ultrafast optical fields. The optical activity opens up a large range of applications including lasers[59], single photon sources[60], detectors[61], optically-driven memory[62], spin-photon interfaces[63], etc.

3.1.2 Fabrication of self-assembled quantum dots

3.1.2.1 InAs / GaAs

A wide range of III-V materials with different lattice constants provide many possible modes for epitaxial growth. The three possible epitaxial growth modes are: (a) Volmer-Weber mode (VW: island), (b) Frank-van der Merwe mode (FM: layer-by-layer), (c) Stranski-Krastanow mode (SK: layer plus island), respectively (see Fig. 3.1 (a-c)). SK mode is the most common method to grow QDs (VW mode is also possible to fabricate zero-dimensional materials, but will cause a large amount of defects, that ruins the optical performance.). During the epitaxial growth, the growth mode is determined by the competition between the adatom cohesive force and surface adhesive force, which depend not only on the lattice mismatch between the substrate and the deposited materials, but also on the thickness of the growing layers.

As is shown in Fig. 3.1 (d), GaAs and InAs have moderate lattice mismatch (7%), which leads to SK mode growth that forms QDs. The large difference of bandgaps between GaAs (1.42 eV at 300K, 1.52 near 4 K) and InAs (0.36 eV at 300K, 0.42 near

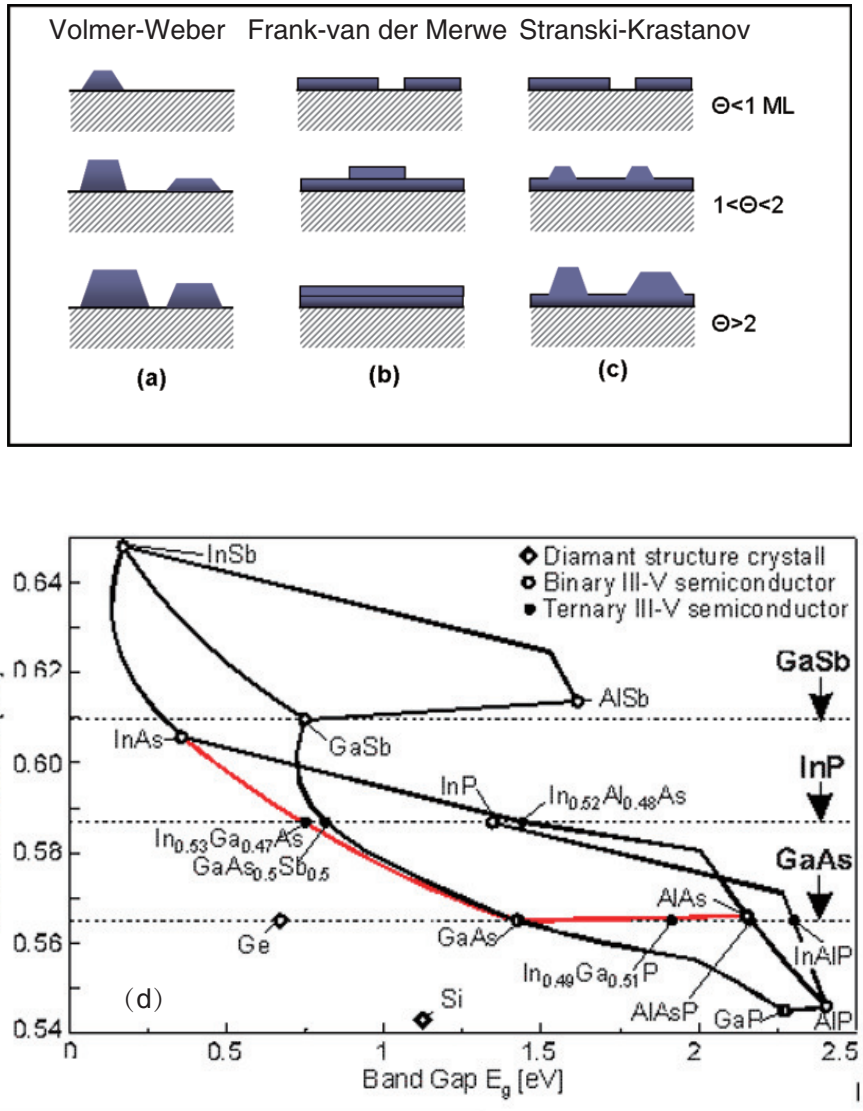

Figure 3.1: (a-c): The three growth modes during epitaxy.[11] (d) Plot of the lattice constant of various III-V materials as functions of their minimum bandgap, Eg[12].

4 K) provides a strong confinement that leads to the quantum effects inside of the InAs QDs. Based on the above-mentioned reasons, most of the work on self-assembled QDs has been concentrated in InAs / GaAs systems.

3.1.2.2 Molecular beam epitaxy growth of self-assembled quantum dots

This dissertation concentrates on self-assembled InAs/GaAs QDs fabricated using solid source molecular beam epitaxy (MBE). In MBE growth, elements heated in effusion cells sublimate and condense on the surface of a substrate wafer. The relative concentrations and flux rates can be precisely controlled to vary both material composition and layer thicknesses.

QDs can be grown on a doped GaAs substrate in order to allow for electrical control. A vertical electric field can be applied in between the Ohmic contact to the doped GaAs substrate and a Schottky contact to undoped top layers on the other side. The first step for the epitaxial growth of QDs is depositing a layer of undoped GaAs on the doped GaAs substrate. The second step is forming single InAs QDs by Stranski-Krastanov (SK) growth on the exposed GaAs surface. SK growth is also known as "layer-plus-island growth" and occurs when InAs is deposited on the GaAs surface. Because InAs has a larger lattice constant compared to that of GaAs, after a critical thickness of InAs (typically 1.6 monolayers [ML]) it becomes energetically favorable for additional InAs to aggregate into small clusters that minimize strain and surface energy. Those clusters, which are the QDs, will be covered by GaAs and AlGaAs to provide three-dimensional energy confinement. The layer grown before the aggregation of clusters is called the wetting layer and can be considered as a superlattice structure between that of GaAs and InAs QDs. The bandgap of this layer is in between GaAs and InAs. Our samples typically have an AlGaAs layer between the QDs and the top contact to reduce carrier tunneling from the Schottky contact. AlGaAs compounds have almost same lattice constant as GaAs and large bandgap that can prevent the escape of charges from the top surface of the sample. This AlGaAs layer is typically covered with a thin layer of GaAs to prevent oxidation of the Al.

The energy of the ground state PL emission in self-assembled InAs/GaAs QDs normally ranges from 1.0 to 1.2 eV at cryogenic temperature, which makes the PL measurements using Si-based detectors difficult. An In-flush technique is commonly applied to partially truncate the QDs in order to control their size and increase PL energy. The QDs will be partially capped by GaAs leaving the top part exposed. During a high-temperature annealing process, the In on the top of the QDs will be completely desorbed and removed.

3.2 Vertical Quantum Dot Molecules

3.2.1 Growth

To build up a system in which inter-dot coupling can be observed and controlled, we need to produce complexes in which two or more QDs are close to each other. These complexes are referred to as quantum dot molecules (QDMs). The growth of vertical QDMs, which was developed in 1995, is one of the most well-established methods to produce QDMs by MBE[13]. Vertical QDMs are fabricated by stacking two self-assembled QD layers along the growth direction. First, a single layer of InAs QDs are deposited on a GaAs (100) substrate and potentially truncated. GaAs is then deposited as a spacer of controlled thickness and the GaAs surface is recovered. Afterwards, the second layer of InAs QDs are grown on the top of the GaAs spacer layer. The preferential growth of the QDs in the top layer above QDs in the lower layer is due to the tensile stress caused by the buried QDs, which creates a preferential nucleation site with smaller lattice mismatch right above those buried QDs. The probability of alignment along the growth axis of the vertical QDMs decreases with the thickness of the spacer layer. Cross-sectional TEM pictures of the as-grown material confirms that the QDs on the top layer are well aligned with the bottom QDs. During the growth of vertical QDMs, In-flush can be used to control the size and shape of both layers of QDs. By utilizing this method, stacked QD arrays with more than two QDs along the growth direction can also be built up.[64]

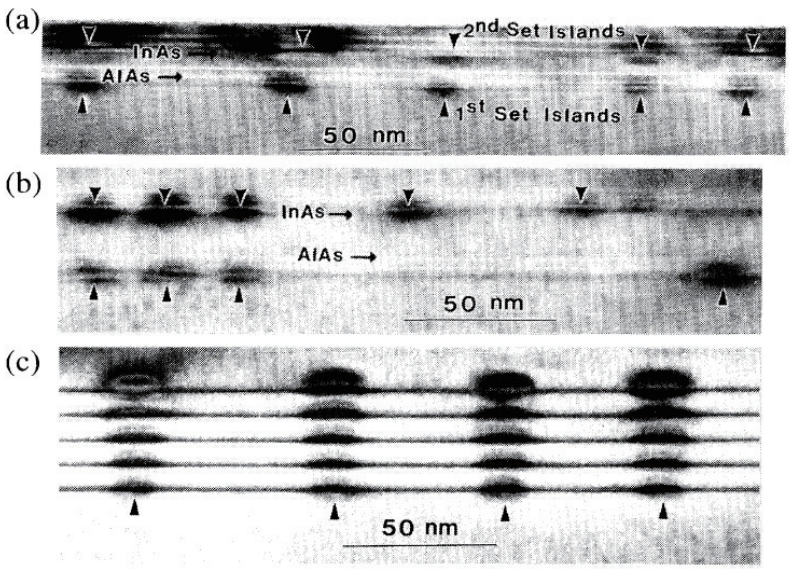

Figure 3.2: Cross-sectional TEM images for vertical QDMs with spacer layer thickness of (a) 46 and (b) 92 ML, respectively. (c) The vertical-stacked QD arrays with interdot spacing of 36 ML. [13]

A small lateral position misalignment for the two vertically stacked QDs is commonly observed in VQDMs. This causes the misalignment of the wavefunction of excitons and therefore breaks the angular symmetry. This symmetry breaking can have important consequences, including hole-spin mixing between light and heavy hole components.[65] This effect can be observed by experimental phenomena such as optical intensity of dark states and new anticrossing patterns between bright and dark states under magnetic field. The hole-spin-mixing phenomena also provides a way to control the spin orientations of holes.

3.2.2 Research progress

In recent years, research on VQDMs has made significant progress towards applications in quantum information processing. In 2001, Bayer et al. first observed the molecular state in self-assembled VQDMs by optical spectroscopy. The energy gap between two interacting PL emission lines from coupled QDs, which corresponds to

bonding and antiboding molecular states, decreases as a function of inter-dot spacing. This fact has been shown to arise due to the change of tunneling rate between two QDs as a function of interdot barrier thickness.[66] In order to switch the molecular state in VQDMs *in-situ*, an external electric field is applied to control the coupling of energy states in between two QDs. The first observed molecular states that show the electric field tuning were reported by Krenner in 2005.[49] The optical signatures of VQDMs under electric fields has been investigated by Stinaff et al. in 2006. This results shows the different anticrossing patterns in neutral exciton and positive/ negative trion emissions. Numerous subsequent publications have explored the anticrossing and x patterns in VQDMs to develop a comprehensive understanding of the spectral signatures in VQDMs and the underlying spin and charrge interactions that create these signatures. Here we briefly introduce this work as a starting point for analyzing self-assembled QDMs.

To clearly indicate the charge configurations, we use the notation $\begin{pmatrix} e_T & e_B \\ h_T & h_B \end{pmatrix}$, where e_T (e_B) indicates the number of electrons in the top (bottom) QD. Similarly for holes. For example $\begin{pmatrix} 0 & 1 \\ 1 & 1 \end{pmatrix}$ describes a QDM with one electron in the bottom QD and one hole in each QD. As is shown in Fig. 3.3(a), Coulomb shifts, Stark shifts and binding energies in the VQDM are similar to the case in single QD. However, the anticrossing pattern, as introduced in section 2.3, makes the spectral signatures of VQDMs much more complicated than the single QDs.

For the VQDMs sample studied in the example of Fig. 3.3, hole tunneling occurs when the energy states of two holes are in resonance. The right column of Fig. 3.3(b) shows the positive trion anticrossing pattern observed in VQDM samples with different thickness.[10] The hole tunneling between initial states $\begin{pmatrix} 1 & 0 \\ 1 & 1 \end{pmatrix}$ and $\begin{pmatrix} 1 & 0 \\ 2 & 0 \end{pmatrix}$ leads to the first anticrossing pattern with energy splitting denoted as δ_{x^+}. The hole tunneling occurring in the final states $\begin{pmatrix} 1 & 0 \\ 1 & 0 \end{pmatrix}$ and $\begin{pmatrix} 1 & 0 \\ 0 & 1 \end{pmatrix}$ is associated with the anticrossing

with energy splitting of δ_h. The diagonal PL lines across the initial state anticrossing comes from the triplet state with two holes in the same spin orientation. Because of the spin blockade, the interdot tunneling is forbidden in those states. It is also observed that the anticrossing energies (δ_{x^+} and δ_h) strongly depends on the interdot spacing, which determines the tunneling rate of holes. These results fits well with the calculated results shown in the left column of Fig. 3.3(b).

3.2.3 Potential applications

The follow-up work toward applications in quantum information processing (QIP) has been focused on the spin properties in the molecular states. The wave-function extent and coupling rates in the QDMs can be tuned *in situ* by electric field and this property can be utilized to build up electrically-controlled device. The g-factor of holes was observed to be tunable in GaAs/InGaAs VQDMs in 2006.[43] By replacing the GaAs interdot barrier to a GaAs/AlGaAs/GaAs sandwich structure, the g-factor of electrons in the molecular state can also be switched by 50% by tuning the electric field without charging the VQDMs.[67] Both of these results provide a path toward electrical control of coherent spin projections using g-tensor modulation.

Both the spin states of electrons[68, 33] and holes can be used as a basis for a qubit. Since the influence of nuclear spin is weaker for holes than electrons, hole spin has longer dephasing time and has recently emerged as a better candidate for a qubit. The unique properties of holes (such as hole-spin mixing observed in QDMs with misalignment along the stacking direction[65]) in VQDMs have attracted considerable attention, followed by a series of publications regarding the all-optical control of the the spin orientations in entangled states of holes[69, 36] in a VQDM.

One shortcoming of the idea for electrical control in VQDMs is that it only allows one-dimensional control. In recent years, research has been focusing on inducing strain *in situ* to the lattice of QDs to change the band structure. Such methods have been applied to VQDMs and successfully tuned the coherent tunneling rate in between the neighbor QDs.[70]

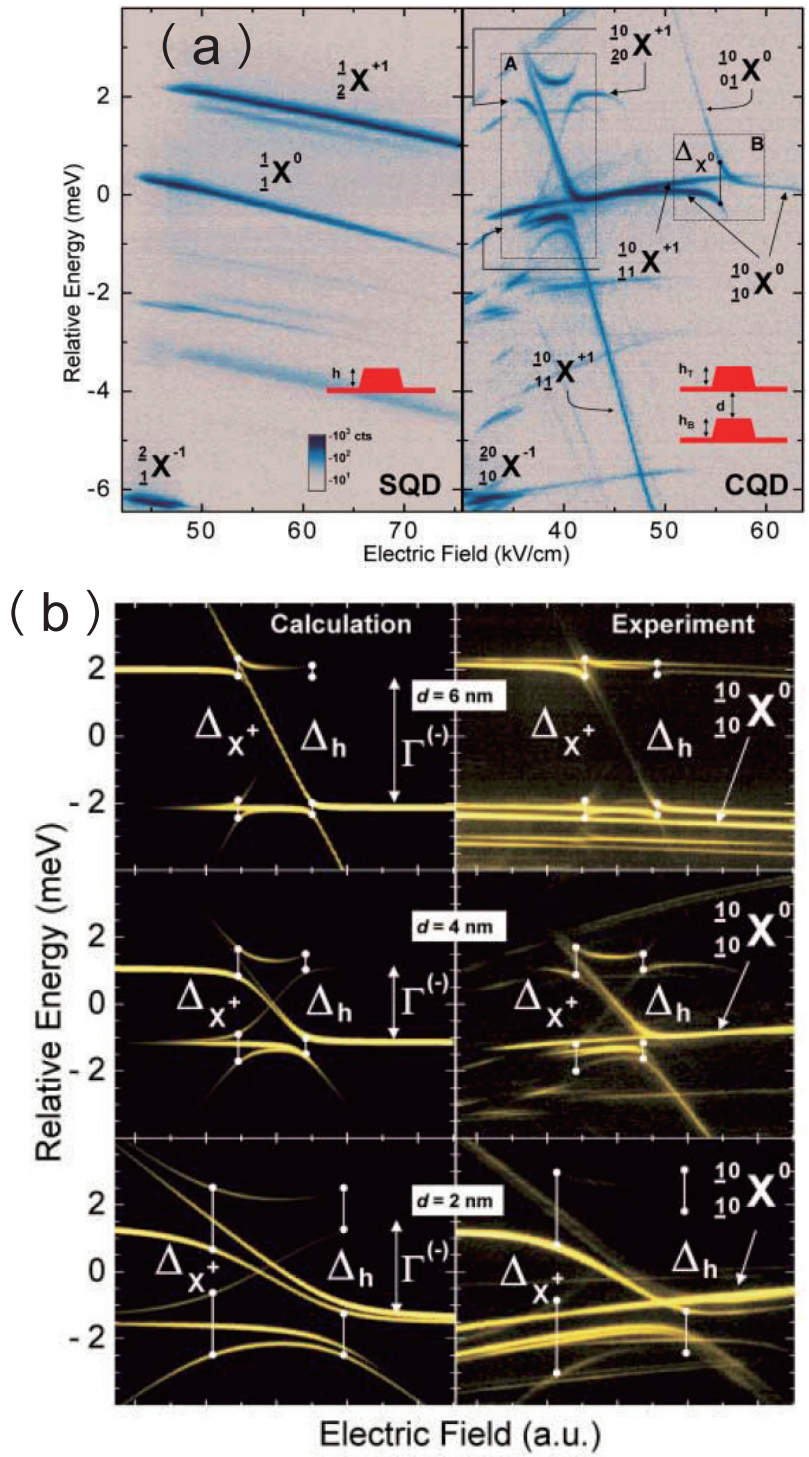

Figure 3.3: (a) (b)Theoretical and experimental results of PL energy anticrossing in positive charged single VQDMs. Results in different tunnel barrier thickness (2 nm, 4nm and 6 nm) are compared.[10]

3.2.4 Limitations

In VQDMs, an electric field applied along the growth direction varies both the quantum coupling and the charge occupancy of the QDs. The quantum coupling is varied as the confined energy levels of the two QDMs are tuned in and out of resonance with one another. The charge occupancy is controlled as the confined energy levels are varied relative to Fermi level set by the substrate doping. For information processing applications based on single charges or spins it is necessary to keep the charge occupancy of a QDM constant (e. g. only one electron). Controlling the quantum coupling independently provides an opportunity to modulate optoelectronic properties for bit initialization, manipulation and readout. I now show that the LQDM geometry provides an opportunity to independently control charge occupancy and quantum coupling.

3.3 Lateral Quantum Dot Molecules

3.3.1 Growth

The fabrication of LQDMs has advanced significantly in the last decade. Compared with the growth of VQDMs, growing LQDM pairs with structural homogeneity is more challenging. Although growth methods for producing LQDMs are straightforward in principle, rigorous control of the growth temperature, As flux and annealing time is required. Subtle deviations in these factors will lead to completely different quantum structures. The growth of InGaAs LQDMs is normally based on the pre-grown "template" nanostructure, which changes the distribution of surface strain or components locally on the substrate and causes the growth of QD complex surrounding this nucleation site.[54] These growth mechanisms provide a path to growth of QDMs in partially controlled locations. One method is to bury single InAs QDs followed by *in-situ* selective etching to produce the nanoholes. An *in-situ* etching based on excess gallium droplet is also a possible way to create nanoholes[71]. Ex-situ patterning on the GaAs substrate can be used to grow location-controlled LQDMs[72, 73].

The LQDMs discussed in this dissertation are grown by Salamo, Lee et al. in university of Arkansas.[54] The template in this case is a single dome-shape InAs QD grown in SK mode by MBE. The growth procedure is shown in Fig 3.4 (a). The template single QDs were relaxed at the monolayer coverage of 1.65 ML, followed by 30 s of annealing for good uniformity of QDs. Afterwards, the surface temperature was quenched to the capping temperature after the application of 10 ML of GaAs and 30 s of *in situ* growth annealing. Because InAs QDs have a larger lattice constant, the GaAs layer will not cover the top of single QDs.[74] During the annealing, the applied shallow GaAs layer will evolve dimer rows along [0 1 -1], which is called (2 X 4) surface reconstruction[75]. Guided by the (2 X 4) surface reconstruction, the In in the single QD will anisotropically diffuse along the direction of (0 1 -1) on GaAs surface and form elongated islands . The surface strain will further split the elongated quantum rod into two separated QD.

The geometry of InAs QDs grown from the template is related to the process of surface reconstruction on the [1 0 0] surface of the GaAs. This process is dependent on the monolayer coverage of the substrate/ adsorbate and the ambient conditions (i. e. gas pressure, temperature, etc.). The relatively low capping temperature will make the single QD diffuse while preserving the dome-shape of the original QD. As is shown in Fig. 3.5, 480 C is a temperature at which it is possible to generate double quantum dot molecules with the original dome-shape. When the capping temperature is higher than this temperature, the single QDs diffuse and form nanorods; When the capping temperature is lower than this temperature, the neighbor QDs merge as bridged/ dimpled QD pairs with substantial connection between them.

Similar LQDMs structure can also be achieved by pre-patterned GaAs droplet epitaxy. As flus was first applied on GaAs substrate sequentially to form the GaAs nanoscale mound templates in low temperature. By controlling the growth conditions, the morphology of the mound can be different.[54] InAs is deposited on substrates with mounts generated by droplet epitaxy, creating LQDMs consisting of multiple single QDs that surround the nanostructure caused by the surface strain distribution. During the

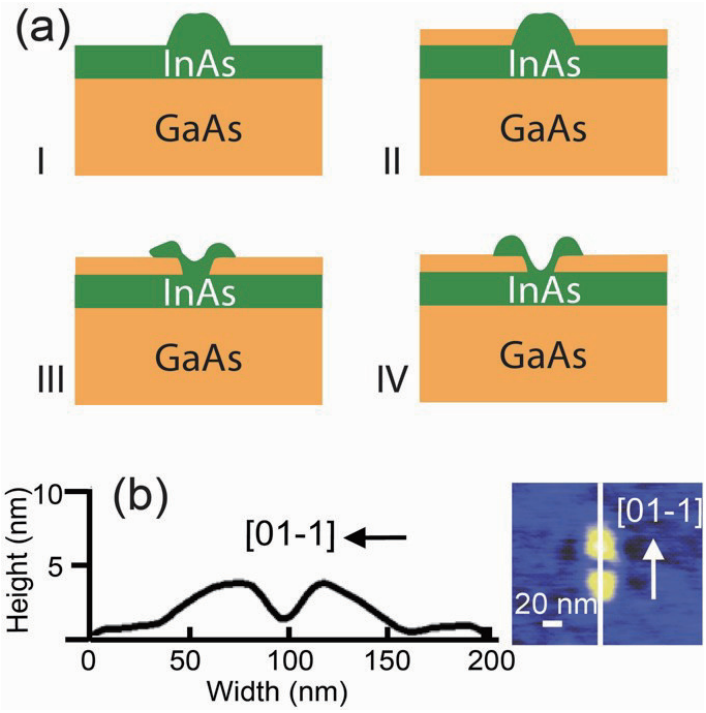

Figure 3.4: (a) Sketch of the different stages during the growth of partially-capping LQDMs. (b) (Left) The height profile of one typical LQDM grown by partially-capping mechanism. The height is measured along the axis of [0 1 -1] as is demonstrated on the AFM image of a single LQDM, as is shown on the right hand side of (b).

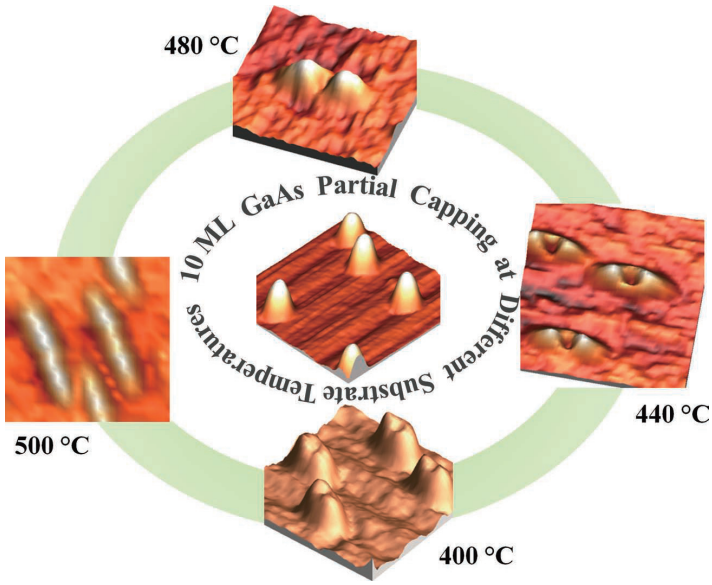

Figure 3.5: Evolution of nanostructure of partially-capped InAs QDs in different temperatures.[14]

deposition of InAs, the QD complex will firstly diffuse along the preferential direction to form LQDMs with two QDs. By continuing deposition of InAs, additional QDs will be generated along other lattice axes. The geometry of the final QD complexes depends strongly on the geometry of the initial GaAs mounds. These are promising method to grow LQDMs contain more than two QDs[76].

Very recently, Folsch et al developed the method to grow QDs with single-atom precision by using a scanning tunneling microscope (STM) tip to manipulate the atoms.[77] This is a very important step towards the development of QD complex-based devices. Considering the lateral arrangement, the energy structure and coupling behaviors of this type of QD complex should be similar to the self-assembled LQDMs.

The ideal LQDM sample for the study of optical properties and inter-dot coupling has the following characteristics:

1) The density of LQDMs should be small in order to allow single QD spectroscopy. For the templates based on self-assembled QDs, the LQDMs density is decided by the state-of-the-art of single QD growth. LQDMs with densities of 1 X 10^8

were achieved in 2012 using these methods.[71] The advantage of templates based on ex-situ etching is that the density and location can be predetermined. For our LQDMs sample, which is grown from partially-capping of single QDs, the ariel density is about 3 X $10^9/cm^2$. To investigate the properties of the LQDMs with such a large density, a mask with apertures of order 1 μm is needed.

2) The center-to-center distance between two neighbor dots must be as small as possible in order to have strong inter-dot coupling. Constrained by the pancake-shape of self-assembled QDs, it is impossible to require the inter-dot distance in LQDMs to be smaller than 30 nm, which is the typical diameter for single QDs. LQDMs grown by partially-capping, ex-situ patterning nanoholes and *in-situ* gallium droplet etching all result in LQDMs with center-to-center distance around 35 nm. However, the *in-situ* selective etching over capped InAs results in LQDMs with 57 nm inter-dot distance.

3) The ratio of double-dot structure on the whole sample should be large. Because of the inhomogeneous nature during MBE growth, complexes with more than two QDs and single QDs are expected to be found on some of the patterned sites. *in-situ* gallium droplet etching, in situ selective etching and ex-situ patterning result in double-dot ratio of 80, 61 and 40 percents respectively.

4) The vertical size of the LQDMs should be small to increase PL energy so that the Si-based CCD can measure its photoluminescence sensivitively. As is shown in Fig 3.4 (b), the peak height of our LQDMs is about 5 nm which is comparable with those LQDMs grown from nanohole templates. According to Ref. [73], the heights of the nanohole template LQDMs ranges from 5 nm to 10nm.

3.3.2 Research progress

Compared with the well-establish research on VQDMs, LQDMs are at a much earlier stage of development. The large center-to-center distance between the neighboring QDs (approximately 40 nm) makes the tunnel coupling much weaker than in the VQDMs[78]. Because the tunnel coupling is weak, the experimental evidence for

the existence of delocalized molecular-like states formed by coherent tunneling has only been indirect.

In 2006, the instructive experimental results focused on LQDM coupling were presented by Beirne et. al.[78]. By taking second order cross-correlation function measurements between the PL lines of an individual LQDM, they observed substantial antibunching of the neutral exciton recombination of the two neighboring QDs. This result verified the presence of quantum coupling in the LQDMs. Also, they found the dominant PL emission in a single LQDM can be switched by tuning the applied static voltage along the molecular axis.

It is expected that the anticrossing signature observed in VQDMs can be discovered in LQDMs. In 2007, a theoretical work towards coupling signature of LQDMs was published by Szafran et al.[15]. Using circular and square disks as the confinement potential, they predicted that the applied electric field that controls the coupling will visibly deform the wavefunctions within each of the dots and mix the single-dot energy levels. Following that, Wang et al. presented preliminary spectral evidence showing anticrossing signatures of single LQDMs under lateral electric field, which includes spectral lines strongly dependent on lateral electric field similar to the calculated results demonstrated by Szafran et al.[16].

The energies of the charge states in LQDMs is another focus of current research. Using atomistic empirical pseudopotential calculations, Peng et al.[18] have prepared a detailed model of the energetic states of a LQDM in which the two QDs are connected by a basin of residual InAs left from the initial seed QD. The compositional profile and growth techniques they model closely parallel the methods used to prepare our samples. The results predict three groups of electron energy levels with two groups delocalized over the entire LQDM for all values of the applied lateral electric field. The results also predict anticrossings as a function of applied lateral fields in both the negative trion (two electrons and one hole) spectra and positive trion (two holes and one electron) spectra.

Royo et al.[79] published their calculation results based on effective mass Hamiltonian of LQDMs, which indicates that the interdot distance will influence the emission energy of several charged states and this can be used to indicate the molecular coupling. Meanwhile, Munoz-Matutano et al[17]. reported the spectral results of charge control in LQDMs by an applied bias along the LQDMs axis. The external bias controls both the relative energies of the two QDs and the charge numbers in the LQDMs. Theoretical modeling based on the aforementioned study by Royo supports the experimental results and explains a measured energy shift of the negative trion as originating in the coherent electron tunneling. However, no anticrossing pattern is observed in the spectra, therefore the existence of the interdot tunneling can only be inferred.

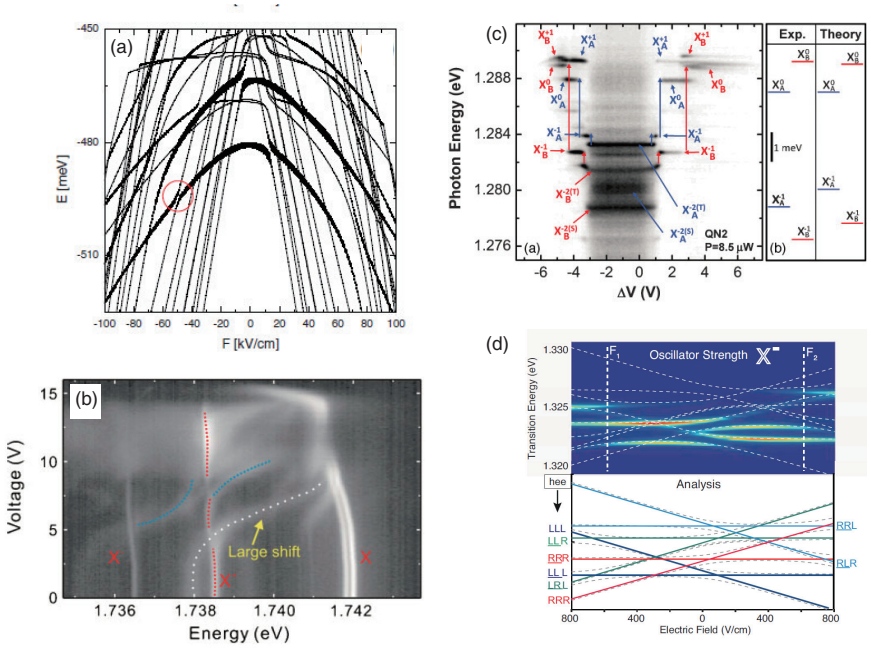

Figure 3.6: (a) Calculated exciton energy spectrum for LQDMs with circular confinement with interdot distance with 20 nm as a function of lateral electric field[15]. (b) PL spectrum of a LQDM as function of lateral field, the dotted lines which given guides to the eyes suggested anticrossing[16]. (c) PL spectrum as function of lateral bias that only shows the charge signature. The comparation between experimental and theoretical energies of different charge states are presented on its right hand side[17]. (d) Top: color map of the PL intensity from the negative trion state as a function of the PL energy (y axis) and the applied lateral electric field (x axis). Bottom: Analysis of the transitions based on atomistic empirical pseudopotential calculations[18].

Chapter 4

EXPERIMENTAL SETUP FOR LATERAL QUANTUM DOTS SPECTROSCOPY

4.1 Introduction

This chapter includes the following contents: (1) the optical path design of the μ-PL measurement of the LQDMs, (2) the fabrication of the optical device structure for LQDMs that applies electric field simply along the growth direction. This device was used to acquire the data reported in chapter 5 and 7 and (3) the cryostat systems for the optical measurements at low temperature with the application of electric/ magnetic fields.

4.2 Constraints of Lateral Quantum Dot Molecules Optical Experiments

Compared to the well-established single QDs and VQDMs systems, the development of understanding of optical properties of LQDMs have lagged behind for multiple reasons. One of the most important reason is that the self-assembly process of LQDMs is more complicated, which makes the optimization of shapes, sizes and densities of LQDMs more difficult.

First, it is difficult to control the shape of the LQDMs during MBE growth. A common method to manipulate the PL energy of single QDs and VQDMs is to truncate the top of the QDs using the indium flush technique during the MBE growth.[80] During this process, the top part of the dome-shaped QDs is removed and the QDs is truncated to a pancake shape with smaller spatial confinement and larger energy gaps. In VQDMs, the truncation process has two functions: first, it can adjust the PL energies of QDs to the sensitive range of Si-based charge-coupled camera (CCD); second, it can control the energy difference between the top and bottom dots in a single

VQDMs, which determines the applied field at which interdot coupling signatures can be obtained. Because this truncation process is hard to achieve during the growth of LQDMs, the significant inhomogeneity between LQDMs in a single sample makes the physical properties of different LQDMs vary. The LQDMs we study have a relative small PL energy (about 1200 meV for neutral exciton emission), which decreases the signal intensities detected by the CCD. This increases the difficulty of the micro-PL and time-resolved PL (TRPL) measurements on our single LQDMs.

Another problem with the LQDM sample we are working on is the high ariel density of LQDMs on the surface. The ariel density of our sample is about $30/\mu m^2$. To measure the PL of single LQDMs, it is necessary to isolate single LQDMs from the ensemble. It is impossible to constrain the size of the laser beam to be smaller than 1 μm. Therefore, we need an opaque mask to cover most of the sample surface and isolate single LQDMs. A high-NA lens to focus the laser down to 1 μm is required during the PL measurement.

4.3 Optic Path for Photoluminescence Measurements

Fig. 4.1 shows the schematic of the path for the micro-PL measurement. For PL spectroscopy the output of a Coherent Mira Ti: Sapphire laser, pumped by a 532 nm Verdi V5 laser, is used to excite the LQDMs at 870 nm. The laser first goes through a BEOC laser power controller (not shown in the figure) to stabilize the intensity. The patterned LQDM sample was mounted on the cold finger of an Advanced Research System DMX-20 closed-cycle cryostat cooled to 12 K to suppress the phonon excitation of carriers out of the LQDMs. Emitted PL was collected by a Mitutoyo high numerical aperture objective and long-pass filtered to remove residual laser light. The signal was analyzed with a 0.75 m Acton SpectraPro 2750 spectrometer equipped with a liquid nitrogen cooled CCD camera with 21 μeV spectral resolution. The data acquisition was controlled by a LabView program that continuously acquires PL spectra as a function of applied voltage and/or laser power. During the PL measurement, electric

and magnetic field applied on the LQDMs can be varied *in situ* to manipulate the total charge occupancy, inter-dot coupling and wavefunction extent of the LQDMs.

The Mira Ti: Sapphire laser has the capability to produce output over a wavelength range from 700 to 950 nm. A mode-locked oscillator generates ultrashort pulses with femtoseconds to picoseconds with pulse widths at a repetition rate of 80 MHz. By using a part of the pulsed laser to simulate a trigger diode and collecting the PL with an avalanche photo diode (APD), we are able to measure the time-resolved PL (TRPL) and understand the dynamic processes during the emission of the PL. Some preliminary TRPL experiments has been done on the ensemble LQDMs.

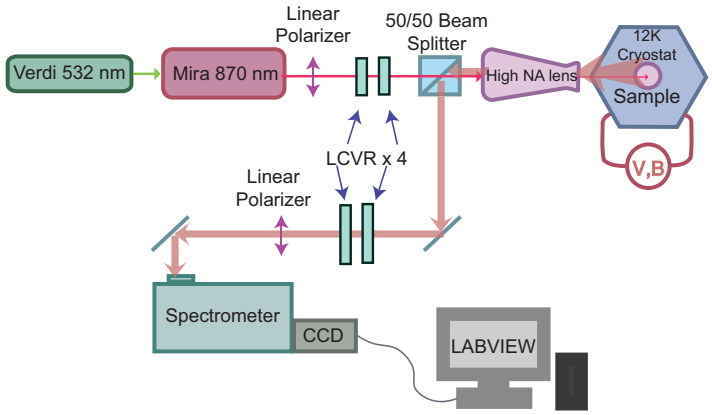

Figure 4.1: Optical path for micro-PL measurements of LQDMs.

By adding components to control the polarization of the laser and analyze the polarization of the PL, this system can be used to extract information on the spin projections of carriers in the LQDMs. On the incoming and outcoming paths, two Meadowlark liquid crystal variable retarders (LCVRs) can be used to control both the phase delay and polarization orientation of incoming laser and PL.

A LCVR takes advantage of the orientation-dependent birefringe in liquid crystal (LC) molecules. The LC molecules are oriented in a default alignment when the applied voltage is zero. The applied voltage will continuously change the orientation of the LC molecules and therefore the phase delay between the fast and slow axes of

the LCVR. By tuning the voltage from 0 to 10 V, the retardance of a LCVR can be tuned from 1400 nm to 100 nm.

4.4 LQDMs in a Schottky Diode

4.4.1 Introduction

In order to control the charge occupation of LQDMs, the LQDMs are embedded in a Schottky diode with 2-electrodes on both the top and bottom surface to apply strict vertical electric fields (along the growth direction). Fig. 4.2(a) shows a schematic diagram for the layout of the LQDMs sample within a Schottky diode. The sample composition and layer thicknesses are labeled. By applying an electric field in the growth direction, which tilts the band structure, the electrons in the Fermi level of the n-doped layer can be sequentially injected into the LQDMs in order to charge the LQDMs with additional electrons. Here we give an introduction to the layer-by-layer structure of the LQDMs diode followed by the fabrication of electrodes.

4.4.2 LQDMs sample layout

80 nm of undoped GaAs is deposited on top of the doped substrate. Electrons in the doped layer need to tunnel through this barrier in order to inject into the LQDMs. Normally this tunnel barrier is designed with a few tens of nanometer thickness. A thicker barrier will reduce the tunneling rate drastically and a thinner barrier can not effectively isolate the QDs from the doped layer. The wetting layer and LQDMs are grown on top of the tunnel barrier.

The InAs are covered by a sandwich structure that includes 230 nm of intrinsic GaAs, 50 nm of $Al_{0.3}Ga_{0.7}As$ and 10 nm of GaAs. The 230 nm of GaAs is deposited first to create a defect-free interface for good optical properties of QDs. A thin layer of GaAs is deposited on the top surface of the device to prevent the oxidation of AlGaAs layer.

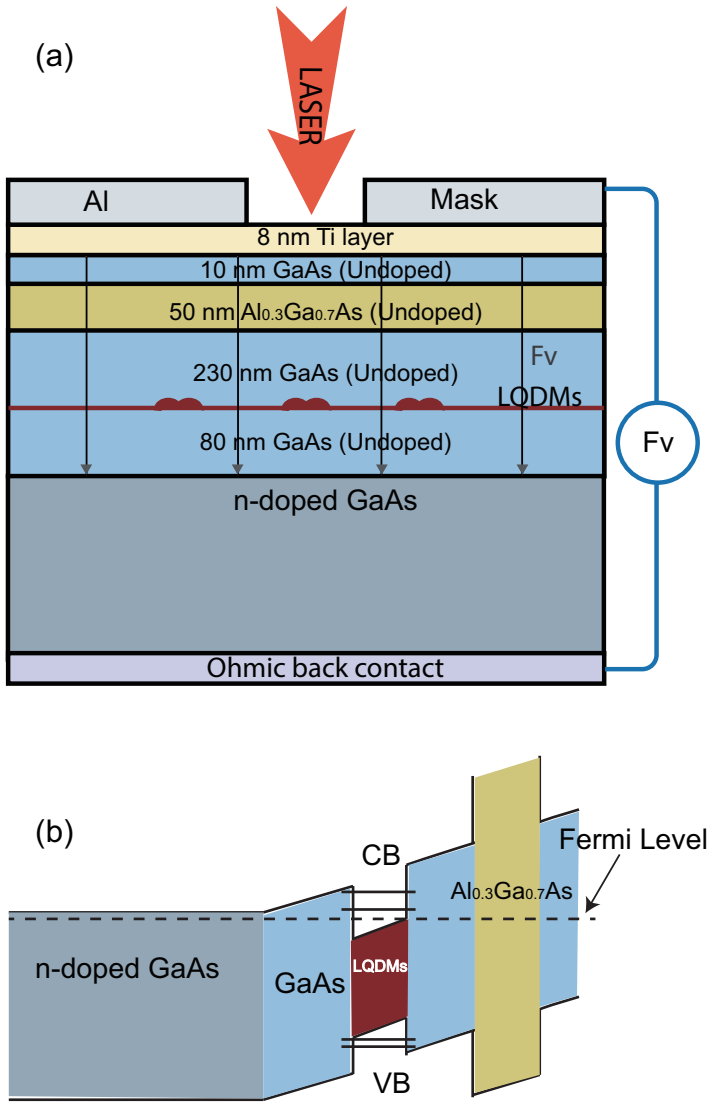

Figure 4.2: (a) The layout of our self-assembled LQDMs sample grown on a n-doped GaAs substrate within a 2-electrode Schottky diode. (b) Band diagram of the LQDM device in the growth direction without electric field applied.

4.4.3 Fabrication of electrodes

4.4.3.1 2-electrode device

The 2-electrode device introduced in this section has been used to generate the result presented in Chapter 5 and 7. The device was processed with an Ohmic back contact on the bottom of the n-doped GaAs substrate. (See Appendix A.2 for experimental details.) In order to acquire spectra from single LQDMs and strictly control the bias along the growth direction of the LQDMs, an Al Schottky contact with 1 μm apertures is applied on the top surface of the sample by electron-beam (e-beam) evaporation. A semi-transparent thin Ti layer (8 nm) is also deposited between of the sample and Al layer to force the electric field to be strictly along the growth direction. We refer to this as a vertical electric field. The Al mask is patterned by optical lithography using a Karl Suss MJB-3 Mask Aligner. The recipe for lithography can be found in Appendix A. By tuning the vertical electric field applied to the LQDM sample, electrons from the n-doped GaAs layer will be injected into the LQDMs and be confined in LQDMs. During the optical measurements, the laser illuminates LQDMs through the apertures on the Al mask and only the single LQDMs under the selected aperture are probed optically.[81]

To fully investigate the energy properties of LQDMs, it is necessary to leave large apertures for the optical measurement of ensembles of LQDMs. The 8 nm Ti thin film applied by e-beam evaporation is not a promising electrode for applying strict electric field when the aperture size becomes too large. Therefore, the sizes of apertures on the Al mask should be no larger than 20 μm.

4.4.3.2 3-electrode device

The scheme of the Schottky LQDM diode being investigated in chapter 6 is shown in Fig. 4.3. 5 μm gaps perpendicular to the 1 μm gaps provide access for ensemble photoluminescence (PL) measurements. The interdigitated contacts provide the opportunity to apply both lateral (perpendicular to the growth direction) and vertical (parallel to the growth axis) electric fields in order to independently control

the charge occupancy of the molecule and the quantum coupling between the two QDs that comprise the molecule. In chapter 6 we focused on charging of the QDMs and always apply the same voltage to both of the top contacts. Although the two interdigitated top contacts always have the same electrical potential, the long term goal of applying both lateral and vertical electric fields precluded the inclusion of a semitransparent Ti layer to maintain uniform electric fields across the 1 μm gap. The interdigitated contacts are separated by 1 μm, but only 370 nm separates the top contacts from the n-doped GaAs that provides the back contact. Consequently, the net electric field at the LQDM location contains both vertical and lateral components. The ratio of lateral and vertical field components depends on the spatial location of the LQDM within the lateral gap, which cannot be measured and varies from LQDM to LQDM. We therefore quote only the value of the applied voltage and not the net electric field for experiments performed with this sample.

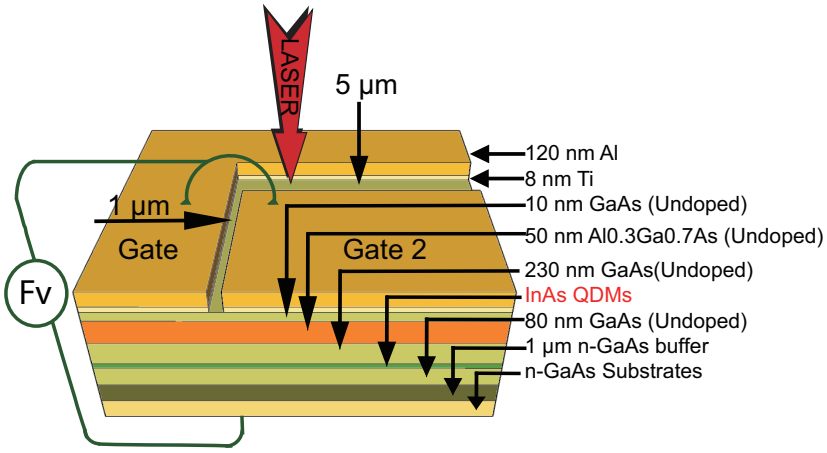

Figure 4.3: The 3-dimensional layout of our self-assembled LQDMs sample grown on a n-doped GaAs substrate and fabricated into a 3-electrode Schottky diode.

4.5 Closed-cycle Cryostat Systems

To suppress the influence of phonons on the optical properties of LQDMs, the LQDM samples are held in an Advanced Research Systems closed-cycle cryogenic refrigerator (DE204SF-DMX20-OM) for low-temperature measurements. The minimum temperature this system can achieve at the sample interface is 8 K. This refrigerator works based on the Gifford-McMahon cycle, which includes a compressor, an expander and two gas lines to transfer gas at high pressure and low pressure through the system. Using Helium as a working fluid, the system removes the heat in the sample holder by going through a full cryogenic cycle at the frequency of the rotary valve that alternately opens and closes as the displacer reciprocates between two spaces that store gas. The cryogenic cycle includes 4 steps:

1. High-pressure gas is admitted into the cold head. Some of the heat from this gas is absorbed by the regenerator material inside the cold-head, lowering the gas temperature.

2. The valve is turned to the low-pressure line and the high-pressure gas goes through an isothermal thermal expansion, taking up heat.

3. The displacer moves and forces the low-pressure cold gas to go through the regenerator material, taking up heat from the regenerator.

4. The valve is tuned back to the high-pressure end and the hot air is compressed and expelled. The whole system comes back to the first phase.

The refrigeration system we are using includes two cryogenic cycles. The gas cooled by the 1st stage will be injected to the 2nd stage displacer and goes through the second cooling cycle. The compressor provides the helium gas with appropriate pressure. It will generate heat during the operation. The electric power and heat exhaust of the compressor is connected in series with a coolpac for thermal dissipation. The compressor can only work when the coolpac is turned on. Plastic tubing transfers cooling water between the compressor and the coolpac to take up heat from the compressor.

To perform micro-PL by using this system, one of the most important factors

is isolating the vibration from the cryocooler in the sample holder. The sample should be stable in the same location with sub-micron movements for the whole experimental cycle, which is usually up to 10 hours. An isolation bellows is used to isolate the expander, which is fixed on the ceiling of the lab, the sample interface, which is mounted on the optical table. To maintain the best performance of the system, it is very important to maintain the relative position of the expander and the sample interface. Helium gas with pressure of 0.6 psig is flowing into the bellows for heat exchange.

4.6 Helium-cooled Magneto-optical Cryostat System

In order to conduct optical measurements under magnetic field, the LQDMs sample was mounted in our superconducting magnet system manufactured by Janis research company. Fig. 4.4(a) shows a schematic of the system. In this system, the alloyed metal coil is soaked in liquid Helium in order to run below the characteristic critical temperature of superconductivity. Two groups of superconductor coils in the system can apply magnetic field up to ± 9 Tesla in the vertical direction and ± 4 Tesla in the horizontal direction, respectively. To achieve a good heat isolation and reduce the Helium cost, the liquid Helium reservoir is surrounded by a liquid Nitrogen reservoir and an outer vacuum jacket. The LQDM sample is held in the bottom of the center column for optical measurements. An inner vacuum jacket is in between the center column and liquid Helium reservoirs to isolate the thermal gradient in the column from the Helium bath. Continuous liquid Helium flow from the reservoir to the bottom of the center column through a capillary to maintain the temperature of the sample below 10 K. The vaporized Helium atmosphere around the sample also protects the system from water in the air and provides a transparent medium for optical imaging.

The laser goes through the optical ports on the platform at the top of the magnet system, reflected by the mirrors, and illuminates the sample at the bottom of the center column. Fig. 4.4(a) shows the components of the insert structure inside the center column. To control the position of the sample *in situ*, the LQDMs sample is held by three Attocube piezoelectric nanopositioners oriented in two horizontal and

one vertical directions. One high numerical aperture lens is positioned right above the sample to focus the laser beam to micrometer range and collect the PL. To manage the

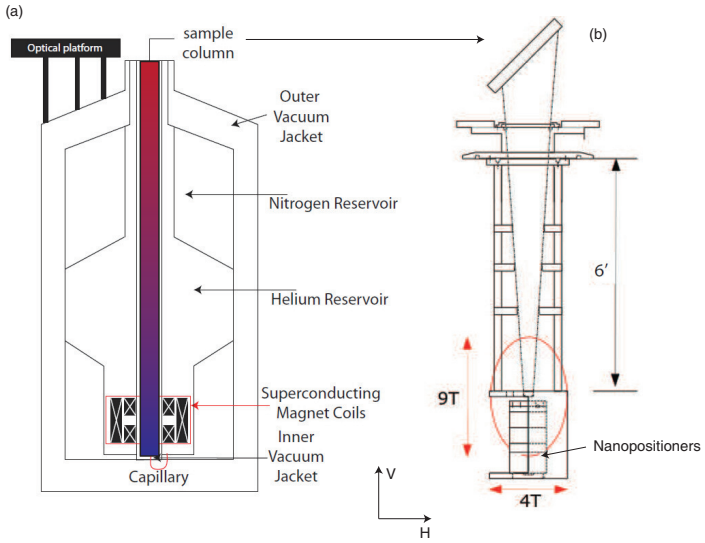

Figure 4.4: (a) Diagram of the Janis superconducting magnet system. The color in the center column schematically shows the gradient of the temperature. (b) Diagram of the microscopic insert of the center column in the magnet system.[19]

rising market price of Helium, a cold finger Helium reliquefier was recently installed in the cryostat system. The liquid Helium boil off condenses on the cold finger and drips back into the cryostat. Ideally, the rate for the reliquification of Helium is equal to the boil-off rate and a small flow of Helium gas into the cryostat should be sufficient to maintain the system at equilibrium.

Chapter 5

ENERGY SHELL STRUCTURE OF LATERAL QUANTUM DOT MOLECULES: GROUND STATE

5.1 Introduction

In order to understand the energy shell structure of LQDMs, we need to start with the ground state (GS). In this chapter, we present a systematic analysis of the photoluminescence (PL) emission of self-assembled InAs LQDMs under a voltage strictly applied along the growth direction, as is introduced in section 4.4.3. We observe a series of discrete PL lines with distinct energy shifts with the increasing electric field. We assign these discrete lines to specific charge configurations using a combination of theoretical modeling and analysis of the formation dynamics. We compare the spectral signatures of LQDMs in which the two QDs have similar and different confined energy states. The measured spectral shifts support the conclusion that inter-dot electron tunneling is present in trion states.

5.2 Power-dependence of Ensemble Photoluminescence

In Fig. 5.1 we plot the ensemble PL signal measured in the 5 μm gaps of the interdigitated top Al contacts and a few examples of single LQDM PL measured in the 1 μm gaps. Three gaussian PL peaks are visible, centered at 1202, 1242, and 1279 meV with full width half maximum (FWHM) values of around 40 meV. These peaks could be attributed to different energy shells of the LQDMs (analogous to the s, p, and d shells in single InAs QDs) or to a distribution of QD types (e.g. a fraction of the seed QD population that did not evolve into LQDMs). To distinguish these possible explanations, we measure the PL intensity of the three ensemble peaks as a function of laser power. The results are presented in Fig. 5.2. The inset of Fig. 5.2

shows that the lowest energy peak (1202 meV) dominates emission at the lowest laser power. For laser powers between 0.1 and 2 mW (power density of 7 to 140 W/ cm^2, see appendix B.1 for more details), the intensity of the lowest energy peak increases with laser power and there is no measurable intensity for other peaks. The intensity of the next highest peak (1242 meV) becomes measurable at laser powers of 2 mW. At laser powers greater than 2 mW, the intensity of the peak centered at 1242 meV increases much more rapidly with laser power than the peak centered on 1202 meV. Emission from the highest energy peak (1279 meV) is not measurable until the laser power reaches about 10 mW. Between 10 and 200 mW, the intensities of the second and third peaks increase with a similar dependence on laser power.

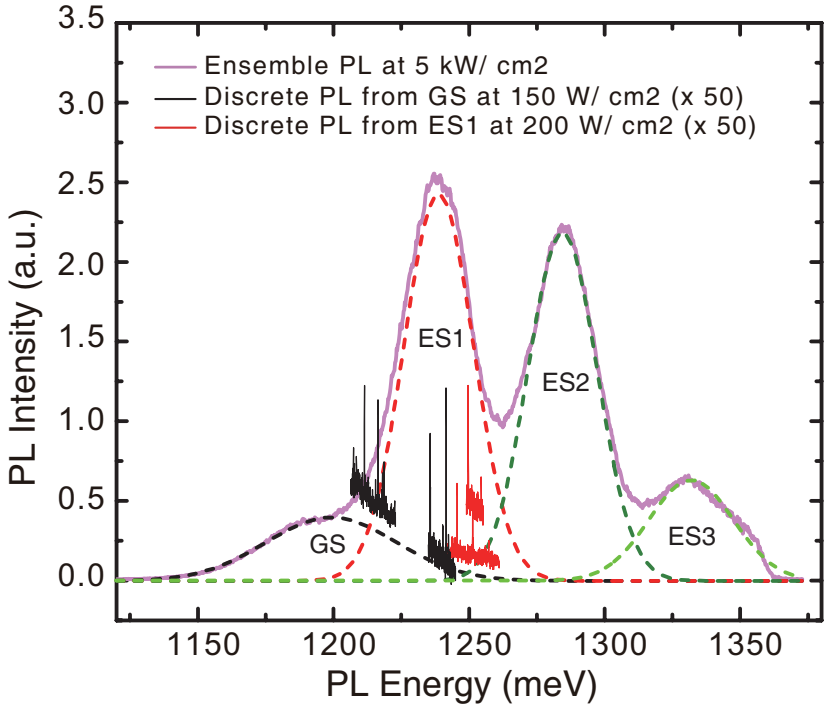

Figure 5.1: PL from LQDM ensemble (blue), single LQDM GSs (black) and single LQDM ES1s (red) measured in flat band conditions with zero magnetic field. The ensemble PL is fit by four Gaussian curves (dashed lines) to identify four PL energy shells.

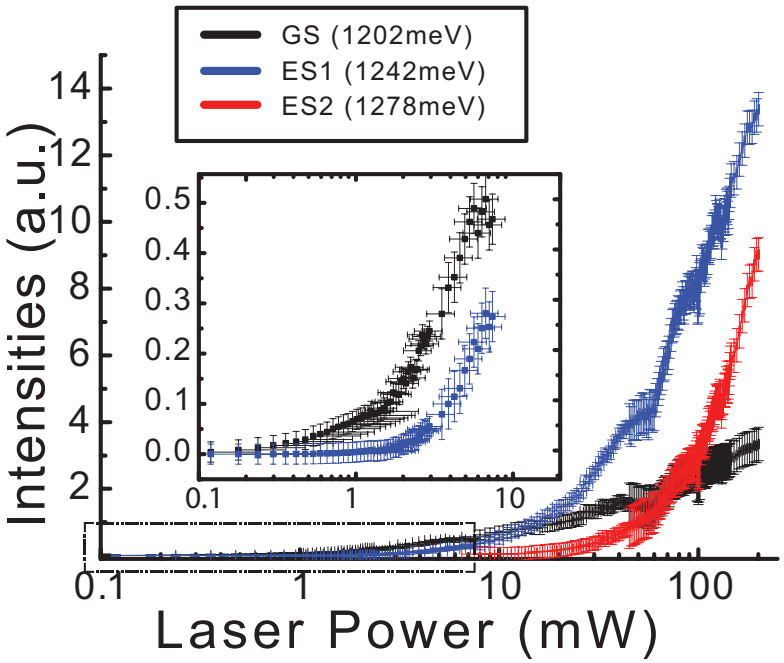

Figure 5.2: Dependence of PL peak intensity on laser power between 0.1 to 200mW. The inset is the enlarged graph of the area framed with the dashed line rectangle.

If the observed PL peaks originated in a distribution of QD types, optical emission from all peaks would be expected at the lowest laser powers. The observation that the lowest energy peak dominates at low powers, and that peaks with increasing energy gain optical intensity only at increasing laser powers, indicates that these three peaks are part of a single structure in which carriers can relax to lower energy shells. Emission from excited states becomes possible only as the increasing laser power generates sufficient carriers to populate the lower energy states and inhibit relaxation.

We therefore assign the three observed peaks to different energy shells of single LQDMs. In Fig. 5.3 we schematically depict the LQDM energy shells. The energy levels of the two QDs that comprise the LQDM are typically slightly different; Fig. 5.3 depicts a situation in which the left QD has lower energy levels. We stress that the measured ensemble PL presented in Fig. 5.1 and 5.2 provides evidence that the three observed PL peaks come from distinct energy shells of a single quantum structure. These data,

however, are not sufficient to identify the specific energy shells associated with each transition or the degree of delocalization of states in any shell. As described below, we use additional measurements of single and ensemble LQDMs to systematically justify the model presented in Fig. 5.3.

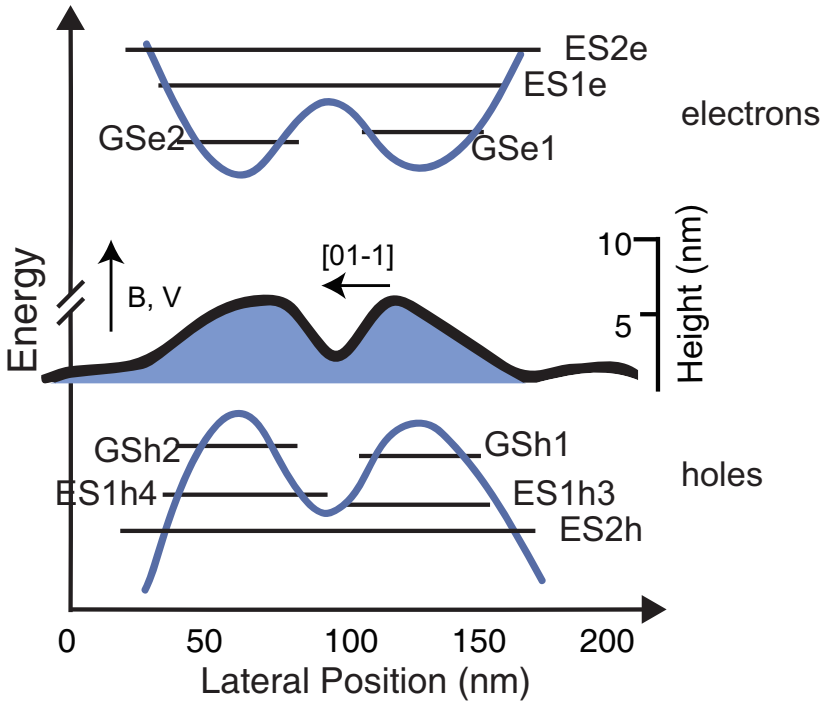

Figure 5.3: Schematic band diagram of a single LQDM. The middle inset shows the cross-sectional profile of a single LQDM with arrows denoting the molecular axis and the direction of applied electric and magnetic fields.

We first show that the power dependence and saturation behavior presented in Fig. 5.2 is consistent with assigning the three PL peaks to the GS_e-GS_h, $ES1_e$-$ES1_h$ and $ES2_e$-$ES2_h$ energy shells of LQDMs. At very low exciting laser powers, on average less than one electron and hole are absorbed into the LQDM. These carriers thermally relax through the ladder of energy states in the LQDM. Thermal relaxation in confined structures typically takes place on ps time scales, so emission from excited energy levels is unlikely.[82] Consequently, we assign the lowest energy observed PL peak (1202 meV) to recombination of electrons and holes in their lowest energy states

(E_0 and H_0). The second measured PL peak (1242 meV) could be assigned to optical recombination from GS_e to $ES1_h$, $ES1_e$ to GS_h, or $ES1_e$ to $ES1_h$. In single QDs, the asymmetry of envelope functions from different shells (e.g. s and p) suppress optical recombination and observed PL is dominated by s to s and p to p transitions. This argument suggests assigning the peak to recombination from $ES1_e$ to $ES1_h$. The dipole selection rules are known to be relaxed by strain, piezoelectric effects, and applied electric fields.[83]. The complex potential profiles of the LQDMs studied here make it likely that the wavefunction symmetries and dipole selection rules are more complicated than those of conventional single QD confined states. Consequently, we cannot rule out recombination from GS_e to $ES1_h$ or from $ES1_e$ to GS_h. The intensity of the $ES1_e$-$ES1_h$ peak rises as a function of laser power because increased laser intensity increases the probability that the E_0 states will be populated by optically injected carriers. PL emission originating in the $ES1_e$ energy shell becomes significant only when the GS_e states are already filled and intraband relaxation from $ES1_e$ to GS_e is suppressed. By the same argument we assign the third PL peak, centered at 1279 meV, to PL originating in the ES2 energy shell.

The measured difference between ensemble PL peak energies GS_e-GS_h and $ES1_e$-$ES1_h$ is 40 meV. This value is in reasonable agreement with the separation between GS_e-GS_h and $ES1_e$-$ES1_h$ transitions predicted by pseudopotential calculations of LQDMs (approximately 28 meV).[84] Similarly, the measured difference between GS_e-GS_h and $ES2_e$-$ES2_h$ ensemble PL peak energies (77 meV) is in reasonable agreement with the predicted difference between GS_e-GS_h and $ES2_e$-$ES2_h$ transitions (approximately 57 meV).[84] The reasonable agreement with calculated values supports, but does not unambiguously confirm, our assignment of PL peaks. Our measured values of the energy separation between transitions are consistently larger than the those predicted by Peng et al. This difference may be due to differences between the the LQDM morphology used in the computational model and the LQDMs studied experimentally.

5.3 Photoluminescence of Neutral Excitons and Positive Trions in LQDMs

5.3.1 Bias map with X^0/ X^+ doublets

Having established a basic assignment of PL peaks to the energy shell structure of LQDMs, we now focus on the Coulomb interactions in the localized GS of a single LQDM in order to understand the effects of charge occupancy. By collecting the PL from 1 μm apertures on the diode sample, we are able to observe PL peaks with linewidth on the order of 100 μeV, which we concluded is emitted from single LQDMs.

The color map in Fig. 5.4(a) presents the discrete PL signature of a single LQDM (LQDM 1), as a function of applied vertical electric field. The x axis is the electric bias applied along the growth direction of the LQDMs while the y axis indicates the PL energy of the discrete PL lines. The color shows the intensities of PL emission, as represented in the inset of Fig. 5.4(a). The energy range of this set of PL lines indicate that the PL emission is from the ground states of the LQDM. Typically, the two QDs, that comprise the LQDM will have slightly different energy levels. Although we cannot assign PL emission to the right or left QD, we simplify the discussion by always assigning the low-energy PL emission to the right QD and the high-energy PL to the left QD.

At negative bias, three PL lines (X^0_R, X^+ and X^+') are observed (at 1223.7, 1223.9 and 1224.2 meV, respectively). A fourth PL line X^0_L is also observed at 1225.7 meV with relatively weak intensity. With increasing applied voltage, these four lines show identical Stark energy shifts and distinct changes in PL intensities (See Fig. 5.4(c)). As the applied voltage reaches 0.58 V (0.66 V), line X^0_R (line X^+/X^+') is turned off. Parallel PL lines with approximately 0.5 meV separation, such as line X^+/X^+' and X^0_R, are a characteristic signature in the PL of single LQDMs. Fig. 5.4(b) presents a survey of the parallel PL lines in six LQDMs in our sample. In all of these examples, the energy separation between the two dominant PL lines are between 0.4 and 0.5 meV. This pair of PL lines with small and constant energy separation could originate from either 1) recombination involving the energy levels of two different QDs

or 2) recombination of one single QD with the presence of different numbers of spectator charge in the LQDM. As indicated by the state labels, we assign the pair of lines to the X^0 and X^+ charge configurations of a single QD within the LQDM. We now justify this assignment.

5.3.2 Analysis

In the n-type Schottky diode, the electron energy states of QDs are higher than the doped Fermi level under negative bias. Consequently, electrons participating in the PL emission must be optically generated. Under moderate excitation laser intensity, the number of electrons occupied a single LQDM during the PL emission should be no more than one. Therefore, PL lines that show up at negative bias are assigned to either neutral exciton (X^0) or positive trion (X^+) states. Due to the anisotropic self-assembly growth mechanism of the LQDMs sample, it is unlikely that the energy difference between two neighboring QDs would consistently be 0.4 to 0.5 meV. This suggests that the two consistently observed pair of PL lines separated by 0.5 meV should not be assigned to two separate QDs.

To support the assignment that the high energy PL is from neutral exciton emission and the low energy PL line is from positive trion emission, we look at the electric field and laser power dependence of the intensities of these lines. The peak intensities from PL emission of line X^+, X^+', X_R^0 and X_L^0 are plotted as a function of vertical voltage in Fig. 5.4(c). The intensities of line X^+ and X^+' show the same nearly-linear dependence on the voltage and reach their maximum at 0.25V before dropping to zero. Line X_R^0 and X_L^0 both have low intensity until a certain voltage and then gain intensity abruptly. The intensity of PL emission from X^0 and X^+ depends on the efficiency of two processes. First, the X^+ configuration is more likely to form at low bias, when it is relatively easy for an optically generated electron to tunnel out of the LQDM, leaving behind an excess optically-generated hole, thereby increasing the probability that the X^+ will form. Second, larger electric fields drive e-h pairs to separate and therefore weaken the PL emission of both X0 and X+. As shown in

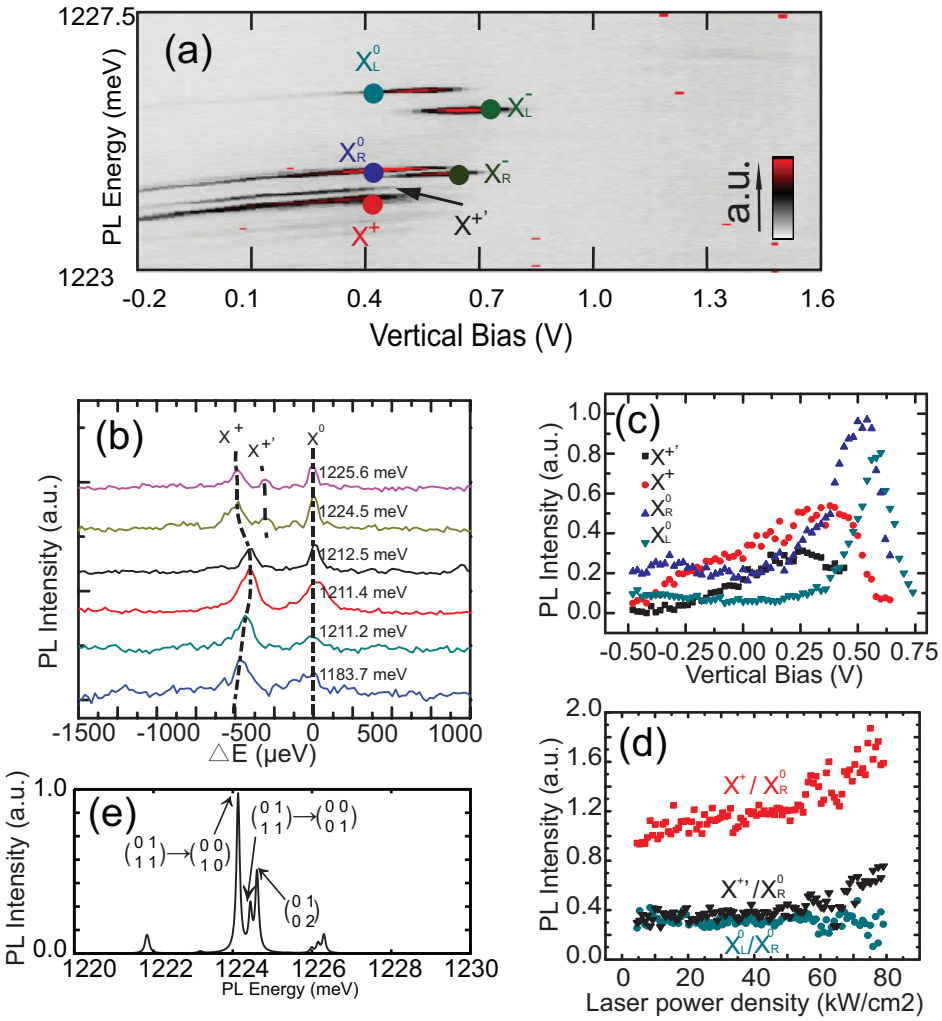

Figure 5.4: (a) PL spectrum of the ground states transitions in LQDM 1 as a function of vertical voltage. (b) PL spectra of X^0 and $X^+/X^{+\prime}$ in 6 different LQDMs. Lines are guides to the eye. Energies are plotted relative to the emission of the X^0 state, with the absolute energy of the X^0 state indicated by the inset text. (c) Intensities of PL lines X^0_R, $X^+/X^{+\prime}$ and X^0_L as a function of vertical voltage. (d) Intensity ratios of PL lines as a function of laser power densities under 0.41 V vertical voltage. (e) Theoretical modeling results of the energies and intensities of positive trion emissions in LQDMs based on the energies of neutral exciton emissions.

Fig. 5.4(c), line X_R^0 and X_L^0 sharply increase in intensity as line X^+ and X^+' begin to get weaker, near 0.25 V. This is the turning point at which it is no longer favorable for the electron to tunnel out of the QD and the emission of X^0 is therefore enhanced. This analysis supports the assignments of the PL lines in Fig. 5.4(a).

Integrated PL intensities of the lines in Fig. 5.4(a) as a function of laser power density further support this assignment, as shown in Fig. 5.4(d). The ratio of PL intensities of line X_R^0 and X_L^0 remain constant with increasing laser power. In contrast, line X^+ shows increasing intensity relative to line X_R^0 with increasing laser power. Compared with holes, electrons have a smaller effective mass and are able to tunnel out of QDs more rapidly. The formation of the X^+ necessarily requires two photons. One photon generates an electron hole pair from which the electron tunnels out, leaving a hole behind. The second photon generates an additional electron hole pair, allowing recombination of an electron hole pair in the presence of the additional hole. Consequently, formation of the X^+ state requires more photons than formation of X^0 state. The superlinear laser power dependence of intensities of lines X^+/X^+', relative to X^0, indicates that these PL line should be assigned to the positive trion states. This laser power dependence allows us to assign line X_R^0 to emission involving neutral excitons. The end result of the analysis based on the data shown in Fig. 5.4(c) and (d) allows us to conclude that line X_R^0 and line X_L^0 are both from the recombination of neutral excitons (X0) while line X^+ and X^+' are the PL recombination with a spectator hole (X^+). We believe that X_L^0 is weaker than X_R^0 because it is energetically favorable for the electron to relax to the lower energy (right) QD.

The red shift of X^+ relative to X^0 differs from the case of single QDs[85, 86] and VQDMs[56], where blue shifts of the X^+ state are typically observed. This red shift is one of the distinct PL properties of LQDMs that has been predicted by both pseudopotential[18] and effective mass[79] modeling. In the X^+ initial state, one electron-hole pair sits in the right QD and the remaining hole in the left QD. If the QDs have very different energies, tunnel coupling is negligible and the electron-hole pair only feels the nearby hole as a static electric field. This reduces the exciton

binding energy leading to a Coulomb-induced red shift. If the QD energies are close enough, the electron may tunnel between the two QDs. This leads to an additional tunnelling-induced red shift of the X^+ emission.[79] In order to determine whether the red shift of X^+ in Fig. 5.4(a) is due to Coulomb coupling or to tunnel coupling, further information is needed. The presence of a splitting between X^+ and $X^{+'}$ lines gives us a hint that it can be interpreted from the comparison with theoretical calculations in order to definitely assign these states to specific charge configurations.

5.3.3 Theoretical fitting

Working with our theory collaborators, we compute the LQDM PL spectra as a function of charge configurations using the model and material parameters described in Ref. [79]. We take a typical distance between QD centers of $d = 35$ nm, and parabolic confinement frequencies of $\hbar\omega_L = 25$ meV and $\hbar\omega_R = 23.5$ meV, consistent with the experimental QD sizes and the energy splitting between X^0_L and X^0_R lines. Since the hole is more confined than the electron, we assume the characteristic lengths to be related by $l_h = 0.6\, l_e$. The energy gap is taken so as to fit the energy of the X^0_R line. The resulting PL spectrum for X^+ is plotted in Fig. 5.4(e).

Similar to the charge configurations in VQDMs, we use the notation $\begin{pmatrix} e_L & e_R \\ h_L & h_R \end{pmatrix}$, where e_L (e_R)) indicates the number of electrons in the left (right) QD in one LQDM. Similarly for holes. For example $\begin{pmatrix} 0 & 1 \\ 1 & 1 \end{pmatrix}$ describes a LQDM with one electron in the right QD and one hole in each QD.

As shown in Fig. 5.4(e), there are two peaks that originate in PL emission from the initial state $\begin{pmatrix} 0 & 1 \\ 1 & 1 \end{pmatrix}$. The presence of one hole in each QD breaks the Coulomb attraction that binds the electron to a single QD and electron tunneling leads to the formation of a delocalized electron state. The delocalized electron can recombine with both holes, in either the left or right QD, and emit PL at slightly different energies. Compared with the direct recombination involving only electron and hole in the right

QD, the indirect X^+ recombination exhibits significant lower intensity because there is a relatively small probability of electron tunneling. This allows us to assign X^+ to the direct recombination of $\begin{pmatrix} 0 & 1 \\ & \\ 1 & 1 \end{pmatrix}$ and $X^{+'}$ to the indirect recombination. The modeling result is also in good quantitative agreement with the data in Fig. 5.4(a).

To explain the relative intensities of multiple X^0 and X^+ PL lines, we consider the dynamics of charge relaxation within the LQDM. Normally, when an e-h pair is optically excited, the electrons relax first and the hole follows, with Coulomb interactions driving the hole toward the same QD as the electron. The electron and hole can relax into either QD, but it is energetically favorable for them to relax into the lower energy (right) QD. By measuring the energy difference between the two X^0 PL lines shown in Fig. 5.4(a) and Fig. 5.5(a), we learn that the X^+ state of LQDM 1 is 1.6 meV below the X^0, which is relatively small. This nearly-degenerate structure enables the optically or electrically injected electrons to relax to both left and right dots when no charges occupy the LQDM. For applied voltage below V1, X^0 PL emission from both the left and right QDs are observed because the electron can relax into either QD and the hole will follow the electron into the same QD. Electron-hole pairs relax more often into the low energy QD (right), therefore, we see $\begin{pmatrix} 0 & 1 \\ & \\ 0 & 1 \end{pmatrix}$ has stronger PL intensities than $\begin{pmatrix} 1 & 0 \\ & \\ 1 & 0 \end{pmatrix}$. Similarly, if the optically-excited electron tunnels out of the QDs and leaves the hole behind, it is energetically favorable for the hole to relax to the bigger QD (right), which has a lower energy confined state. Although the hole tunneling is slower than electron tunneling, the hole lifetime is limited by tunneling escape from the LQDM, not radiative recombination, and thus there is significant opportunity for the hole to relax. The presence of this hole in the right QD drives the electron to localize into the right QD. Consequently, we do not see emission from a positive trion state in which the electron is predominantly located in the left QD (this includes both $\begin{pmatrix} 1 & 0 \\ & \\ 1 & 1 \end{pmatrix}$ and $\begin{pmatrix} 1 & 0 \\ & \\ 2 & 0 \end{pmatrix}$). The optically excited hole will relax into the left QD

because of hole-hole repulsion and serve as a spectator charge during the PL emission $\begin{pmatrix} 0 & 1 \\ 1 & 1 \end{pmatrix}_D$ as a direct recombination. As discussed previously, the interdot tunneling of the single electron allows weak indirect recombination and emitted PL signal marked as $\begin{pmatrix} 0 & 1 \\ 1 & 1 \end{pmatrix}_I$. We observe emission involving both positive trion and neutral excitons in the bias region to the left of V1 because the CCD integrates over multiple optical excitation and emission cycles that randomly contain both X^+ and X^0 events. The relative probability of these events is influenced by the laser power density as described above.

5.4 Charging Sequence in Nearly Degenerate LQDMs

5.4.1 X^- charge configurations

As the applied voltage moves the confined states of the QDs past the Fermi level, additional electrons tunnel into the LQDM. This leads to a sequence of charging events and discrete shifts in the energies of ground state PL emission, as shown in Fig. 5.5(a). In order to understand the mechanism and consequences of this charging sequence in LQDMs, we systemically study the ground state spectra of LQDM 1, as a function of increasing applied voltage, by comparing the experimental PL signatures with the theoretical modeling results. The charge configuration for almost all PL lines in Fig. 5.5(a) are assigned and indicated by the inset labels. We now justify and explain these assignments.

The first observation is that there are four values of the applied voltage (V1 through V4 at which discrete shifts in the PL spectra occur. These shifts occur as the increasing vertical bias moves confined energy states relative to the Fermi level. The increase of the vertical bias drives the conduction band states across the Fermi level and electrically injects electrons one by one as is shown in Fig. 5.5(b).

The first group of PL lines, appearing for voltages above V1, are assigned to $\begin{pmatrix} 1 & 1 \\ 1 & 0 \end{pmatrix}$, $\begin{pmatrix} 1 & 1 \\ 0 & 1 \end{pmatrix}$, and $\begin{pmatrix} 0 & 2 \\ 0 & 1 \end{pmatrix}$, all of which have two electrons and one hole. In each

of these configurations at least one electron is in the right QD. The second, optically generated, electron can relax into either the left or right QD. The hole, which typically relaxes more slowly, can also relax into either QD. We do not observe any lines assigned to $\begin{pmatrix} 0 & 2 \\ 1 & 0 \end{pmatrix}$ because Coulomb attraction makes it unlikely that the hole will relax into a QD with no electrons. The PL emission of $\begin{pmatrix} 2 & 0 \\ 1 & 0 \end{pmatrix}$ can only happen when both the electrically-injected electron and optically-generated electron-hole pair occupy the left QD. Because the conduction level of the left QD is a little higher than the right one, the electrically-generated electron can be injected into the left QD only at voltages slightly higher than V1.

At the same time that the X^- PL lines appear at V1, the X^+ PL line $\begin{pmatrix} 0 & 1 \\ 1 & 1 \end{pmatrix}$ disappears. This occurs because electrical charging of the LQDM with a single electron makes it impossible for a single optically-generated hole to remain in the LQDM. For voltages larger than V1, the PL line $\begin{pmatrix} 1 & 0 \\ 1 & 0 \end{pmatrix}$ gains significant optical intensity. This occurs because the probability that an electron relaxes to the higher energy (left) QD increases in the absence of a single hole in the right QD. Both neutral exciton states are observed at voltages above V1, despite the expectation that the LQDM should be charged with an excess electron. This is because the relaxation of the optically-generated electron into the LQDM can be blocked by both Coulomb and the Pauli interactions with the electron/s already occupying the LQDM. This relaxation blockade can force the electron to remain, temporarily, in a higher energy confined state from which tunneling out of the LQDM is more probable. It is therefore possible to observe PL emission of both charge states near the charging point. Similar processes lead to overlap of emission from other total charge states.[87].

Fig. 5.5(c) compares experimental (dotted lines) and theoretical (solid and dashed lines) PL energies for different excitonic complexes. The dashed lines in the X^+ column represent the PL emissions that are energetically unfavorable, as was discussed

in the last section. Good agreement between experimental and theoretical results is found for X^+ and X^0, as well as for X^- complexes containing all charges within the same QD. However, for X^- with one electron in each QD in the initial states, the theory predicts that $\begin{pmatrix} 1 & 1 \\ 1 & 0 \end{pmatrix}$ and $\begin{pmatrix} 1 & 1 \\ 0 & 1 \end{pmatrix}$ emission energies are blue and red shifted with respect to the corresponding X^0 levels. This is because of the participation of electron's inter-dot tunnel coupling in the final state[79]. By contrast, in the experiment only a slight red shift of both lines is observed, similar to what is seen in VQDMs PL when spectator electrons are placed in neighbor QDs. This result leads us to suspect that the electron tunnel coupling in LQDM 1 may be suppressed for X^- states. This suppression may be related to the different nature of repulsive electron-electron and hole-hole Coulomb interactions. The basin structure between the QD pair could also influence the tunneling strength.[18] The simulations predict the inverted energy of $\begin{pmatrix} 0 & 2 \\ 0 & 1 \end{pmatrix}$ and $\begin{pmatrix} 2 & 0 \\ 1 & 0 \end{pmatrix}$ emissions as a result of the inter-dot tunneling of the electron in the final state [17]. Our experimental techniques do not allow us to confirm this assignment, but it seems consistent with the fact that the former shows up at smaller bias than the latter in Fig. 5.5(a).

5.4.2 X^{2-} charge configurations

As the applied voltage increases beyond V1, a second electron can tunnel into the LQDM. For LQDM 1, shown in Fig. 5.5(b), the confined conduction band energy levels of the two QDs are similar in energy and it is energetically favorable for the second electron to go into the left QD. Although the left QD energy state is at somewhat higher energy than the state of the right QD, this spatial configuration reduces the energy penalty of on-site electron-electron Coulomb repulsion if both electrons are in the right QD. As a result of the electrical injection of a second electron, new PL lines appear for voltages above V2. We assign these PL lines to the $\begin{pmatrix} 1 & 2 \\ 0 & 1 \end{pmatrix}$ and $\begin{pmatrix} 2 & 1 \\ 1 & 0 \end{pmatrix}$ charge

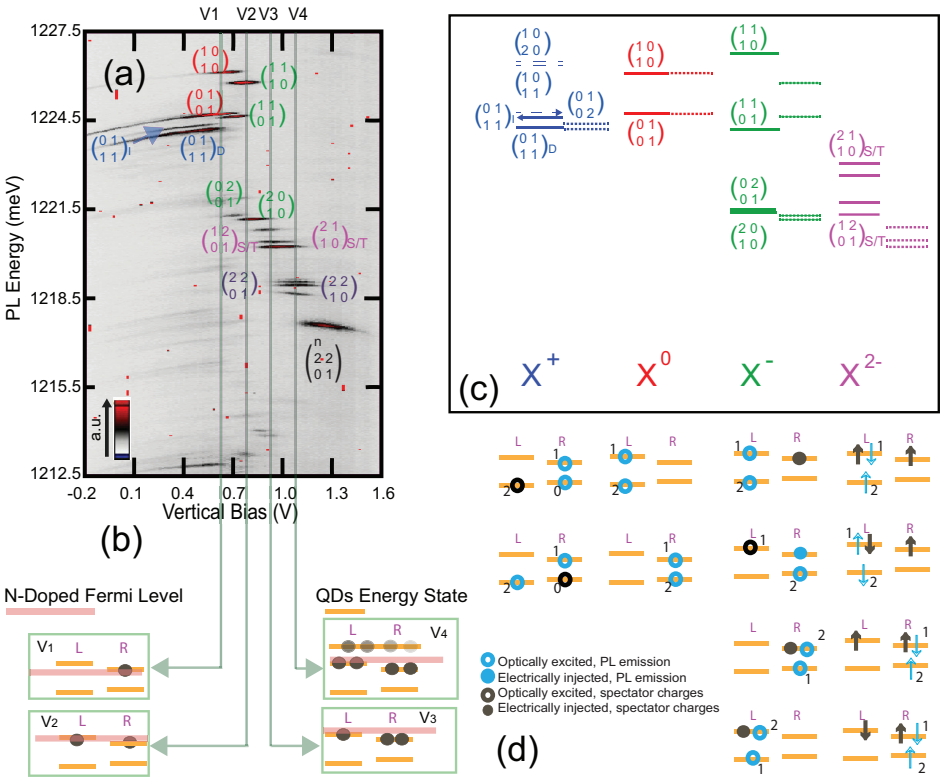

Figure 5.5: (a) Full PL spectra of the ground states transition mapping as a function of vertical voltage measured for LQDM 1. (b) Electrical charging sequence as the applied voltage increases. (c) Comparison between the theoretical (solid and dashed lines in the left half of every column) and experimental (dotted lines in the right half of every column) emission energies from X^{+} to X^{2-}. (d) Depiction of the initial and final states of each PL emission line.

configurations. We observe fine structure in these lines that we attribute to singlet and triplet electron spin configurations in the final state after optical recombination.

As is shown in the X^{2-} column of Fig. 5.5(c), the experimental PL lines are a few meV lower than the simulated PL energies. Yet, the 0.4 meV energy splitting between $\begin{pmatrix} 2 & 1 \\ 1 & 0 \end{pmatrix}$ and $\begin{pmatrix} 1 & 2 \\ 0 & 1 \end{pmatrix}$ emission observed in the data agrees well with the computational prediction.

5.4.3 X^{3-} and higher charge configurations

Continuing to increase the voltage makes it possible for a third electron to tunnel into the LQDM. As a result, X^{3-} charge configurations become visible for voltages larger than V3. In the X^{3-} charge configuration, no spin fine structure is expected to be possible. Three lines and a hint of the fourth line are visible, corresponding to the combination of two initial states and two final states of X^{3-} emission. The small energy separation between each line suggests the perturbation from electron tunnel coupling and the Auger process in between two neighbor QDs.

As the applied voltage increases beyond V4, the ground state of the LQDM is filled with four electrically-charged electrons. Optically generated electrons therefore occupy excited states of the LQDM. These excited states are delocalized over the entire LQDM and there is a relatively small energy spacing between each excited state. Consequently, we observe a quasi-continuous shift of the PL line as increasing numbers of electrons occupy the excited states[88, 18].

To summarize this section, we have provided detailed understanding of the charging process in LQDMs with nearly degenerate QDs by comparing experimental PL data with theoretical estimates and logical relaxation dynamics. The observation of energy shifts computationally predicted to arise from electron tunneling provides strong experimental evidence for the existence of tunnel-coupling for X^{+} (and possibly X^{-}) in this system.

5.5 Charging Sequence in Non-degenerate LQDMs

The detailed analysis presented in the previous section was possible because LQDM 1 happens to have QDs that are nearly degenerate in energy. Because of the self-assembly of LQDMs involves diffusion, the geometrical structure and composition profile can vary significantly between LQDMs. Consequently, many LQDMs with non-degenerate energy states are expected to be present in the sample. We present one example of a non-degenerate LQDM and show how the relaxation dynamics and charge

interaction signatures developed in the previous section can be used to assign observed PL lines that appear dramatically different from the degenerate LQDM case.

Fig. 5.6(a) shows the PL signature of LQDM 2 as function of vertical field. Two PL lines separated by 0.5 meV are observed for negative bias (1212.1 and 1212.6 meV at 0.5V). These PL lines are assigned to the $\begin{pmatrix} 0 & 1 \\ 0 & 1 \end{pmatrix}$ and $\begin{pmatrix} 0 & 1 \\ 1 & 1 \end{pmatrix}$ states following the discussion of positive trion states presented above. Similar to LQDM 1, we can clearly see discrete energy shifts due to Coulomb interactions when the vertical voltage allows one, two and three additional electrons to tunnel into the LQDMs at V1, V2 and V3. The locations of these charges, as shown in Fig. 5.6(b), are different from the degenerate LQDM case because there is substantially larger offset between the confined energy states of the left and right QD. We followed the same model described in the last section to assign the different charge states of each PL emission as marked in Fig. 5.6(a); the probability of relaxing into the high energy QD is much smaller in the case of non-degenerate QDs. We describe the significant differences here.

First, for voltage below V1, only one PL emission from a X^0 state is observed $\begin{pmatrix} 0 & 1 \\ 0 & 1 \end{pmatrix}$. PL line $\begin{pmatrix} 1 & 0 \\ 1 & 0 \end{pmatrix}$, which originates in the emission of the neutral exciton in the higher energy QD, is not observed because the optically excited electrons and holes relax to the low-energy QD faster than optical recombination can occur.

Second, only a single X^+ emission is observed in LQDM 2. As we discussed in the last two sections, the PL doublet for $\begin{pmatrix} 0 & 1 \\ 1 & 1 \end{pmatrix}$ comes from different final states of the hole after electron-hole recombination. In a nearly-degenerate LQDM, a single electron is able to tunnel between two neighboring QDs when there is one hole in each QD. However, in a non-degenerate LQDM, electron tunneling is significantly suppressed and it is impossible for electrons in the right QD to recombine with the hole in the left QD. Therefore, only one emission line is observed in X^+ state.

Third, the PL line $\begin{pmatrix} 1 & 1 \\ 0 & 1 \end{pmatrix}$, which is observed in degenerate LQDMs when the

conduction level of the right (higher energy) QD crosses the Fermi level, is missing in this system. In the non-degenerate LQDM the PL emission from $\begin{pmatrix} 1 & 1 \\ 1 & 0 \end{pmatrix}$ and $\begin{pmatrix} 0 & 2 \\ 0 & 1 \end{pmatrix}$ turns on at this electric field. This change is a consequence of the offset in confined energy states in the non-degenerate LQDM. When one electrically-injected electron has occupied the conduction level of the low-energy QD, the optically generated electron will relax to the energetically favorable QD. In this case, the energy difference between the two QDs is relatively large, which drives the second electron to relax into the QD already occupied by one electron regardless of the Coulomb repulsion. The hole follows the electrons into the right QD and consequently beyond V1, $\begin{pmatrix} 0 & 2 \\ 0 & 1 \end{pmatrix}$ is emitted and $\begin{pmatrix} 1 & 1 \\ 0 & 1 \end{pmatrix}$ is missing. If the electron relaxes into the left QD, it creates a metastable state that rapidly relaxes to two electrons in the right QD. If, however, the hole follows the electron into the left QD, the hole is trapped by its large effective mass and slow tunneling. As a result, the Coulomb binding energy extends the lifetime of this metastable state and PL emission from the $\begin{pmatrix} 1 & 1 \\ 1 & 0 \end{pmatrix}$ state can be observed.

Beyond V2, the applied voltage charges LQDM 2 with two electrons. This charging results in a red shift by 1 meV between PL lines $\begin{pmatrix} 0 & 2 \\ 0 & 1 \end{pmatrix}$ and the X^{2-} states $\begin{pmatrix} 1 & 2 \\ 0 & 1 \end{pmatrix}$ and $\begin{pmatrix} 1 & 2 \\ 1 & 0 \end{pmatrix}$. We observe two discrete PL lines for the X^{2-} state because the two electrically injected electrons relax into the right QD. The optically generated electron relaxes into the left QD rather than occupying an excited state of the right QD. The presence of electrons in both QDs makes it possible for the hole to relax into either QD.

At V3, the electrical injection of the third electron causes a 0.8 meV red shift for the X^{3-} PL emission. Again, a PL doublet is observed, corresponding to the

relaxation of the hole into the left or right QD. The intensities of X^{2-} and X^{3-} PL lines are substantially reduced compared to X^{-} PL lines. We observe significant variation between LQDMs in the PL intensities of highly charged states. We tentatively assign this variation to changes in electron tunneling escape rates from higher energy states, but further work to analyze this effect is necessary.

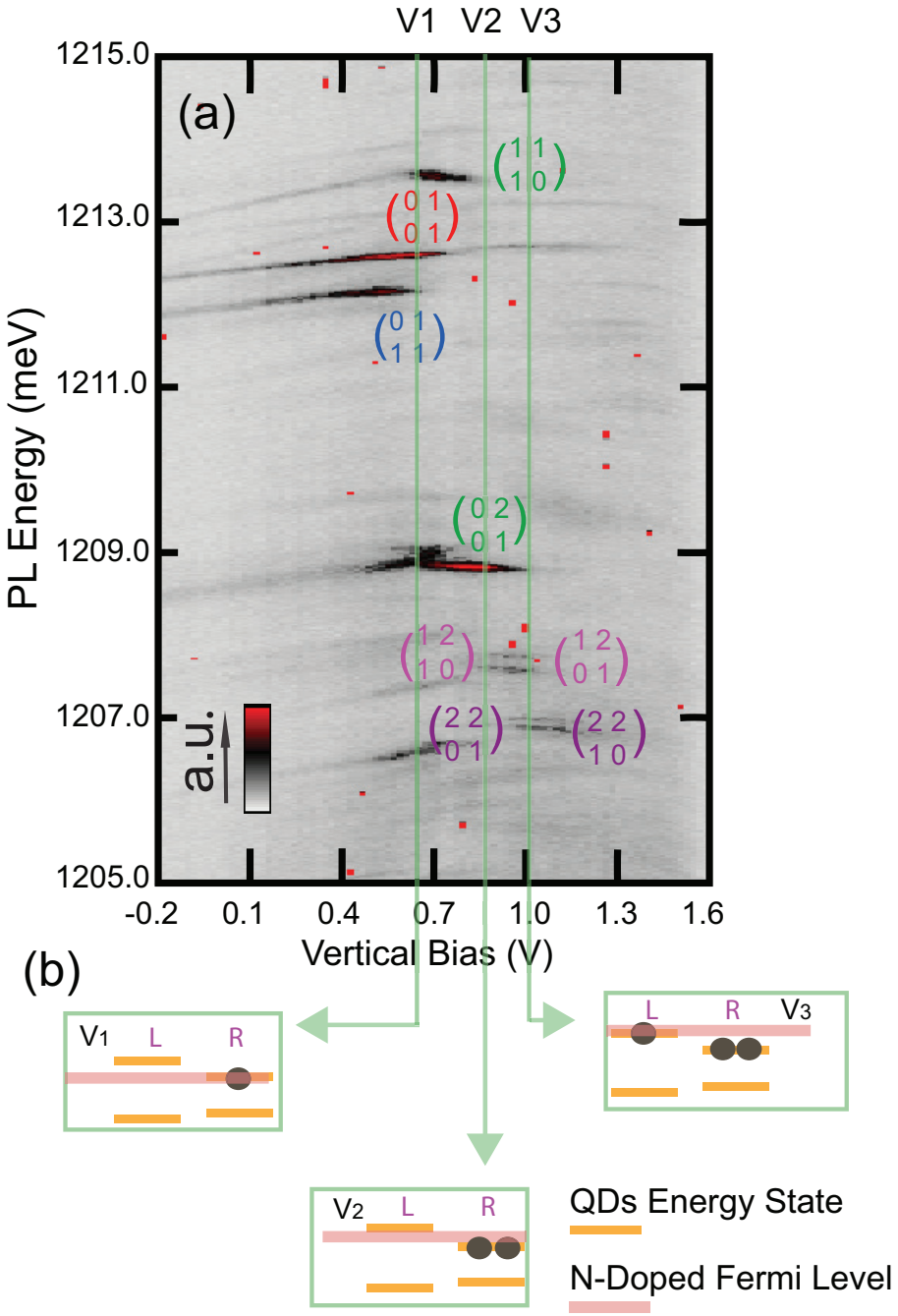

Figure 5.6: (a) Full PL spectra of the ground states transition map as a function of vertical voltage measured for LQDM 2. (b) Electrical charging sequence as the applied voltage increases.

Chapter 6

ENERGY SHELL STRUCTURE OF LATERAL QUANTUM DOT MOLECULES: FIRST EXCITED STATE

6.1 Introduction

In this chapter, we provide experimental evidences that electrons in excited energy levels are delocalized over the entire LQDM. We present optical spectroscopy of ensembles and individual LQDMs as a function of electric fields applied along the growth direction. The results allow us to characterize the energy level structure of LQDMs and the spectral signatures of both charging and many-body interactions. We present experimental evidence for the existence of molecular-like delocalized states for electrons in the first excited energy shell. In Sect. 6.2 we describe photoluminescence (PL) measurements of ensembles of LQDMs and propose a model for the LQDM energy shell structure in which electrons in excited energy shells are delocalized over the entire LQDM. In Sect. 6.3 we use the spectroscopy of individual LQDMs to analyze the consequences of Coulomb interactions. The measured spectral shifts validate the energy shell model and suggest that the excited electron states are delocalized over the entire LQDM. In Sect. 6.4 we report the observation of fine structure which likely originates in spin interactions within the excited electron energy shell. These observations further support the conclusion that the excited electron shell is delocalized over the entire LQDM. These results suggest that this energy shell structure opens up new opportunities to optically control the interaction of spins confined in LQDMs.

6.2 Many-body Interactions in the $ES1_e$-$ES1_h$ Energy Shell

To understand the ES1 shell, we study the ensemble PL of the $ES1_e$-$ES1_h$ transition as a function of applied voltage. Fig. 6.1(a) plots the intensity and center

energy of the PL peak as a function of the voltage applied along the growth direction. Because of the Schottky diode structure, zero applied voltage corresponds to a built-in field 19.2 kV/cm. Increasing applied voltage forward biases the diode, dropping the confined energy levels of the QDMs toward the Fermi level set by the doping. As the applied voltage increases, the intensity of PL emission from the ES1 state increases until saturating at an applied voltage of about 0.4 V. We label this applied voltage $F_{\langle GS \rangle}$ because it corresponds to the applied voltage at which the GS shell of the average LQDM has crossed the Fermi Level. The center energy of the $ES1_e$-$ES1_h$ PL peak remains constant at 1242 meV until $F_{\langle GS \rangle}$, then decreases rapidly to about 1237 meV as the applied field is increased to about 0.7 V, which we label $F_{\langle ES1 \rangle}$. The center PL energy then remains constant at approximately 1237 meV as the applied voltage continues to increase.

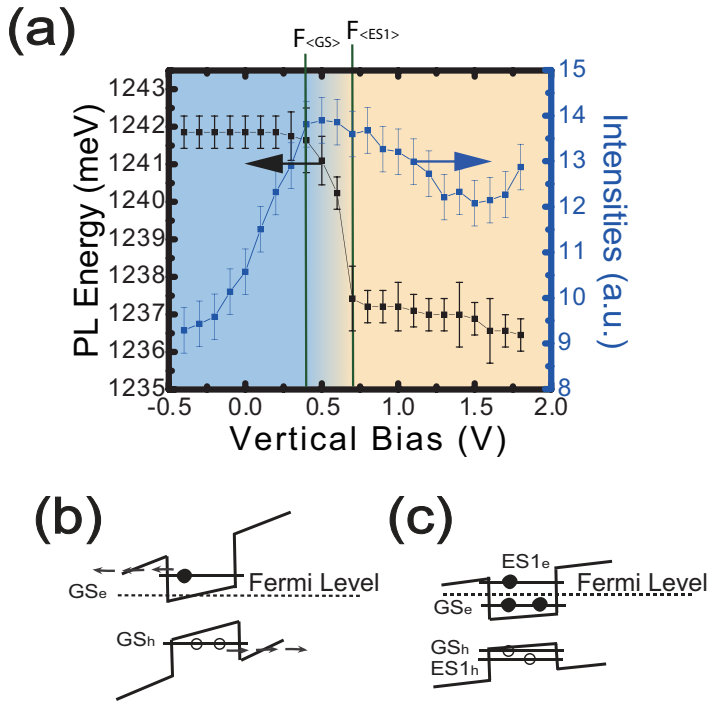

Figure 6.1: (a) PL spectra of the $ES1_e$-$ES1_h$ transition as a function of applied voltage. (b, c) Schematic models of confining potential along the growth direction with no (b) and significant (c) applied voltage, indicating how the applied voltage impacts the filling of excited energy levels.

To explain the intensity dependence of the $ES1_e$-$ES1_h$ PL, we consider the dynamics of electron and hole absorption and relaxation into the ES1 energy shells. The number of electrons and holes captured in the LQDM depends on the applied voltage because it impacts the probability with which optically generated charges are captured and retained in the LQDM, as schematically depicted in Fig. 6.1b and c. We stress that the band diagrams in Fig. 6.1b and c are drawn along the growth axis and thus depict only the vertical confinement in one of the QDs comprising the LQDM. When no voltage is applied, the large built-in electric field creates a relatively thin triangular tunnel barrier for confined electrons and holes, reducing the probability that carriers are trapped in and remain in the QDs (Fig. 6.1b). The confinement for holes is stronger than for electrons because of the large hole effective mass. As a result, single InGaAs QDs and vertical QDMs studied under large built-in electric fields frequently exhibit multiple discrete spectral lines associated with positively charged exciton configurations.[8, 10, 43, 56] The confinement of both electrons and holes is substantially weaker for excited energy states, making it improbable that a carrier population can be trapped in the ES1 states.

As the applied voltage increases, the net electric field decreases and the confining potential becomes more like a square well (Fig. 6.1(c)). Trapping and retention of electrons becomes more probable and the intensity of emission from the $ES1_e$-$ES1_h$ PL transition increases. The intensity saturates near the applied voltage at which the GS states cross the Fermi level ($F_{\langle GS\rangle}$) because the GS states become electrically charged by electrons tunneling from the Fermi level. As a result, at applied voltages larger than $F_{\langle GS\rangle}$ virtually all optically generated electrons are populating the ES1 states and the probability of emission from this state no longer strongly depends on the applied voltage.

The red shift of the center of the $ES1_e$-$ES1_h$ PL peak between $F_{\langle GS\rangle}$ and $F_{\langle ES1\rangle}$ is explained by charging and many-body interactions within the ES1 energy shell. The dynamics of charging described above indicate that, for applied voltages less than $F_{\langle GS\rangle}$, the probability that electrons populate ES1 is relatively small. The average electron

occupancy of the ES1 energy shell is therefore less than one, but we only observe emission from the $ES1_e$-$ES1_h$ transition when at least one electron is present in ES1. As the applied voltage is increased beyond $F_{\langle GS\rangle}$, the probability of electron escape from $ES1_e$ decreases and the average electron occupancy of the ES1 energy shell begins to increase. Many-body interactions between the electrons filling the ES1 energy shell lead to the red shift in emission of the $ES1_e$-$ES1_h$ PL. This red shift with increasing electron occupancy is consistent with the typical behavior of single InGaAs QDs and VQDMs.[89, 42] As the applied voltage continues to increase, the ES1 shells of the LQDMs begin to cross the Fermi level and become electrically charged with additional electrons. The center of the ES1 ensemble PL peak red shifts rapidly because the average electron occupancy of the ES1 shell increases dramatically. When the applied voltage reaches $F_{\langle ES1\rangle}$ the ES1 shells of almost all LQDMs have been fully occupied by electrons tunneling from the Fermi level and the red shift ceases. The ensemble average red shifts by 5 meV between $F_{\langle GS\rangle}$ and $F_{\langle ES1\rangle}$.

6.3 Spectral Signatures of Coulomb Interactions in First Excited States

Further information on the energetic position and degree of localization of energy shells can be obtained from the spectroscopy of single LQDMs. We now show that the single LQDM spectra validate the model that electrons in excited energy shells are delocalized while the excited-shell holes remain localized in a single LQD. In Fig. 6.2 we present the discrete spectral lines of a single LQDM measured in both the GS (b) and the ES1 (a) energy shells. Vertical lines labeled F_{GS} and F_{ES1} indicate applied voltages where discrete shifts in the PL spectra are observed in both energy shells. We attribute the first discrete shift (F_{GS}) to Coulomb interactions that arise when the applied voltage tunes the GS shell below the Fermi level and additional electrons begin to occupy the GS shell. We attribute the second discrete shift (F_{ES1}) to charging of the ES1 shell. The observation that discrete shifts in the energy of PL transitions within the GS (ES1) energy shell occur when the ES1 (GS) energy shell crosses the Fermi level confirms that both of these energy shells are part of the same LQDM.

The applied voltages at which the GS and ES1 shells of the single LQDM are charged ($F_{GS} - F_{ES1} = 0.12$ V in Fig. 6.2) correspond to a 6 to 26 meV energy separation of the GS and ES1 shells of this LQDM. Obtaining a more precise value for the GS-ES1 energy shell separation in this LQDM requires knowing the spatial location of the LQDM between the top electrodes, which we cannot measure.

To develop a more detailed understanding of Coulomb interactions and assess the spatial extent of wavefunctions associated with the ES1 energy shell, we systematically analyze the spectral map presented in Fig. 6.3a. Fig. 6.3a plots the observed $ES1_e$-$ES1_h$ PL emission of a single LQDM, different from that presented in Fig. 6.2, as a function of applied voltage. At low applied voltage two discrete PL lines separated by 2.1 meV are observed (A and B). The PL intensity of lines A and B is weak because the probability that electrons occupy the ES1 energy level is low. There are three possible origins for this pair of spectral lines: 1) recombination involving energy levels of the two distinct QDs that comprise the LQDM, 2) recombination of two different charge states of the lowest energy QD, and 3) recombination from the lowest energy QD with and without the presence of an extra spectator charge in the other QD.

The A-B peak separation of 2.1 meV is at least four times larger than the spectral shifts typically observed when spectator charges occupy the neighboring QD of a VQDM, where shifts are typically less than 0.5 meV for QDs separated by less than 10 nm. The QD separation in these LQDMs is much larger ($\sim$ 40 nm) and the Coulomb interactions between charges localized in separate QDs are therefore expected to be much smaller. As a result, the assignment of the discrete spectral shifts to recombination in the lowest energy QD with and without spectator charges in the neighboring QD can be excluded. Because line A and B show identical shift features with applied voltage, the possibility that these two lines are emitted by two QDMs with different locations can be excluded. We assign the two discrete lines (A and B) to recombination of an electron in the lowest energy ES1 state under two different configurations of holes. We analyze the dynamics of charge relaxation into the QDs, the dependence of the relative intensity of PL lines A and B on applied voltage, and

the observed spectral shifts to show that the ES1 electron state is delocalized while hole states in both the GS_h and $ES1_h$ shells are localized in one of the two QDs that comprise the LQDM (e.g. $ES1_{hL}$ and $ES1_{hR}$).

Experiments and calculations on LQDMs indicate that electrons relax more rapidly than holes. Electrons can relax into either of the two QDs that comprise the LQDM (e.g. E_{0L} or E_{0R}) and typically relax into the QD with the lowest energy levels.[90] The QD with lowest energy levels depends on the applied lateral electric field, but in the conditions studied here the applied lateral field is small and changes only slightly with applied voltage, as discussed above. We therefore conclude that the difference in energy levels is dominated by the natural variation in QD energy levels arising from growth inhomogeneity. We further assume that the energy ordering of the states associated with the two QDs does not change with applied voltage. We cannot determine which QD has lower energy states, but for consistency in the discussion we will continue to assume that the left QD has lower energy levels, following our schematic in Fig. 5.1(c).

Holes relax more slowly than electrons and typically fall into the same QD as the electron due to Coulomb interactions.[90] When the electric field is large, optical charging tends to populate positively charged exciton states, as described above. This optical charging is a quasi-random process, and multiple charge states can be observed in the time-integrated PL spectra.

The charge state assignments for transitions labeled in Fig. 6.3(a) are depicted in Fig. 6.3(c). The electron and hole participating in the excitonic recombination are colored blue and all spectator charges are colored black. We stress that we cannot verify the total charge configuration for each transition. In particular, there may be fewer spectator charges than we depict in Fig. 6.3(c). However, the *changes* in charge occupancy depicted in Fig. 6.3(c) explain the energy differences between PL lines measured in the data. We first present the charge configurations tentatively assigned to each PL line and show how changing Coulomb interactions in the different configurations predict energy shifts consistent with the measured data. We then show

that these measured Coulomb interactions support our conclusion that the ES1 energy shell is delocalized while the GS_h and $ES1_h$ shells are localized to single QDs.

In single InGaAs QDs and VQDMs, the addition of a single hole to a single QD typically increases the energy of PL emission from that QD by 2-3 meV.[10, 43, 42] We therefore assign PL line A to recombination of an electron from $ES1_e$ to $ES1_hL$ when the GS_e and GS_h states are filled and there are no additional holes in H_{1L}. We assign PL line B to the same charge configuration as transition A with the addition of one hole in $ES1_hL$. This assignment is supported by the relative intensities of PL lines A and B as a function of applied voltage, as depicted in Fig. 6.3(b). As the applied voltage increases, the probability of populating the ES1 and $ES1_h$ levels increases, so the intensity of both PL lines increases. However, the probability of generating an excess hole population *decreases* with increasing applied voltage. As a result, the intensity of the positively charged exciton (PL line B) decreases with respect to PL line A.

As the applied voltage in Fig. 6.3a increases beyond F_{GS}, a new spectral line (C) appears. This line starts with low intensity, but increases in intensity as the applied voltage is increased. The small energy shift between lines A and C ($\sim$ 0.31 meV) suggests that PL line C arises from Coulomb interactions with a charge localized in the right QD. We attribute this PL line to emission of the ES1 to H_{1L} transition in the presence of an additional spectator hole in the right QD (see Fig. 6.3(c)). At applied voltages less than F_{GS} the occupation of the high energy (R) QD by holes is less probable because the electron localizes to the low energy (L) QD and the hole follows. Charging of the GS_{eR} and GS_{hR} states therefore occurs only when optical excitation injects multiple electron hole pairs. At applied voltages greater than $F_{<GS>}$, however, electrons occupy both the GS_{eL} and GS_{eR} states. Consequently, Coulomb interactions no longer favor relaxation of the hole into the low energy (L) QD. The probability of observing a spectator hole in the right QD therefore increases after the applied voltage crosses the Fermi level, consistent with the assignment of PL line C to the $ES1_e$ to $ES1_{hL}$ transition in the presence of an additional spectator hole in the right QD.

As the applied voltage in Fig. 6.3(a) increases beyond $F_{<ES1>}$, a series of strong, discrete PL lines appears (D-G). Lines D through G do not all gain significant optical intensity at the same value of applied voltage. Rather, line D become optically bright at 1.00 V, with lines E-G gaining optical intensity at 1.08, 1.17, 1.31 V respectively. This sequential appearance of the PL lines suggests that the lines are associated with the sequential charging of the ES1 states with single electrons as the states cross the Fermi level. The charge configuration for PL line D is depicted in Fig. 6.3(c) and lines E, F, and G are assigned to filling of the ES1 energy levels with 3, 4, and 5 electrons, respectively. The applied voltage at which each additional electron enters the LQDM depends on both the exact energy level of each state within the ES1 shell and Coulomb interactions with the other electrons occupying the LQDM. Each time a charge is added, the PL energy red shifts by approximately 2 meV (A-D: 2.25 meV, D-E: 1.87 meV, E-F: 1.53 meV, F-G: 2.59 meV. The red shift is consistent with the energy shift observed in other InGaAs QDs upon charging with additional electrons.[42]

If two charges are localized in separate QDs, the wavefunctions associated with the charges have minimal overlap. Consequently, the shift in PL energy due to Coulomb interactions between charges localized in separate QDs is small, of order 0.5 meV. Shifts of this magnitude are observed for PL line C in Fig. 6.3, supporting the conclusion that the hole states are localized in individual QDs. However, all red shifts observed upon charging with additional electrons (lines D-G) are of order 2 meV. This large shift is indicative of strong Coulomb interactions and suggests that the electron wavefunctions overlap strongly. We thererfore conclude that the ES1 states are delocalized over the entire LQDM. If states of the ES1 shell are delocalized, states of the ES2 shell must also be delocalized. This analysis is the basis of the schematic depiction of delocalized states in Fig. 5.1(c). We note that the localization or delocalization of the H_2 states cannot be determined from the presently available data.

We note that Fig. 6.3(a) and Fig. 6.2(a) both show discrete red shifts in the spectra of single LQDMs as the applied voltage increases beyond $F_{<GS>}$ and $F_{<ES1>}$. These data are representative of the spectral shifts we have measured in nearly 20 LQDMs

and agree with the red-shift due to many-body interactions presented in Fig. 6.1 for an ensemble of LQDMs. However, the model presented in Fig. 6.3(c) does not adequately explain the energy separation between discrete spectral lines presented in Fig. 6.2(a). We suspect that differences in the composition profile and energy level separation in different LQDMs can lead to a variety of spectral features. For example, LQDMs in which GS_{eL} and GS_{eR} differ by only a few meV may have different spectral features than those LQDMs in which the difference is larger. These differences in spectral features could arise because of the competition between optical emission and charge relaxation dynamics, which is influenced by the energy level separation. More investigation of the energy levels and charging dynamics is necessary to develop a more general model of the LQDM spectral properties.

6.4 Spin Fine Structure in a Single LQDM

Further evidence for the delocalized nature of the ES1 energy levels is provided by the observation of fine structure in the highly charged exciton states (D-G), as shown in Fig. 6.3(d). Fine structure typically arises in PL spectra when more than one spin configuration is possible in either the initial or final states. Electrons have spin projections $\pm\frac{1}{2}$. Holes in QDs are properly described as spinors with both light and heavy hole character, though the heavy hole component typically dominates the spinor.[91] The light hole components can have a significant impact on the properties of coupled QDs,[92, 93] but the assumption that holes have only heavy hole character with spin projections $\pm\frac{3}{2}$ is a reasonable first approximation. Optical selection rules require recombining electrons and holes to have opposite spin projections, so dark exciton states, where the electron and hole have parallel spin projections, are not observed.[1] The Pauli exclusion principle requires two charges occupying a single energy level to be in a spin singlet configuration. As a result, neutral exciton and singly charged (negative or positive) exciton transitions do not have spin fine structure. Spin fine structure

[1] We ignore anisotropic exchange interactions, which typically introduce energy splittings of less than 100 μeV, comparable to the resolution of our spectrometer.

becomes possible only in charged exciton states where there are two unpaired spins in either the initial or final state of optical recombination.

Transitions A-C in Fig. 6.3 all involve recombination where spin fine structure is not expected. Neither the initial nor final state of transition B has more than one unpaired spin. The initial state of transition A has an unpaired electron and unpaired hole, but the dark exciton spin configurations cannot be observed. Transition C has two unpaired holes, but experiments on VQDMs indicate that singlet and triplet configurations of holes localized in separate QDs are degenerate in energy unless coherent tunneling between the energy levels leads to a kinetic exchange interaction.[51] Because the two QDs that comprise the LQDM typically have slightly different energy levels, coherent coupling is unlikely in the absence of any lateral field to tune the energy levels into resonance.[90] The absence of spin fine structure associated with line C further supports the conclusion that the $ES1_h$ energy levels are localized to individual QDs.

Once the applied voltage tunes the ES1 shell past the Fermi level, electrons begin to fill the states that comprise the ES1 shell. The order in which these states will be filled depends on charge and spin interactions.[42] Whenever the initial state or final state of optical recombination has unpaired electron spins, multiple possible spin configurations are possible and spin fine structure is probable. In Fig. 6.3(d) we indicate several weak PL lines that gain optical intensity at the same value of applied voltage as the strong PL lines D and E. Although we cannot assign these spectral lines to specific charge and spin configurations, the applied voltage controls the number of electrons that occupy the ES1 shell. Consequently, a pair of lines that gain optical intensity at the same value of applied voltage most probably originate from states with the same total charge. The observation of fine structure for line D suggests that the two electrons occupying the ES1 shell are located in different discrete energy states. If these states were localized in individual QDs, the energy shifts due to Coulomb or spin interactions would be expected to be very small (0.5 meV or less). The observed shifts are all more than 1meV (D: 1.27 meV, E: 2.16 and 3.23 meV), further supporting the conclusion that the ES1 energy states are delocalized over the entire LQDM.

Unlike controlled charging of single InGaAS QDs,[42] there is not a well-defined window of applied voltage in which the PL of a single charge configuration dominates. This suggests that the charge occupancy of the LQDM ES1 state is not well defined for any value of applied field. States with increasing charge occupancy do not become populated until the applied voltage tunes the ES1 energy states sufficiently below the Fermi level to overcome Coulomb interactions and add an additional electron to the ES1 energy shell. For this reason the PL transitions originating in states with increasing number of electrons gain optical intensity at increasing values of the applied voltage. However, optical recombination of electrons in the ES1 states competes against emission from the GS states, which removes electrons and enables electron relaxation out of the ES1 states. Consequently, states of lower charge occupancy can continue to emit even at applied voltages where higher charge occupancy is possible.

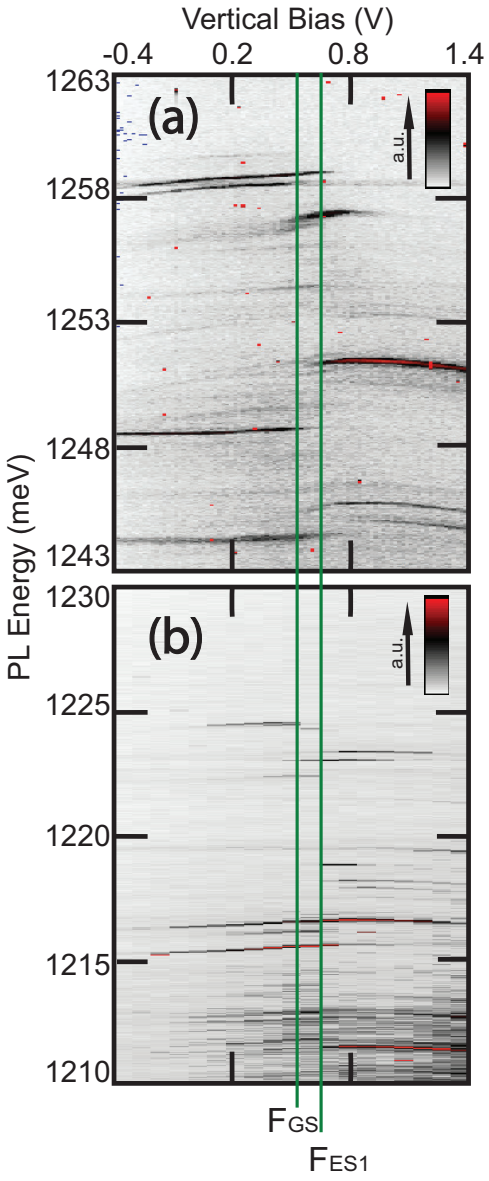

Figure 6.2: PL spectra of the GS_e-GS_h (b) and $ES1_e$ to $ES1_h$ (a) transitions in a single LQDM as a function of applied voltage. Vertical lines indicate the applied voltage at which the GS and ES1 energy shells cross the Fermi level. Panel (a) is measured with about twice the exciting laser power used in panel (b) in order to populate the ES1 energy shell. Scale bars in the top right corner indicate the colors associated with increasing PL intensity.

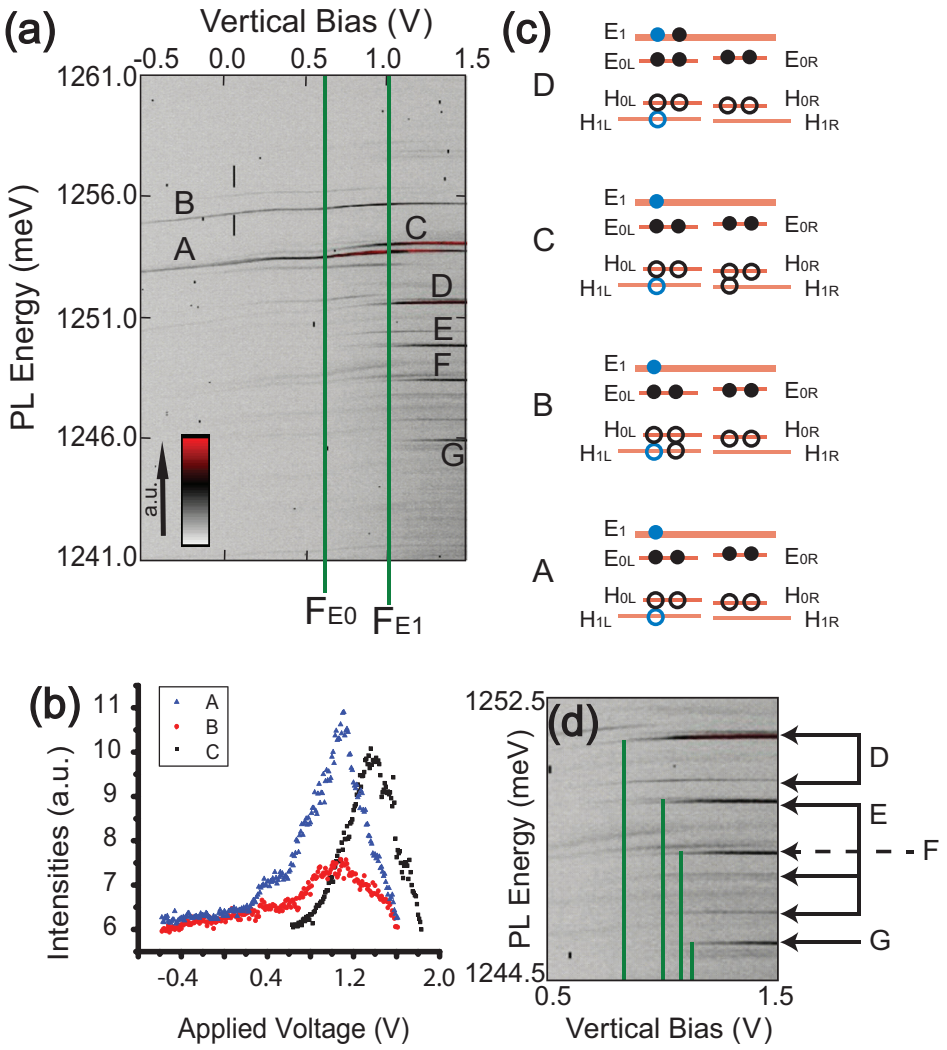

Figure 6.3: (a) PL spectrum of the $ES1_e$-$ES1_h$ transitions in a single LQDM as a function of applied voltage. The scale bar at the bottom left corner indicates the color mapping of increasing PL intensity. (b) Intensity of PL lines A, B and C as a function of applied voltage. (c) Depiction of the charge configuration assigned to each labeled transition as described in the text. (d) Close up of panel a showing possible spin fine structure correlations.

Chapter 7

SPECTROSCOPIC SIGNATURES OF LATERAL QUANTUM DOT MOLECULES UNDER MAGNETIC FIELD

7.1 Introduction

In this chapter, we use magneto-optical spectroscopy to study both ground and excited states of individual LQDMs. We uncover the underlying physics that explains the energy shifts of discrete states of individual InAs lateral quantum dot molecules (LQDMs) as a function of magnetic fields applied in the Faraday geometry. We observe that ground states of the LQDM exhibit a diamagnetic shift while excited states exhibit a paramagnetic shift. We explain the physical origin of the transition between these two behaviors by analyzing the molecular exciton states with effective mass calculations. We further show that the net effects of broken symmetry of the molecule and Coulomb correlation lead to the paramagnetic response. We also present preliminary results suggesting that Zeeman splittings in the ground states of LQDMs which depends on the charge occupancy. We attribute the variation of Zeeman splitting and g factor to the wavefunction extent for charge carriers, which is shown in chapter 5 to be influenced by the charge occupancy in the LQDMs.

7.2 Differentiating the Discrete PL Peaks from GS and ES1

Based on the methods introduced in the last two chapters, we are able to assign the discrete PL peaks to different energy shells by measuring the discrete PL intensities as a function of laser power. A typical result for this power-dependent measurement is shown in Fig. 7.1(a). With increasing laser power density, the increase of the PL intensities of the three peaks with low energy (marked as G1, G2 and G3, see Fig. 7.1(b)) rise sub-linearly with a change in slope at a laser power density of approximately 125

W/cm^2. In contrast, the intensities of peaks on the high-energy side (see Fig. 7.1(c)) increase superlinearly with increasing laser power. The different trends of these two groups of lines indicates that PL line G1, G2 and G3 are emitted from the ground shell of the LQDMs (GS) while E1, E2 and E3 are from the first excited shell (ES1)[88]. We have also noticed that the Stark shift of PL lines in different shells varies. These two methods allow us to assign PL lines to specific energy shells.

7.3 Magneto-optic Experimental Results of PL in GS and ES1

We focus on the GS PL lines with higher-than-average energies to improve detection efficiency with our Si-based CCD. Emission from the GS and ES1 is easily distinguished by observing characteristic applied voltage and laser power dependence trends in the PL data as discribed above.[88, 94] Fig. 7.2a shows the typical magnetic field dependence of PL emission from the GS and ES1, measured on two different LQDMs. The GS exhibits a 0.6 meV blue-shift as the magnetic field is increased to 6T and a Zeeman splitting that reaches 0.3 meV. Over the same range of magnetic field ES1 exhibits a strong red shift (about 3.5 meV). Although the lines broaden slightly, no Zeeman splitting in the ES1 PL is observed within the range of magnetic fields studied. The continuous and smooth energy shifts and the full PL spectral maps (not shown) confirm that the number of charges in each LQDM does not change as a function of magnetic field.

The PL energy of QD ground states as a function of magnetic field is typically fit with an equation of the form:

$$E_{pl}(B) = E_{pl}(0) \pm b_{ex}B + a_{ex}B^2 \tag{7.1}$$

where $E_{pl}(0)$ is the PL energy at 0 T, b_{ex} is the linear coefficient and a_{ex} is the quadratic coefficient. Typically, in GS emissions, the linear term $\pm b_{ex}B$ corresponds to the Zeeman splitting and b_{ex} is given by $1/2\mu_B g_{ex}$, where g_{ex} is the exciton g factor and μ_B is the Bohr magneton. The quadratic term $a_{ex}B^2$ typically comes from the diamagnetic shift. By fitting the GS data in Fig. 7.2a with this equation, we are able

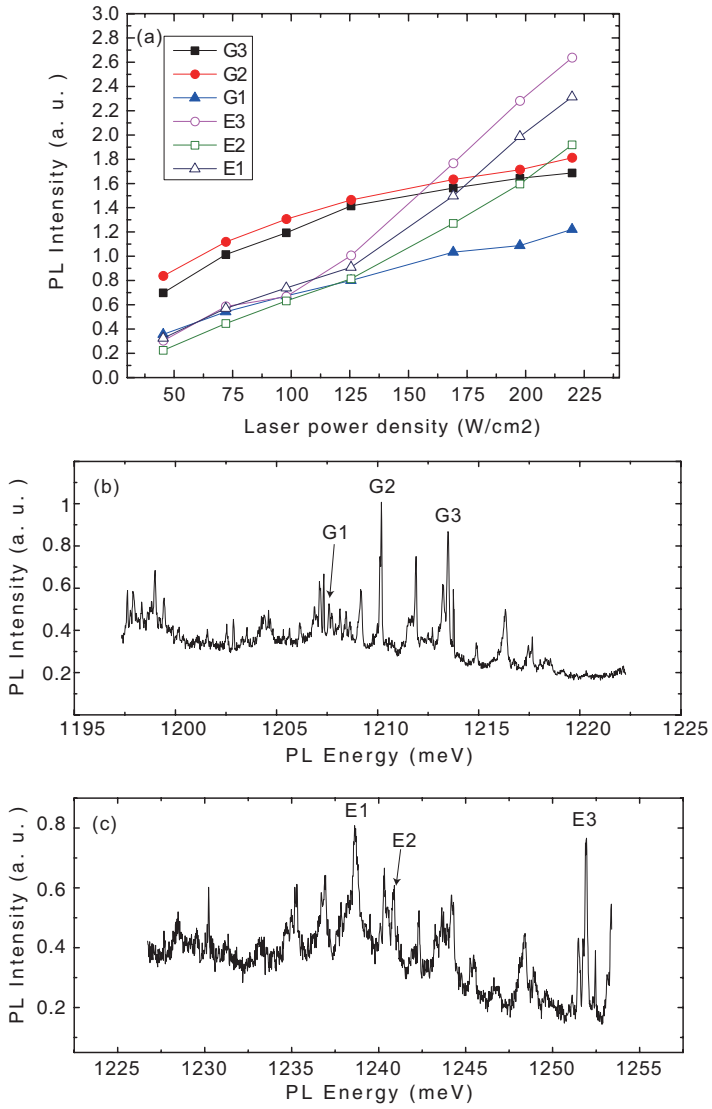

Figure 7.1: (a) Dependence of photoluminescence intensity of discrete spectral lines emitted from LQDMs excited by a laser with power ranging from 50 to 225 W/cm^2. The PL peak labels correspond to discrete ground (b) or excited (c) states evident in the line spectra.

to extract the g factor and diamagnetic coefficient. For the PL emission of ES1, we set b_{ex} to zero because no Zeeman splitting is observed. The fit value for a_{ex} is negative, in contrast to the positive value for the ground state PL. This negative a_{ex} quantifies the paramagnetic shift for the excited state that is evident in Fig. 7.2a.

We apply the same fit to the magnetic-field dependent PL data of 25 distinct ground states and 23 distinct excited states of LQDMs. The values of a_{ex} returned by these fits are plotted in Fig. 7.2b as a function of PL wavelength. The average a_{ex} for GS PL (solid symbols) is 11.73 μeV/T^2 and the standard deviation is 4.27 μeV/T^2. This value is consistent with the diamagnetic coefficient observed for ground states of single InAs QDs and vertically-stacked QDMs.[95, 96] The average value of a_{ex} for ES1 PL (open symbols), on the other hand, is -65.36 μeV/T^2, approximately 6 times larger in magnitude and opposite in sign. The standard deviation of a_{ex} in ES1 is 19.59 μeV/T^2. Although red shifts of the excited state PL of single QDs have been previously observed,[97] this effect originates in the circular symmetry of the single QD, a symmetry that does not exist for delocalized states of an LQDM.

7.4 Theoretical Explanation to the Paramagnetic and Diamagnetic Shift of LQDMs

7.4.1 Theory details

The theoretical calculation is done by our collaborators J I Climente and M Royo in Universitat Jaume I, Spain. We use single-band two-dimensional effective mass calculations to explain the physical origin of the pronounced red shift in the ES1 PL. The single particle Hamiltonian, is integrated using three-point finite differences on a two-dimensional grid. The magnetic field is implemented with the symmetric gauge. Gauge invariance of the finite-difference discretization was checked by comparison with an alternative discretization formalism that averages the wave function in the B^2 term, as done e.g. in Ref. [98]. Exciton eigenstates and eigenfunctions are obtained using a configuration interaction (CI) method in the basis formed by the 36 (48) lowest electron (hole) spin-orbitals. Coulomb integrals are obtained

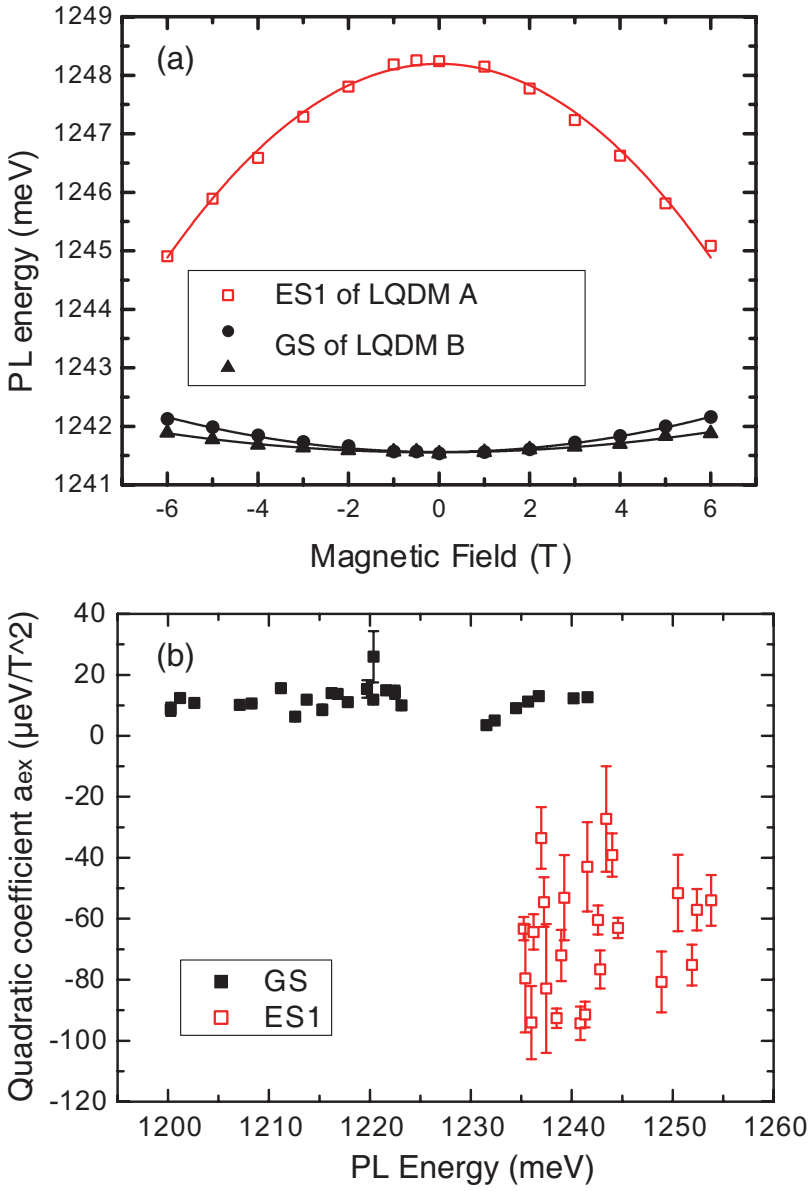

Figure 7.2: (a) Energies of typical PL lines (GS, ES1) from two representative LQDMs as a function of magnetic field. (b) Diamagnetic coefficients for discrete PL lines from different energy shells of LQDMs as a function of PL energy.

using the Fourier transform convolution theorem. The CI matrix is built and diagonalized using the CItool software.[1] The resulting exciton states are of the form $\Psi(\mathbf{r_e}, \mathbf{r_h}) = \sum c_{ij}\phi_i(\mathbf{r_e})\,\phi_j(\mathbf{r_h})$, where ϕ denotes a single-particle spin-oribtal. The emission intensity is estimated within the dipolar approximation as proportional to the square of the electron-hole overlap, considering holes as complex-conjugated electrons, $I \propto |S_{eh}|^2 = |\sum_{ij} c_{ij} \int \phi_i(\mathbf{r_e})^* \phi_j(\mathbf{r_h})^* \delta(\mathbf{r_e} - \mathbf{r_h})\, d\mathbf{r_e}\, d\mathbf{r_h}|^2$.

We consider an exciton confined in the LQDM, described by the Hamiltonian $H_X = H_e + H_h + V_{eh}$. Here V_{eh} is the Coulomb interaction between electron and hole and H_e and H_h are the electron and hole single-particle Hamiltonians:

$$H_i = \frac{\mathbf{p}^2}{2\,m_i^*} - \frac{q_i B}{2\,m_i^*} L_z + \frac{(q_i B)^2}{8\,m_i^*}(x^2 + y^2) + V_c^i, \tag{7.2}$$

where m_i^* is the effective mass of the electron ($i = e$) or hole ($i = h$), q_i is the charge ($q_e = -1, q_h = 1$), B is the vertical magnetic field, $L_z = (xp_y - yp_x)$ the azimuthal angular momentum and V_c^i the confining potential. Hereafter we refer to the linear-in-B term of H_i as H_i^{B1}, and to the quadratic-in-B term as H_i^{B2}. We neglect the Zeeman effect, which is not relevant for determining the red shift of ES1. Hamiltonian H_X is solved using a configuration interaction method to account for Coulomb interactions. We use the same material parameters and confining potential that previously showed good agreement with experimental measurements of a nearly-degenerate LQDM from the same sample at zero magnetic field.[94] We note that considering a single exciton in excited states neglects quantitative corrections that may arise for ES1 PL due to the presence of additional excitons forming a closed shell in the lower-energy states. In single QDs such corrections have been estimated to be no more than 1 meV.[99]

7.4.2 Charge densities of LQDMs under magnetic field

As shown in Fig. 7.3, at $B = 0$ T the GS charge densities of both electrons (left panels) and holes (right panels) are localized in individual QDs. For the first excited state, the hole is also mainly localized inside one QD (left dot), but the electron is

[1] https://code.google.com/p/citool/

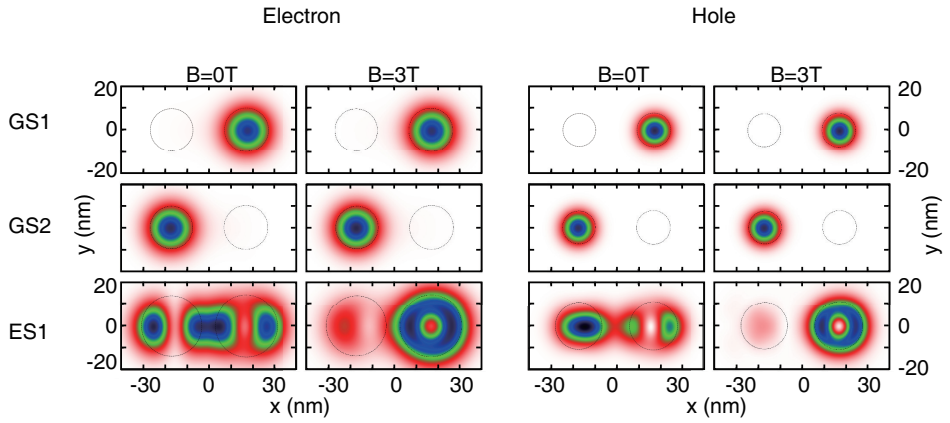

Figure 7.3: Electron (left panels) and hole (right panels) charge densities corresponding to the three relevant exciton states at $B = 0$ T and $B = 3$ T. Dashed line circumferences depict the characteristic length of the harmonic oscillators defining each QD calculated for the electron and hole states with the largest contribution in the exciton wave function.

clearly delocalized over the whole LQDM, forming a molecular orbital. This picture is consistent with that inferred in previous experiments on LQDM as described in the previous chapters.[88] When the magnetic field is switched on, $B = 3$ T, the GS charges remain largely unaffected. By contrast, the excited electron becomes trapped in the right QD, and the hole follows behind bound by Coulomb interaction. In other words, the magnetic field turns off the molecular character of the excited state.

7.4.3 Exciton emission spectrum as a function of magnetic field

Next, we compute the exciton emission spectrum as a function of B. The result is shown in Fig. 7.4(a). Black dots are used for emission from the two GS, red dots for emission from ES1 and gray dots for other transitions (e.g. "forbidden" transitions such as an electron in a GS recombining with a hole in ES1). The size of the dots indicates the optical intensity, estimated within the dipolar approach.[79] One can see that the theory captures qualitatively the magnetic response observed in Fig. 7.2, with a moderate diamagnetic shift of the GS transitions and a larger, non-linear paramagnetic shift of the optically active ES1 transitions.

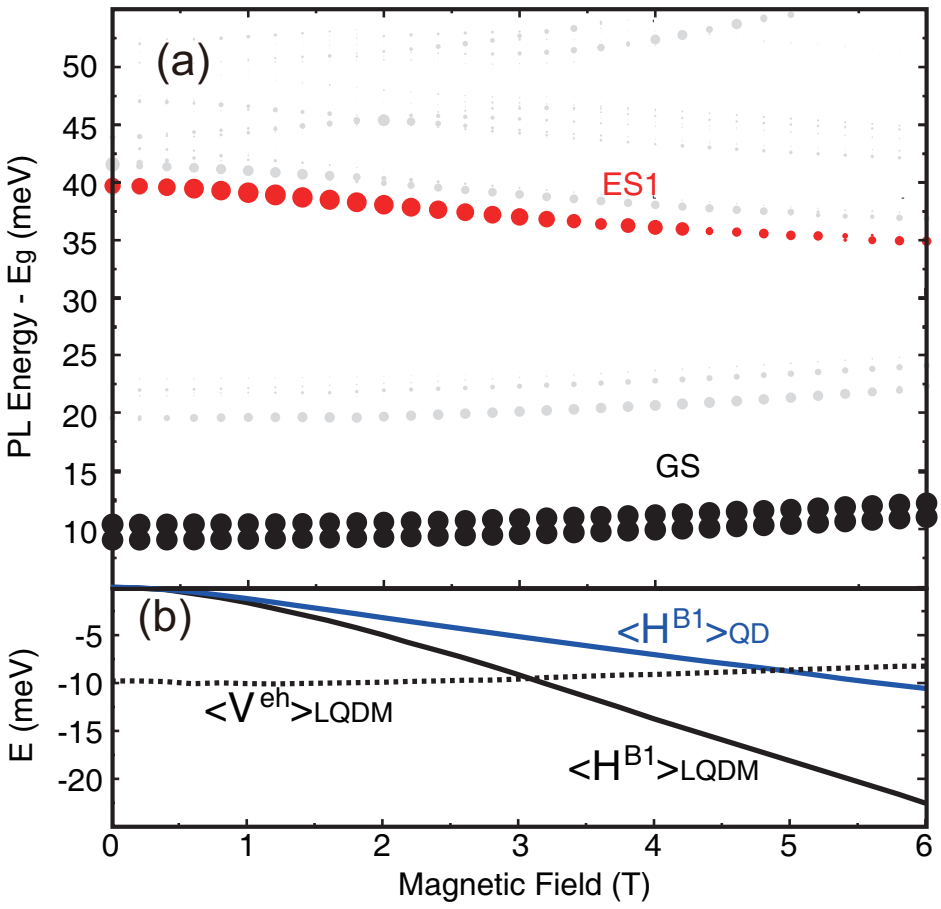

Figure 7.4: (a) Exciton emission spectrum as a function of magnetic field. Black dots are used for GS1 and GS2, red dots for ES1 and gray dots for other non-relevant exciton states. The size of the dots is proportional to the optical intensity. (b) The expectation values of Coulomb interaction (dashed) and linear-in-B single-particle terms for a LQDM (solid black) and a QD (solid blue).

7.4.4 Expectation value of the angular momentum

The electron angular momentum expectation value $\langle L_z^e \rangle$ corresponding to the the optically active p-shell exciton behaves differently for a single QD and LQDM. In a single QD, $\langle L_z^e \rangle$ smoothly decreases from 0 to -1 atomic units as the magnetic field B increases (see red dots in Fig. 7.5). In contrast, $\langle L_z^e \rangle$ in the quasi-degenerate LQDM fluctuates and evolves from 0 towards negative values well under -1 (see blue dots in the figure). The LQDM behavior follows from the lack of circular symmetry in the system and it contributes the large paramagnetic shift displayed in Fig. 7.4.

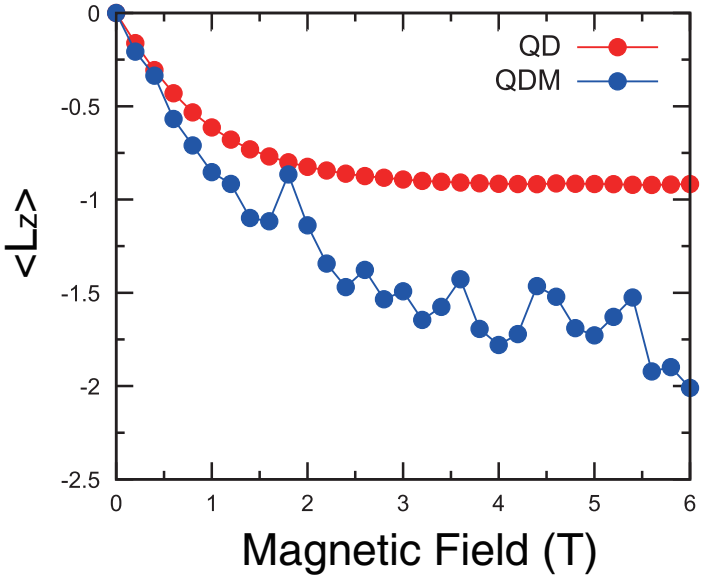

Figure 7.5: Angular momentum expectation value for the electron in a p-shell exciton of a single QD (red dots) and that of a quasi-degenerate LQDM (blue dots). For the single QD $\hbar\omega = 25$ meV. For the LQDM $\hbar\omega_L = 23.5$ meV (left dot) and $\hbar\omega_R = 25.0$ meV (right dot). The distance between QD centers is 35 nm.

7.5 Discussion

7.5.1 Origin of the paramagnetic shift in ES1

As evident in Fig. 7.2(a), it is straightforward to identify the quadratic-in-B term, H_e^{B2}, as the origin of the diamagnetic shift with increasing field in GS shells

because L_z=0 in circular symmetry and the linear-in-B terms in Eq. 7.2 vanished. In contrast, for ES1 states H_e^{B2} is necessarily positive and L_z is not well-defined. There are two factors potentially responsible for the paramagnetic (red) shift of ES1: (1) an enhancement of the electron-hole Coulomb interaction, V_{eh}, as the increasing magnetic field localizes the electron into the same QD as the hole and (2) the linear-in-B single-particle terms, $H^{B1} = H_e^{B1} + H_h^{B1}$. To identify the physical origin of the paramagnetic shift we compare the expectation value of these two terms for the optically active ES1 exciton. The results, displayed in Fig. 7.4(b), clearly show that $\langle V_{eh} \rangle$ has a slight blue shift and the net red shift originates in the H^{B1} term.

The above result is surprising in two senses. First, the Coulomb attraction gives no contribution to the paramagnetic shift (rather the opposite) in spite of B driving the electron and hole into the same QD. This is because the field lifts exciton quasi-degeneracies, thus reducing Coulomb correlations that helped increase electron-hole attraction. Second, it is not obvious that H^{B1} should give a red shift in an LQDM. H^{B1} does induce a red shift in single QDs with nearly circular symmetry,[97] but in such a case L_z is a good quantum number and the optically active p-shell exciton is mainly formed by an electron with $L_z^e = -1$ and a hole with $L_z^h = +1$. Both H_e^{B1} and H_h^{B1} contribute to the exciton red shift in a single QD, though H_e^{B1} is primarily responsible due to the lighter electron mass. In a LQDM, however, the symmetry is drastically lowered and the states have no well defined L_z. One may then expect $\langle L_z^e \rangle \approx 0$, as predicted e.g. in laterally coupled quantum rings.[100] $\langle L_z^e \rangle \approx 0$ would suppress the paramagnetic shift, but we find exactly the opposite behavior. If we compare the red shift induced by $\langle H^{B1} \rangle$ for the LQDM and one of the constituent QDs alone (see Fig. 7.4(b)), the former is twice larger. Indeed, the angular momentum expectation value $\langle L_z^e \rangle$ is found to increase rapidly with B, soon reaching $L_z^e = -2$. As a consequence, ES1 in the LQDM shows a pronounced red shift. The overall red shift is similar for single QD and LQDM because other terms like H_e^{B2} compensate.

This behavior is explained as follows. The B-induced carrier localization into the QDs makes the LQDM emission spectrum resemble that of two individual, nearly

degenerate QDs (cf. Fig. 7.4 with Fig. 2 of Ref. [101]). At the same time, the lowered symmetry enables mixing between states which would otherwise have different L_z. In particular, for the electron it allows strong mixing between the states that eventually converge to the lowest Landau level, which in the single QD would have $L_z^e \leq 0$. As a result, $\langle L_z^e \rangle$ rapidly decreases with B.

7.5.2 Energy shift under magnetic field for LQDMs in different degree of degeneracy

The extent of molecular orbital formation and symmetry breaking in LQDMs depends strongly on the energy degeneracy of the two QDs that comprise the molecule.[94] Although the high areal density of LQDMs in our sample makes it impossible to conclusively assign ES1 PL to a LQDM with degenerate vs non-degenerate GS, we can use theoretical models to estimate the influence of changing degeneracy.

Fig. 7.6 shows the calculated exciton emission spectrum and exciton charge densities of LQDMs with different interdot spacing and degrees of degeneracy under magnetic field. Red dots are used to highlight the molecular exciton state. Although the spatial localization of charges in ES1 depends strongly on the inter-QD degeneracy, no significant change in the paramagnetic energy shifts is observed. The non-degenerate LQDMs can be considered as a system with properties between a single QD and a LQDM with nearly-degenerate constituent QDs. In non-degenerate LQDMs the increase of the angular momentum with increasing magnetic field is weaker than in quasi-degenerate LQDMs while the Coulomb attraction increases more quickly. The net effect of these two factors leads to a 5 meV energy shift when $B = 6T$ regardless of the degree of degeneracy.

7.6 Preliminary Research Results: Zeeman Splitting of LQDMs

7.6.1 Introduction

In addition to the paramagnetic shift and diamagnetic shift in different energy shells of the LQDMs, the Zeeman splitting in the LQDM GS also reveals signatures

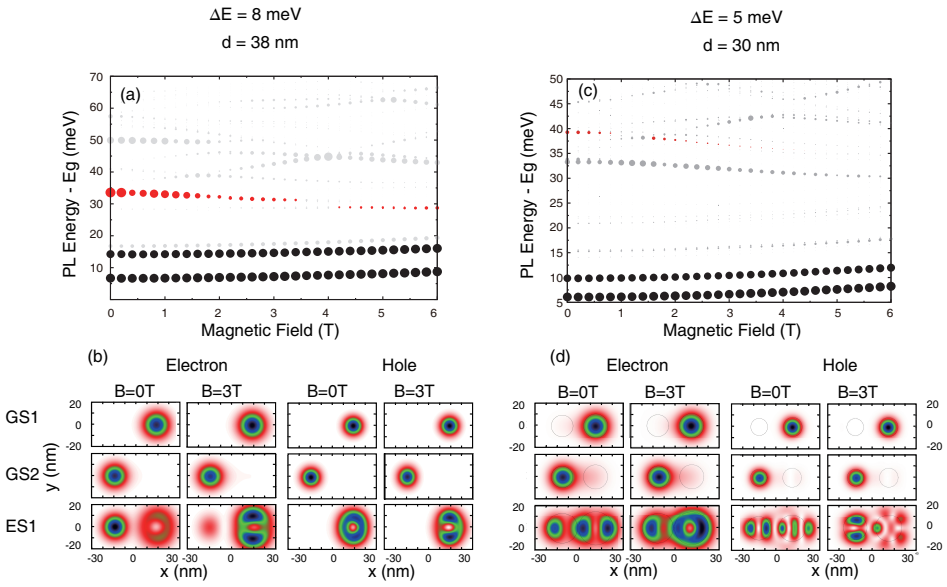

Figure 7.6: Calculated exciton emission emission spectra (top row) and exciton charge densities (bottom row) of LQDMs with different degrees of degeneracy.

of the delocalization in the LQDMs. We are currently working on explaining our preliminary experimental results of Zeeman splitting in different charge states in GS. In the current discussion, we only considered the extension of the wavefunctions of electrons and holes under the influence of the charge states. To better understand the change of the g factors in LQDMs, calculations based on the atomatic structure of LQDMs are necessary.

7.6.2 Experimental results

In chapter 5, the charge confinement in different charge states in GS1 of LQDMs have been studied by electro-magneto-photoluminescence spectroscopy. With the increase of the vertical electric fields applied to the LQDMs sample, a set of PL lines with different PL energy appear sequentially. These lines can be assigned to various charged exciton states following the rules described above.[94] These PL lines show both Zeeman splitting and diamagnetic shift when magnetic fields are applied. Fig.

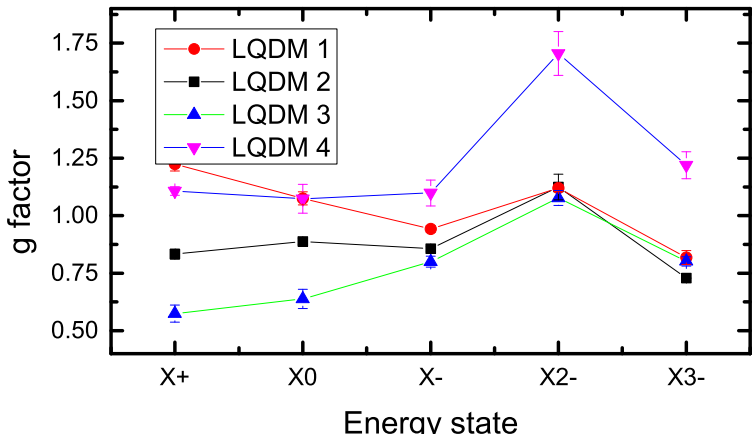

Figure 7.7: g-factors measured from 4 distinct LQDMs

7.6.3 Qualitative discussion: g-factors in LQDMs with different charge states and degrees of degeneracy

The fluctuation of $|g|$ between different LQDMs can be qualitatively explained by the distribution of the geometries of the LQDMs.[102] However, the fluctuation of $|g|$ in different charge configurations in one single LQDM is also commonly observed as a distinct behavior in LQDMs. It has been shown that in a strongly confined system such as single QDs, the Zeeman splitting for all GS recombinations is identical because (1) they are always given by the sum of the g factors of the recombining electron and hole and (2) electronic band structure does not change with the charge states.[44] We attribute the difference of $|g|$ to the change of confinement caused by the arrangement of charges in single LQDMs. The net contribution of Coulomb effects and spin blockade in different states influence the wavefunction extension and the amplitude of the wave function in the GaAs barriers. Therefore, $|g|$ for an electron or hole in the initial/ final states of different charge configurations must be considered to have different values. This observation contrasts with the observation in single QDs and suggests new opportunities for optically manipulating Zeeman splitting and spin

projections in LQDMs.

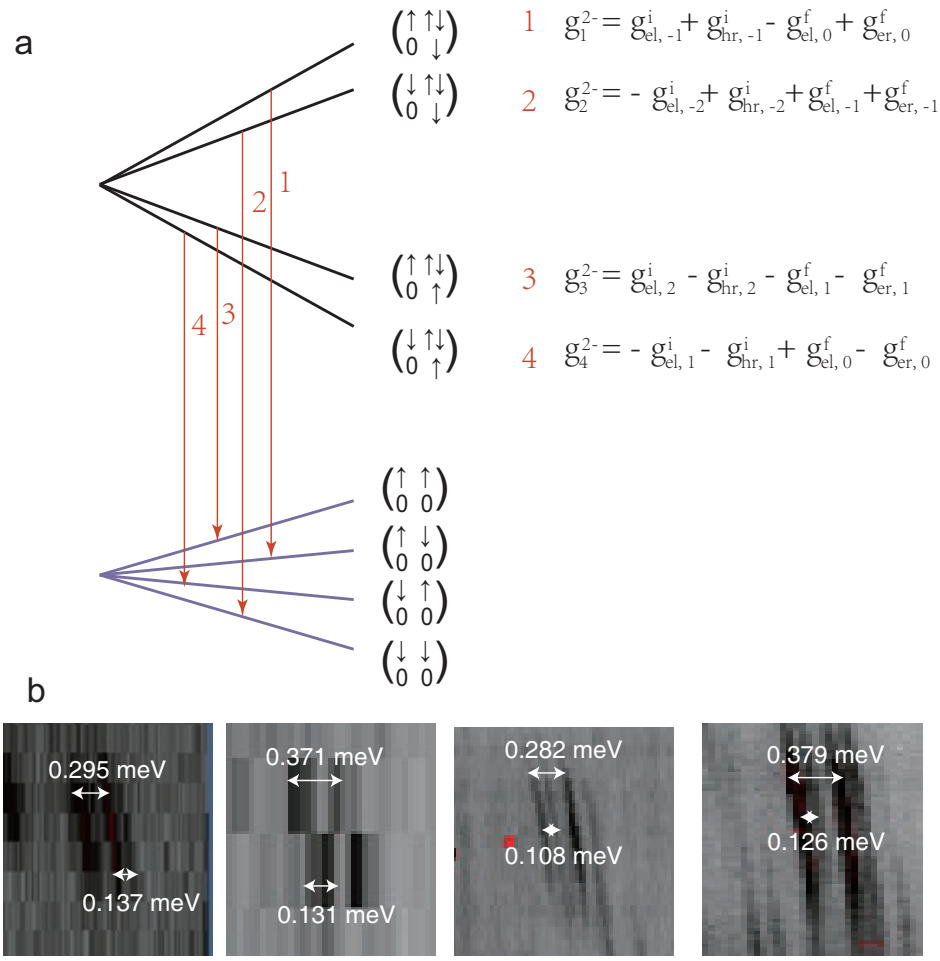

Figure 7.8: (a) The initial and final states of X2- states in LQDMs and g factors associated with them. (b) The bias maps of four LQDMs that shows X2- states. ΔE_{Zeeman} and ΔE_{fine} energy splitting is labeled on top and bottom of each bias map.

A common signature that can be observed in all 4 examples is that the X^2- state shows a larger $|g|$ than the energy state with 1 or 3 spectator electrons. Except for the case in LQDM 1, X^2- always shows the largest $|g|$ among all the states in the same LQDMs. To explain it we turn to the g factors of initial and final states of X^2- emissions.

To simplify the discussion we follow our rule of always assigning the right QD as the low-energy one. The initial state of X^{2-} can be identified as $\begin{pmatrix} 1 & 2 \\ 0 & 1 \end{pmatrix}$ and the final state must be $\begin{pmatrix} 1 & 1 \\ 0 & 0 \end{pmatrix}$. The four allowed recombination pathways for X^{2-} and net $|g|$ in each case are listed in Fig. 7.8. We continue to use the notation $\begin{pmatrix} e_L & e_R \\ h_L & h_R \end{pmatrix}$, where e_L/ e_R denotes the number of electrons in the left/ right dot, and similarly for holes. X^Q denotes the charge states, in which Q is the net charge of the exciton. $g^{i/f}_{e/h,r/l,k}$ denotes the g factor of the electron (e)/ hole (h) in the right (r)/ left (l) QD in the initial (i)/ final (f) states with total spin projection of k.

Because the charge occupation in initial and final states are different, g_{eL} in the initial and final states are different and this leads the PL peak of X^{2-} to split into quadruplets under the magnetic field. This has been observed in experiment, as is shown in Fig. 7.8(b) by the emergence of 4 distinct PL peaks. The four PL lines can be divided into two groups with a high intensity one on the low-energy side and a low intensity one on the high-energy side. The difference of the intensities can be explained by the spin-flip relaxation process that happens between two states with small energy separation.

The energy splitting between two strong PL lines (denoted as ΔE_{Zeeman}) is about twice larger than the splitting within each group (denoted as ΔE_{fine}). Using the model shown in Fig. 7.8(a), we obtain

$$\Delta E^{X^{2-}}_{Zeeman} = 1/2\mu_B B(g^i_{hr,2} + g^i_{hr,1} + g^f_{er,0} + g^f_{er,1} - g^f_{el,0} + g^f_{el,1}) \tag{7.3}$$

and

$$\Delta E^{X^{2-}}_{fine} = 1/2\mu_B B(g^i_{hr,1} - g^i_{hr,2} + g^i_{el,1} + g^i_{el,2} - g^f_{el,0} - g^f_{el,1} + g^f_{er,0} - g^f_{er,1}) \tag{7.4}$$

Our previous work indicates that the single hole will be localized in the dot with lower energy even if the electron number in the both QD is same. With the existence

of one more electron in the right (lower energy) QD, we can confirm that in the initial state, the wavefunction of the single hole is localized in the right dot. Therefore, the g factor of the single hole is comparable to the g factor of holes in X_0.

The electrons in the final states should be discussed based on the degeneracy of the LQDMs. In the steady state of a non-degenerate LQDM states, two electrons tend to both occupy the right QD. Therefore, the final state with spin projection of 0 is unstable and the wavefunction of the left QD is extended over the entire LQDM. For the final state with spin projection of 1, the two electrons have the same spin orientation and the wavefunction of the electron on the left is trapped in the left QD. However, the wavefunction of the right electron is always localized in the right QD, which result in a g factor comparable to the g factor of electrons in X^0. In this case, we can attribute the increase of g factor from X^0 to X^{2-} to the value of $-g^f_{el,0}+g^f_{el,1}$). Both theory and experiments imply that dots with smaller lateral confinement have a more negative g factor[102, 103]. The negative value of $-g^f_{el,0}+g^f_{el,1}$) adds to the negative g factor of the exciton and leads to an increase in the Zeeman splitting.

In contrast, in the nearly-degenerated LQDM system, the final state has one electron in each QD. Therefore the difference of Zeeman splitting between X^0 and X^{2-} is not significantly observed. Similarly, the energy of the fine structure splitting in X^{2-} can be simplify as $\Delta E^{X^{2-}}_{fine} = 1/2\mu_B B(g^i_{el,1}+g^i_{el,2}-g^f_{el,0}-g^f_{el,1})$ which is non-zero when the lateral confinement of the left electron is different in the initial and final states. In the non-delocalized states of LQDMs, the fluctuations of g factor for excitons with charge states of X^{1+}, X^0, X^{1-} and X^{3-} are relatively small. This is because the confinement of the initial and final states in these charge configurations does not depend on the charge configurations. The small perturbation of the confinement alters the g factors within error bars. In the example of nearly-degenerate LQDMs, the fluctuation of g factor is large because charge carriers are allowed to tunnel in some spin configurations. However, substantial theoretical analysis is needed in order to quantify the influence of each charge/ spin configurations. The large g factor in X^{1+} state implies the possibility

of the hole tunneling in the initial state of $\begin{pmatrix} 0 & 1 \\ 1 & 1 \end{pmatrix}$.

.

Chapter 8

DESIGN OF VECTOR ELECTRIC FIELD DEVICE FOR SELF-ASSEMBLED QUANTUM DOT COMPLEXES

8.1 Introduction

In this chapter, we first present a 4-electrode device compatible with optical excitation and emission that allows application of electric fields with arbitrary magnitudes and angles relative to isolated QD complexes. We demonstrate the electric field tunability of this device with numerical simulations. The design introduced in this chapter has been published in Journal of Applied Physics.[104] In the last section of this chapter, a simplified optical device design including 3 electrodes is briefly introduced, which serves as a back up plan for the vector field control of LQDMs.

8.2 Motivations

Current QD device architectures apply electric fields in only one direction, along [105, 88, 94, 67, 106] or perpendicular to [17, 90, 107, 108] the growth direction. Future optoelectronic devices would gain substantial functionality from the application of "vector" electric fields that control both the magnitude and angle of the electric field applied to individual QDs or QDMs.

It is well-known that QDs can be controllably charged by application of electric fields along the growth direction. These electric fields which tune the confined energy levels of the QDs relative to the Fermi level set by a doped substrate. In the case of single QDs, tunable vector electric fields can manipulate the wavefunction overlap in random directions, which enables dynamic control over the exciton states. One important application is to control the fine-structure splitting (FSS) by manipulating the wavefunction overlap of electron and holes.[41, 109] Mar et al. reported that the

FSS in single self-assembled QDs can be reduced from 50 μeV to 7 μeV under an electric field applied along the elongated crystal direction of the QDs. In the case of vertical QDMs, a vertical electric field controls *both* the total charge occupancy and the relative energy levels of the two QDs, which controls the tunnel coupling and the formation of molecular states with unique properties. Application of electric fields with lateral components to vertical QDMs could be used to break the molecular symmetry, which is known to enable new spin mixing phenomena with important technological applications.[92, 36] One big strength of LQDMs is that the tunnel coupling between neighboring QDs could be controlled by electric fields along the molecular (QD-to-QD) axes independent from the growth direction electric field that controls the doping.[88]

8.3 Design Criteria For Vector Electric Field Device Incorporating LQDMs

Table. 8.1 summarizes the design criteria for the vector electric field device. Because controlled nucleation of InAs QDs at pre-determined locations remains challenging, one of the significant challenges for a "vector" electric field device is to simultaneously control lateral and vertical electric fields for QDs or QDMs at arbitrary locations between the electrodes. Another challenge is to design electrodes that apply relatively uniform lateral electric fields to LQDMs that have a large lateral separation between the QDs. Ideally, the electrodes would also serve as an aperture that isolates single QDs or QDMs for quantum device applications. The third challenge is to prevent electron injection from the lateral electrodes by incorporating dielectric tunnel barriers between the electrodes and the QDs. The possibility of pinning the Fermi level at the interface between the dielectric and QD host materials such as GaAs must be carefully considered as this would disrupt the application of controlled vector electric fields. We incorporate one possible solution to this problem in our design, but passivating surface states in multi-layer devices remains challenging.[110, 111]

Table 8.1: Design criteria for vector electric field device incorporating LQDMs

Property	Target Value	Motivation
Aperture size	$\sim$1 μm	Isolate single QDMs[88] at densities of $\sim 30/\mu m^2$ Allow optical measurements with lasers of 800-1000 nm wavelength Allow fabrication by optical lithography
Distance from QDs to doped layer	$\leqslant$ 120 nm	Adequate charge tunneling rate[87, 105]
Minimum lateral field uniformity	$\geqslant$ 50 nm	Uniform lateral field over a LQDM[112]
Max lateral field	$\geqslant$0.5 MV/m	Tune the relative energy difference between LQDMs by at least 10 meV[94]
Max leakage current	$\leqslant$ 100 mA	Prevent excessive heat generation and sample damage

8.4 3-electrode Device For Vector Field

The simplest way to fabricate a device that might apply vector electric fields to QDs or QDMs is to create a single back contact and two split electrodes on the top surface. Fig. 8.1(a) shows the design for such a 3-electrode device. The advantage of the 3-electrode design is that it could be fabricated with only one photolithography and lift off step. However, as we will show, the performance of this device is severely limited. The top electrodes, separated by a 1 μm gap, serve as both lateral gates and an aperture for isolating single QDs. This device can apply a vertical electric field to the center of the aperture by applying voltages with the same magnitude and same sign (relative to the back contact) to the two electrodes on the top surface. This device can similarly apply a lateral electric field to the center of the aperture by applying voltages with the same magnitude and opposite sign to the two top electrodes. To illustrate the limitations of this design, we present device simulations generated with COMSOL Multiphysics of the uniformity and tunability of the electric fields that can be applied.

Fig. 8.1 (b,c) shows that the three-terminal device could apply a lateral and vertical electric field to a QD complex in the center of the aperture (point B). However, the fields that can be applied are highly nonuniform across the aperture, as shown by the differences between points A and B in Fig. 8.1(b,c). The non-uniformity of the vertical electric field arises because of the relatively large lateral and vertical separation between the top electrodes and the center of the aperture. The vertical electric field applied at the center of the aperture (Point B of Fig. 8.1 (b)) is four times smaller

than the electric field under the electrodes (Point A). As a result, most of the device, which is covered by the metal electrodes, will reach flat-band voltage and exceed the allowed leakage current before the electric field at point B is large enough to charge the QDs. Similarly, the non-uniform lateral field arises because of the back contact that cannot be at the same potential relative to both lateral contacts. Moreover, it is difficult to apply a uniform lateral field to QDs that are not located at the center of the aperture, a condition that is inevitable with present QD growth technologies. Resolving these challenges with only two top electrodes is prohibitive. A modified 3-electrode design (not shown) includes a pair of electrodes surrounding the QDs and on the same horizontal plane as the QD layer. Such a design can apply uniform lateral electric fields, but cannot apply vertical fields because the QDs are not covered by electrodes.

8.5 4-terminal Device For Vector Electric Field

To meet the design criteria for electric fields in both vertical and lateral directions, we turn to a 4-electrode device. Conceptually, one pair of electrodes applies a lateral electric field while the other applies a vertical electric field. By combining the two electric fields, we are able to apply a two-dimensional vector electric field to a lateral or vertical QDM at an arbitrary location within the device. The device design also allows the isolation and controlled optical interaction with a single QD or QDM. Fig. 8.2 shows a schematic three-dimensional view of the device incorporating a LQDM sample. The distance between the QDM and the doped layer must be sufficiently thin that electrons can tunnel into the device to charge the QDM but sufficiently thick that sequential charging by one electron at a time can be controlled. The distance between the QDM and the sample surface impacts the change in field required to step through charging events; a larger distance makes discrete charging robust against small fluctuations in the electric field. Initial parameters for these thickness values were set based on our previous experience with QDM structures applying electric fields only in the growth direction. The device parameters we report below were obtained by iteratively

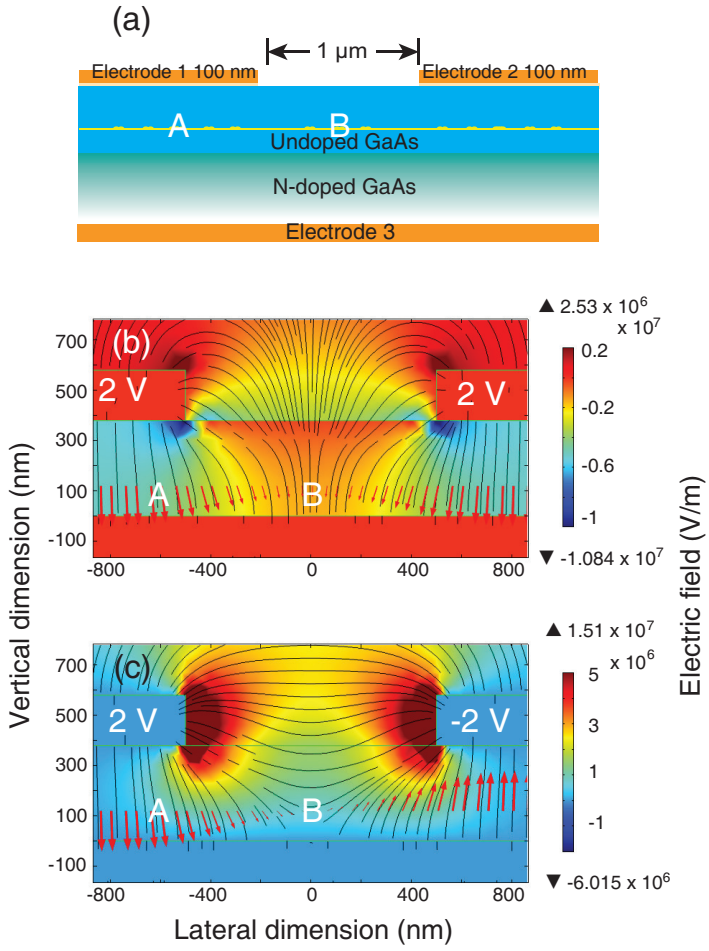

Figure 8.1: a) Schematic diagram of 3-terminal device. (b,c) Electric field distributions in the 3-terminal device when applying (b) pure vertical or (c) pure lateral electric field as measured at the center of the aperture. The color shows the intensity of electric fields along (b) growth direction or (c) molecular axis; the electric field lines are shown in black; the arrows show the direction and magnitude of the electric field along the location of the LQDMs layer.

optimizing to maintain control of charging while maximizing the electric fields applied at the QDM under fixed voltages.

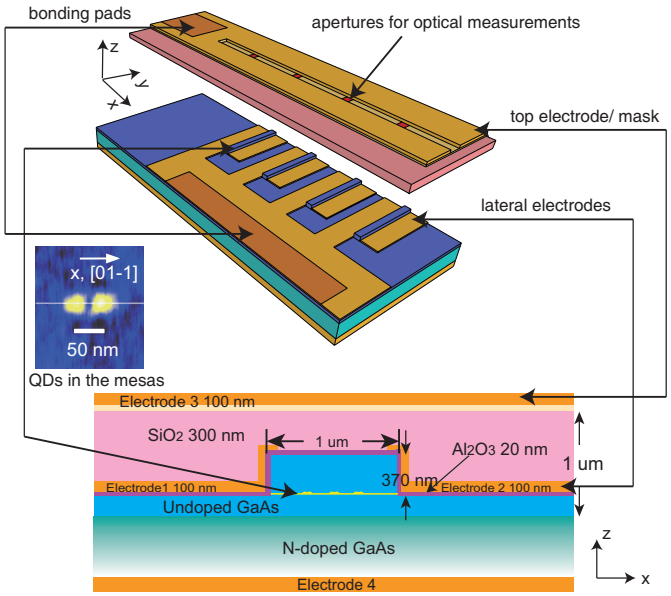

Figure 8.2: Schematic diagram of 4-electrode device design in perspective view (top) and cross-sectional view (bottom). An atomic force microscopy image of a single lateral QDM inside the mesa is shown in the inset.

As is introduced in chapter 3, the molecular axis of the LQDMs naturally orients along the [0 1 -1] axis of the GaAs crystal due to anisotropic diffusion. The distance from the QDMs to the doped layer is set at 120 nm and the distance between the QDMs and the top surface of the sample is 330 nm. Fig. 8.3 shows the procedures for the fabrication of this device. A mesa 1 μm wide and 370 nm deep is first etched so that the molecular axis of the LQDMs is perpendicular to the long axis of the mesa. The mesa is coated with a thin layer of Al_2O_3 (20 nm) that should prevent charging of the LQDMs from the lateral electrodes and reduce the leakage current. We expect that atomic layer deposition (ALD) will be required for this step because ALD-grown Al_2O_3 is known to effectively passivate surface states and unpin the Fermi level in GaAs-oxide diodes[113, 114]. A pair of lateral electrodes including 8 nm Ti and 100 nm Al are then deposited on the sides of the mesa. The thin Ti layer improves the adhesion of the

metal electrodes to the GaAs. The electrode feature is defined by lithography followed by lift-off or dry etching to open up the top of the mesa and avoid shorts. Ideally the electrodes would terminate at the sides of the mesa to apply a purely lateral electric field, but this approach requires high precision in the layer-to-layer alignment. To relax the processing requirements and ensure a symmetrical structure, we choose a design that allows the electrodes to cover the side walls and top edges of the mesas. The gap between the two lateral electrodes is designed to be 800 nm, 200 nm smaller than the width of the mesa. Bond pads for connection to an external circuit are included in this layer.

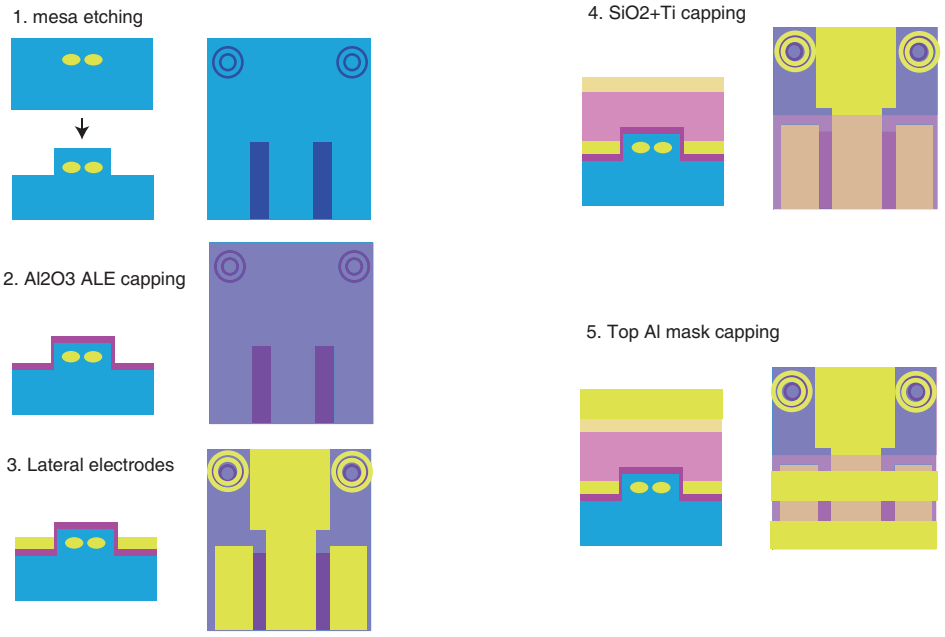

Figure 8.3: Flow chart of the fabrication procedure of the 4-electrode device. The features on this figure are not proportional.

Following the deposition of the lateral electrodes, a SiO_2 insulating layer with a thickness of 300 nm is deposited to cover the mesa and electrode fingers. The vertical electrode and its bonding pad are deposited on top of the SiO_2 insulating layer. The top electrode is composed of a semi-transparent Ti layer (8 nm) completely covering the mesa and a thicker Al layer ($\geq$ 100 nm) with 1 μm gaps oriented perpendicular

to the mesa. This Al mask isolate sections of the mesa for optical measurements of individual LQDMs without needing to align the features during fabrication. The Ti layer guarantees the uniformity of electric fields along the growth direction. As shown on the top of Fig. 8.2, the bonding pads for lateral electrodes are not covered by the insulator layer or subsequent features.

Fig. 8.4 presents device simulations that illustrate the capacity of this device to apply vector electric fields to a LQDM. In order to demonstrate the tolerance of this device to the arbitrary location of the QDMs, we randomly assume the location of the LQDM is 200 nm left of the center of the mesa. In Fig. 8.4 (a, b), a quasi-vertical electric field is applied to the region of the LQDM. In Fig. 8.4 (c, d), a vector electric field containing both lateral and vertical parts is applied. In Fig. 8.4 (e, f), a quasi-lateral electric field is applied. We note that this 4-electrode design is able to apply a maximum lateral electric field 1.2 to 2 times larger than the 3-electrode device. To clearly show the uniformity of the electric field magnitude and direction across the LQDM when a quasi-lateral field is applied, we choose a narrower range for the color scale in Fig. 8.4(f). The figure shows that the lateral field varies from -1 to -1.5 MV/m from the left to the right of the LQDM. This is not a perfectly uniform electric field, but because the direction of the field is parallel to the molecular axis small variations are not likely to substantively alter the ability to tune the relative energy levels of the two QDs, which is the primary function of this lateral field.

8.6 Next Generation 3-terminal Device

One crucial reason why the traditional 3-electrodes device does not work for application of a vector field is that it causes a large leakage current before the vertical electric field is large enough to charge the QDs. On the other hand, if we reduce the area of the electrodes, the top electrode will not be able to cover the QDs and leave apertures small enough for single QD meausurements. One way to solve this problem is developing a two-layer top contact. The bottom layer includes narrow electrodes with minimum area and bonding pads. The top layer is an opaque insulator with

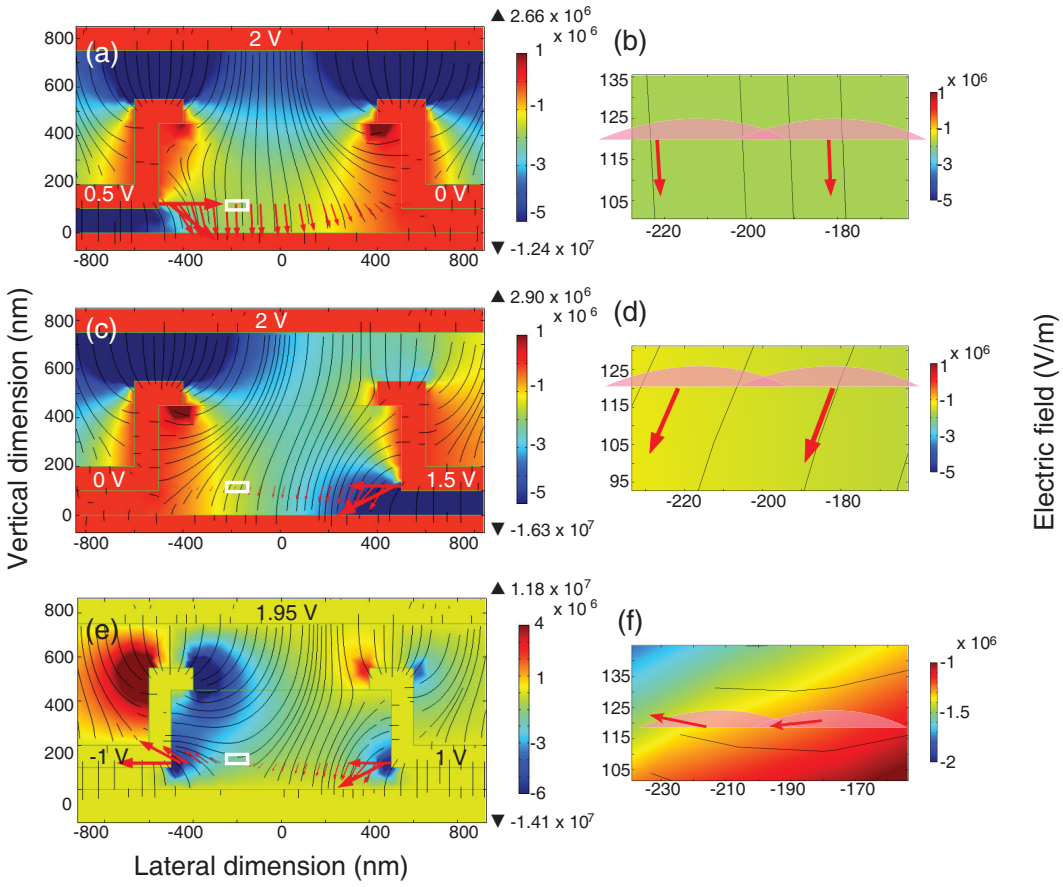

Figure 8.4: Electric field diagram of 4-electrode device simulated by COMSOL. The color shows the intensities of electric fields along the growth direction (a-d) or molecular axis (e, f). The electric field lines are shown in black while the arrows show the direction and magnitude of the electric field at the level of the LQDMs. The right column shows a zoom-in view inside the white rectangular zone on the left column. The pink profiles in the figures in the right column show the cross-sectional view of a single LQDM located inside the white rectangle in the left column.

short stripped patterns perpendicular to the direction of the patterns on the electrodes underneath, which serves as a top mask. Only QDs in the crossover of the top and bottom apertures can be illuminated by the laser. By using this design, a fine alignment during the lithography can be avoided. One suggested design for the top electrodes and mask is schematically shown in Fig. 8.5.

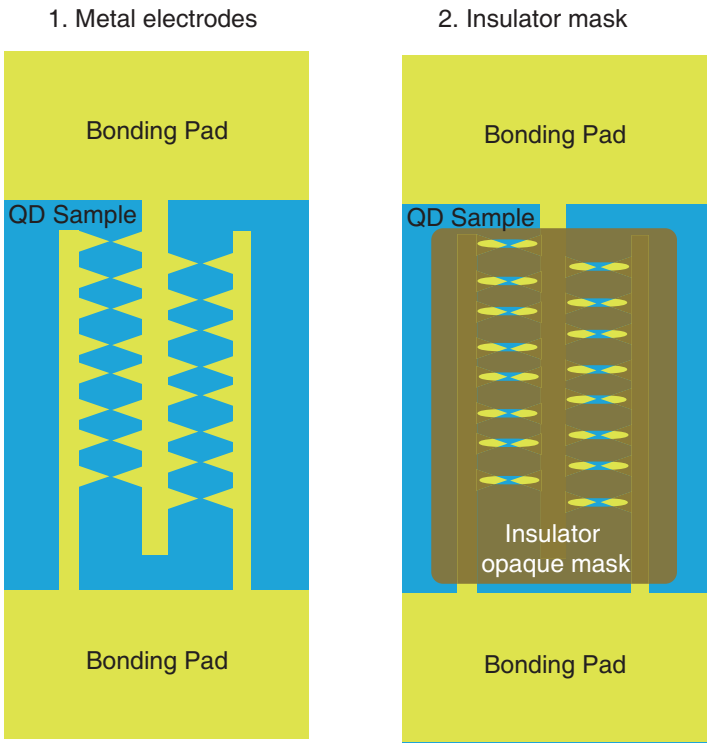

Figure 8.5: Scheme of the top pattern design for the next generation 3-terminal device.

Chapter 9

SUMMARY AND FUTURE WORKS

Our systematic experimental and theoretical analysis of single LQDMs reveals the electronic structure and molecular nature of delocalized states. The observation that the molecular character and symmetry of these electronic states can be controlled with applied magnetic fields, in ways different from what occurs in single QDs or VQDMs, presents new opportunities to design quantum structures for optoelectronic and quantum device applications.

The experimental results of the magneto-spectroscopy of LQDMs, as is introduced in chapter 7, raise several questions for future research. Firstly, the Zeeman splitting has never been observed in the photoluminescence of the first excited states. Secondly, the strength paramagnetic shifts from different emission lines varies substantially. Quantitative theoretical analysis based on the atomic structure of LQDMs might be able to solve these open questions. As we mentioned in section 7.2, the observed difference of Stark shift in ground and excited energy shells is another problem worth to be studied theoretically.

Experimentally, our magnetic-optic cryostat system can apply magnetic field along arbitrary directions to the LQDMs. We can deduce the g tensor by looking at the Zeeman splitting in the photoluminescence of the LQDMs. In our updated system, polarization equipment (e. g.: linear polarizer and liquid crystal variable retarders) can help us to differentiate the spin orientations of emitted photons. The fine-structure splitting, which is closely related to the wavefunction extent of LQDMs, can also be acquired with polarization equipment. The long-term goal for the study of LQDMs is to build up qubits with states being able to be "hand tuning" electrically in two dimensions. To achieve this goal, fabricating the LQDM device introduced in chapter 8

is necessary. The large inter-dot distance and inhomogeneity of LQDMs limited its development as quantum computing devices. It is desired that these problems will be concurred with the development of the QD growth techniques.

BIBLIOGRAPHY

[1] "http://www.youtube.com/watch?v=bnuoym7su4o".

[2] R. Hanson, J. R. Petta, S. Tarucha, and L. M. K. Vandersypen. Spins in few-electron quantum dots. *Reviews of Modern Physics*, 79(4):1217–1265, 2007.

[3] L. A. Ponomarenko, F. Schedin, M. I. Katsnelson, R. Yang, E. W. Hill, K. S. Novoselov, and A. K. Geim. Chaotic dirac billiard in graphene quantum dots. *Science*, 320(5874):356–8, 2008.

[4] A. Pfund, I. Shorubalko, R. Leturcq, and K. Ensslin. Top-gate defined double quantum dots in InAs nanowires. *Applied Physics Letters*, 89(25):252106, 2006.

[5] M. Heiss, Y. Fontana, A. Gustafsson, G. Wust, C. Magen, D. D. O'Regan, J. W. Luo, B. Ketterer, S. Conesa-Boj, A. V. Kuhlmann, J. Houel, E. Russo-Averchi, J. R. Morante, M. Cantoni, N. Marzari, J. Arbiol, A. Zunger, R. J. Warburton, and A. Fontcuberta i Morral. Self-assembled quantum dots in a nanowire system for quantum photonics. *Nat Mater*, 12(5):439–44, 2013.

[6] A. P. Alivisatos. Semiconductor clusters, nanocrystals, and quantum dots. *Science*, 271(5251):933–937, 1996.

[7] Y. Rong, Y. Huo, E. T. Fei, M. Fiorentino, M. R. T. Tan, T. Ochalski, G. Huyet, L. Thylen, M. Chacinski, T. I. Kamins, and J. S. Harris. High speed optical modulation in ge quantum wells using quantum confined stark effect. *Frontiers of Optoelectronics*, 5(1):82, 2012.

[8] M. Ediger, G. Bester, B. D. Gerardot, A. Badolato, P. M. Petroff, K. Karrai, A. Zunger, and R. J. Warburton. Fine structure of negatively and positively charged excitons in semiconductor quantum dots: Electron-hole asymmetry. *Physical Review Letters*, 98:036808, 2007.

[9] A. Sachrajda Z. Wasilewski S. Raymond, S. Studenikin and W. Sheng. Excitonic fock-darwin spectra in quantum dots. *2004 Joint International Meeting*, Quantum Dots and Nanowires, 2004.

[10] E. A. Stinaff, M. Scheibner, A. S. Bracker, I. V. Ponomarev, V. L. Korenev, M. E. Ware, M. F. Doty, T. L. Reinecke, and D. Gammon. Optical signatures of coupled quantum dots. *Science*, 311:636–639, 2006.

[11] "http://en.wikipedia.org/wiki/file:growthmodes.png".

[12] "https://nanohub.org/topics/aqme?version=76".

[13] Q. Xie, A. Madhukar, P. Chen, and N. Kobayashi. Vertically self-organized InAs quantum box islands on GaAs(100). *Physical Review Letters*, 75(13):2542–2545, 1995.

[14] J. Wu, X. Hu, J. Lee, E.-S. Kim, and Z. M. Wang. Epitaxially self-assemblied quantum dot pairs. *Advanced Optical Materials*, 1(3):201–214, 2013.

[15] B. Szafran and F. M. Peeters. Signatures of lateral coupling of double quantum dots in the exciton photoluminescence spectrum. *Phys. Rev. B*, 76:195442, Nov 2007.

[16] L. Wang, A. Rastelli, S. Kiravittaya, M. Benyoucef, and O. G. Schmidt. Self-assembled quantum dot molecules. *ADVANCED MATERIALS*, 21(25-26):2601–2618, JUL 13 2009.

[17] G. Munoz-Matutano, M. Royo, J. I. Climente, J. Canet-Ferrer, D. Fuster, P. Alonso-Gonzalez, I. Fernandez-Martinez, J. Martinez-Pastor, Y. Gonzalez, L. Gonzalez, F. Briones, and B. Alen. Charge control in laterally coupled double quantum dots. *Phys. Rev. B*, 84:041308, Jul 2011.

[18] J. Peng, C. Hermannstadter, M. Witzany, M. Heldmaier, L. Wang, S. Kiravittaya, A. Rastelli, O. G. Schmidt, P. Michler, and G. Bester. Heterogeneous confinement in laterally coupled InGaAs/GaAs quantum dot molecules under lateral electric fields. *Physical Review B*, 81:205315, 2010.

[19] W. Liu. Characterizing and engineering tunable spin functionality inside InAs/GaAs quantum dot molecules (ph. d dissertation). *University of Delaware*, 2013.

[20] A. I. Ekimov and A. A. Onushchenko. Quantum size effect in three-dimensional microscopic semiconductor crystals. *JETP Letters*, 34(6):5, 1981.

[21] R. Rossetti, S. Nakahara, and L. E. Brus. Quantum size effects in the redox potentials, resonance raman spectra, and electronic spectra of cds crystallites in aqueous solution. *The Journal of Chemical Physics*, 79(2), 1983.

[22] J. M. Caruge, J. E. Halpert, V. Wood, V. Bulovic, and M. G. Bawendi. Colloidal quantum-dot light-emitting diodes with metal-oxide charge transport layers. *Nat Photon*, 2(4):247–250, 2008. 10.1038/nphoton.2008.34.

[23] G. I. Koleilat, L. Levina, H. Shukla, S. H. Myrskog, S. Hinds, A. G. Pattantyus-Abraham, and E. H. Sargent. Efficient, stable infrared photovoltaics based on solution-cast colloidal quantum dots. *ACS Nano*, 2(5):833–840, 2008.

[24] G. Konstantatos and E. H. Sargent. Solution-processed quantum dot photodetectors. *Proceedings of the IEEE*, 97(10):1666–1683, Oct 2009.

[25] M. Dahan, T. Laurence, F. Pinaud, D. S. Chemla, A. P. Alivisatos, M. Sauer, and S. Weiss. Time-gated biological imaging by use of colloidal quantum dots. *Opt. Lett.*, 26(11):825–827, Jun 2001.

[26] F. Hetsch, N. Zhao, S. V. Kershaw, and A. L. Rogach. Quantum dot field effect transistors. *Materials Today*, 16(9):312 – 325, 2013.

[27] B. O. Dabbousi, J. Rodriguez-Viejo, F. V. Mikulec, J. R. Heine, H. Mattoussi, R. Ober, K. F. Jensen, and M. G. Bawendi. (cdse)zns core/shell quantum dots: Synthesis and characterization of a size series of highly luminescent nanocrystallites. *The Journal of Physical Chemistry B*, 101(46):9463–9475, 1997.

[28] G. J. Schinner, J. Repp, E. Schubert, A. K. Rai, D. Reuter, A. D. Wieck, A. O. Govorov, A. W. Holleitner, and J. P. Kotthaus. Single exciton emission from gate-defined quantum dots, 2012.

[29] D. Subramaniam, F. Libisch, Y. Li, C. Pauly, V. Geringer, R. Reiter, T. Mashoff, M. Liebmann, J. Burgdorfer, C. Busse, T. Michely, R. Mazzarello, M. Pratzer, and M. Morgenstern. Wave-function mapping of graphene quantum dots with soft confinement. *Physical Review Letters*, 108(4), 2012.

[30] B. Trauzettel, D. V. Bulaev, D. Loss, and G. Burkard. Spin qubits in graphene quantum dots. *Nature Physics*, 3(3):192–196, 2007.

[31] K. Tachibana, T. Someya, and Y. Arakawa. Nanometer-scale ingan self-assembled quantum dots grown by metalorganic chemical vapor deposition. *Applied Physics Letters*, 74(3):383, 1999.

[32] S. G. Li, Q. Gong, C. F. Cao, X. Z. Wang, J. Y. Yan, Y. Wang, and H. L. Wang. The developments of inp-based quantum dot lasers. *Infrared Physics and Technology*, 60:216–224, 2013.

[33] A. Greilich, Sophia E. Economou, S. Spatzek, D. R. Yakovlev, D. Reuter, A. D. Wieck, T. L. Reinecke, and M. Bayer. Ultrafast optical rotations of electron spins in quantum dots. *Nature Physics*, 5(4):262–266, 2009.

[34] R. J. Warburton. Single spins in self-assembled quantum dots. *NATURE MATERIALS*, 12(6):483–493, JUN 2013.

[35] B. D. Gerardot, D. Brunner, P. A. Dalgarno, P. Ohberg, S. Seidl, M. Kroner, K. Karrai, N. G. Stoltz, P. M. Petroff, and R. J. Warburton. Optical pumping of a single hole spin in a quantum dot. *Nature*, 451(7177):441–4, 2008.

[36] S. E. Economou, J. I. Climente, A. Badolato, A. S. Bracker, D. Gammon, and M. F. Doty. Scalable qubit architecture based on holes in quantum dot molecules. *Physical Review B*, 86(8), 2012.

[37] L. Muller-Kirsch, R. Heitz, A. Schliwa, O. Stier, D. Bimberg, H. Kirmse, and W. Neumann. Many-particle effects in type ii quantum dots. *Applied Physics Letters*, 78(10):1418, 2001.

[38] J. Shumway, A. Williamson, Alex Zunger, A. Passaseo, M. DeGiorgi, R. Cingolani, M. Catalano, and P. Crozier. Electronic structure consequences of in/ga composition variations in self-assembled InxGa1-xAs/GaAs alloy quantum dots. *Physical Review B*, 64(12), 2001.

[39] E. Leobandung, L. Guo, Y. Wang, and S. Y. Chou. Observation of quantum effects and coulomb blockade in silicon quantum-dot transistors at temperatures over 100 k. *Applied Physics Letters*, 67(7):938, 1995.

[40] E. J. Gansen, M. A. Rowe, M. B. Greene, D. Rosenberg, T. E. Harvey, M. Y. Su, R. H. Hadfield, S. W. Nam, and R. P. Mirin. Photon-number-discriminating detection using a quantum-dot, optically gated, field-effect transistor. *Nature Photonics*, 1(10):585–588, 2007.

[41] J. D. Mar, X. L. Xu, J. S. Sandhu, A. C. Irvine, M. Hopkinson, and D. A. Williams. Electrical control of fine-structure splitting in self-assembled quantum dots for entangled photon pair creation. *Applied Physics Letters*, 97(22):221108, 2010.

[42] M. Ediger, G. Bester, A. Badolato, P. M. Petroff, K. Karrai, A. Zunger, and R. J. Warburton. Peculiar many-body effects revealed in the spectroscopy of highly charged quantum dots. *Nature Physics*, 3:774–779, 2007.

[43] M. F. Doty, M. Scheibner, I. V. Ponomarev, E. A. Stinaff, A. S. Bracker, V. L. Korenev, T. L. Reinecke, and D. Gammon. Electrically tunable g factors in quantum dot molecular spin states. *Physical Review Letters*, 97:197202, 2006.

[44] M. Bayer, G. Ortner, O. Stern, A. Kuther, A. A. Gorbunov, A. Forchel, P. Hawrylak, S. Fafard, K. Hinzer, T. L. Reinecke, S. N. Walck, J. P. Reithmaier, F. Klopf, and F. Schafer. Fine structure of neutral and charged excitons in self-assembled In(Ga)As/(Al)GaAs quantum dots. *Physical Review B*, 65:195315, 2002.

[45] C. Schulhauser, D. Haft, R. Warburton, K. Karrai, A. Govorov, A. Kalameitsev, A. Chaplik, W. Schoenfeld, J. Garcia, and P. Petroff. Magneto-optical properties of charged excitons in quantum dots. *Physical Review B*, 66(19), 2002.

[46] M. F. Tsai, H. Lin, C. H. Lin, S. D Lin, S. Y. Wang, M. C. Lo, S. J. Cheng, M. C. Lee, and W. H. Chang. Diamagnetic response of exciton complexes in semiconductor quantum dots. *Physical Review Letters*, 101(26), 2008.

[47] M. Bayer, M. Korkusinski, P. Hawrylak, T. Gutbrod, M. Michel, and A. Forchel. Optical detection of the aharonov-bohm effect on a charged particle in a nanoscale quantum ring. *Physical Review Letters*, 90(18), 2003.

[48] I. Sellers, V. Whiteside, I. Kuskovsky, A. Govorov, and B. McCombe. Aharonov-bohm excitons at elevated temperatures in type-ii znte/znse quantum dots. *Physical Review Letters*, 100(13), 2008.

[49] H. J. Krenner, M. Sabathil, E. C. Clark, A. Kress, D. Schuh, M. Bichler, G. Abstreiter, and J. J. Finley. Direct observation of controlled coupling in an individual quantum dot molecule. *Physical Review Letters*, 94:57402, 2005.

[50] K. C. Wijesundara, J. E. Rolon, S. E. Ulloa, A. S. Bracker, D. Gammon, and E. A. Stinaff. Tunable exciton relaxation in vertically coupled semiconductor InAs quantum dots. *Physical Review B*, 84(8), 2011.

[51] M. Scheibner, M. F. Doty, I. V. Ponomarev, A. S. Bracker, E. A. Stinaff, V. L. Korenev, T. L. Reinecke, and D. Gammon. Spin fine structure of optically excited quantum dot molecules. *Phys. Rev. B*, 75(24):245318, 2007.

[52] A. S. Bracker, M. Scheibner, M. F. Doty, E. A. Stinaff, I. V. Ponomarev, J. C. Kim, L. J. Whitman, T. L. Reinecke, and D. Gammon. Engineering electron and hole tunneling with asymmetric InAs quantum dot molecules. *Applied Physics Letters*, 89:233110, 2006.

[53] D. Granados and Jorge M. Garcia. In(Ga)As self-assembled quantum ring formation by molecular beam epitaxy. *Applied Physics Letters*, 82(15):2401, 2003.

[54] J. H. Lee, Z. M. Wang, N. W. Strom, Y. I. Mazur, and G. J. Salamo. InGaAs quantum dot molecules around self-assembled GaAs nanomound templates. *Applied Physics Letters*, 89:202101, 2006.

[55] G. Bester, J. Shumway, and A. Zunger. Theory of excitonic spectra and entanglement engineering in dot molecules. *Physical Review Letters*, 93:47401, 2004.

[56] M. F. Doty, M. Scheibner, A. S. Bracker, I. V. Ponomarev, T. L. Reinecke, and D. Gammon. Optical spectra of doubly charged quantum dot molecules in electric and magnetic fields. *Physical Review B*, 78:115316, 2008.

[57] B Szafran and F M Peeters. Signatures of lateral coupling of double quantum dots in the exciton photoluminescence spectrum. *Physical Review B*, 76:195442, 2007.

[58] L. Goldstein, F. Glas, J. Y. Marzin, M. N. Charasse, and G. Le Roux. Growth by molecular beam epitaxy and characterization of InAs/GaAs strained-layer superlattices. *Applied Physics Letters*, 47(10):1099, 1985.

[59] M. Nomura, N. Kumagai, S. Iwamoto, Y. Ota, and Y. Arakawa. Laser oscillation in a strongly coupled single-quantum-dotcnanocavity system. *Nature Physics*, 6(4):279–283, 2010.

[60] C. L. Salter, R. M. Stevenson, I. Farrer, C. A. Nicoll, D. A. Ritchie, and A. J. Shields. An entangled-light-emitting diode. *Nature*, 465(7298):594–7, 2010. Salter, C L Stevenson, R M Farrer, I Nicoll, C A Ritchie, D A Shields, A J eng Research Support, Non-U.S. Gov't England 2010/06/04 06:00 Nature. 2010 Jun 3;465(7298):594-7. doi: 10.1038/nature09078.

[61] A. D. Stiff, S. Krishna, P. Bhattacharya, and S. Kennerly. High-detectivity, normal-incidence, mid-infrared InAs/GaAs quantum-dot detector operating at 150 k. *Applied Physics Letters*, 79(3), 2001.

[62] Y. Ducommun, M. Kroutvar, J. J. Finley, M. Bichler, A. Zrenner, and G. Abstreiter. Dynamics of optically stored charges in InGaAs quantum dots. *Physica E: Low-dimensional Systems and Nanostructures*, 21(2-4):886–891, 2004.

[63] D. Press, T. D. Ladd, B. Zhang, and Y. Yamamoto. Complete quantum control of a single quantum dot spin using ultrafast optical pulses. *Nature*, 456(7219):218–21, 2008. Press, David Ladd, Thaddeus D Zhang, Bingyang Yamamoto, Yoshihisa eng Research Support, Non-U.S. Gov't Research Support, U.S. Gov't, Non-P.H.S. England 2008/11/14 09:00 Nature. 2008 Nov 13;456(7219):218-21. doi: 10.1038/nature07530.

[64] Z. R. Wasilewski, S. Fafard, and J. P. McCaffrey. Size and shape engineering of vertically stacked self-assembled quantum dots. *Journal of Crystal Growth*, 201-002(0):1131 – 1135, 1999.

[65] M. F. Doty, J. I. Climente, A. Greilich, M. Yakes, A. S. Bracker, and D Gammon. Opportunities for single hole-spin control using delocalized states of quantum dot molecules. *Journal of Physics: Conference Series*, 245, 2010.

[66] M. Bayer, P. Hawrylak, K. Hinzer, S. Fafard, M. Korkusinski, Z. R. Wasilewski, O. Stern, and A. Forchel. Coupling and entangling of quantum states in quantum dot molecules. *Science*, 291:451–453, 2001.

[67] W. Liu, S. Sanwlani, R. Hazbun, J. Kolodzey, A. S. Bracker, D. Gammon, and M. F. Doty. *In situ* tunable g factor for a single electron confined inside an InAs quantum dot molecule. *Phys. Rev. B*, 84:121304, Sep 2011.

[68] D. Kim, S. G. Carter, A. Greilich, A. S. Bracker, and D. Gammon. Ultrafast optical control of entanglement between two quantum-dot spins. *Nature Physics*, 7(3):223–229, 2010.

[69] A. Greilich, S. G. Carter, D. Kim, A. S. Bracker, and D. Gammon. Optical control of one and two hole spins in interacting quantum dots. *Nature Photonics*, 5(11):702–708, 2011.

[70] E. Zallo, R. Trotta, V. Kpek, Y. H. Huo, P. Atkinson, F. Ding, T. ikola, A. Rastelli, and O. G. Schmidt. Strain-induced active tuning of the coherent tunneling in quantum dot molecules. *Physical Review B*, 89(24), 2014.

[71] E. Zallo, P. Atkinson, A. Rastelli, and O. G. Schmidt. Controlling the formation of quantum dot pairs using nanohole templates. *Journal of Crystal Growth*, 338(1):232–238, 2012.

[72] L. Wang, A. Rastelli, S. Kiravittaya, P. Atkinson, F. Ding, C. C. Bof Bufon, C. Hermannstadter, M. Witzany, G. J. Beirne, P. Michler, and O. G. Schmidt. Towards deterministically controlled InGaAs/GaAs lateral quantum dot molecules. *New Journal of Physics*, 10(4):045010, 2008.

[73] E. Zallo, P. Atkinson, L. Wang, A. Rastelli, and O. G. Schmidt. Epitaxial growth of lateral quantum dot molecules. *physica status solidi (b)*, 249(4):702–709, 2012.

[74] J. M. Garca, T. Mankad, P. O. Holtz, P. J. Wellman, and P. M. Petroff. Electronic states tuning of InAs self-assembled quantum dots. *Applied Physics Letters*, 72(24):3172, 1998.

[75] V. P. LaBella, H. Yang, D. W. Bullock, P. M. Thibado, Peter Kratzer, and Matthias Scheffler. Atomic structure of the GaAs(001)-(2x4) surface resolved using scanning tunneling microscopy and first-principles theory. *Phys. Rev. Lett.*, 83:2989–2992, Oct 1999.

[76] R. Songmuang, S. Kiravittaya, and O. G. Schmidt. Formation of lateral quantum dot molecules around self-assembled nanoholes. *Applied Physics Letters*, 82:2982, 2003.

[77] S. Folsch, J. Martinez-Blanco, J. Yang, K. Kanisawa, and S. C. Erwin. Quantum dots with single-atom precision. *Nat Nano*, 9(7):505–508, 2014.

[78] G. J. Beirne, C Hermannstadter, L Wang, A Rastelli, OG Schmidt, and P Michler. Quantum light emission of two lateral tunnel-coupled (In,Ga)As/GaAs quantum dots controlled by a tunable static electric field. *PHYSICAL REVIEW LETTERS*, 96(13), APR 7 2006.

[79] M. Royo, J. I. Climente, and J. Planelles. Emission spectrum of quasiresonant laterally coupled quantum dots. *PHYSICAL REVIEW B*, 84(23), DEC 21 2011.

[80] S. Fafard, Z. Wasilewski, C. Allen, D. Picard, M. Spanner, J. McCaffrey, and P. Piva. Manipulating the energy levels of semiconductor quantum dots. *Phys. Rev. B*, 59:15368–15373, Jun 1999.

[81] F. Findeis, M. Baier, E. Beham, A. Zrenner, and G. Abstreiter. Photocurrent and photoluminescence of a single self-assembled quantum dot in electric fields. *Applied Physics Letters*, 78(19):2958, 2001.

[82] T. S. Sosnowski, T B Norris, H Jiang, J Singh, K Kamath, and P Bhattacharya. Rapid carrier relaxation in $In_{0.4}Ga_{0.6}As/GaAs$ quantum dots characterized by differential transmission spectroscopy. *Physical Review B*, 57(16):R9423–R9426, 1998.

[83] O. Stier, M. Grundmann, and D. Bimberg. Electronic and optical properties of strained quantum dots modeled by 8-band k.p theory. *Physical Review B*, 59(8):5688, 1999.

[84] J. Peng and G. Bester. Charged excitons and biexcitons in laterally coupled (in,ga)as quantum dots. *Physical Review B Phys. Rev. B PRB*, 82(23):235314, 2010.

[85] J. J. Finley, M. Sabathil, P. Vogl, G. Abstreiter, R. Oulton, A. I. Tartakovskii, D. J. Mowbray, M. S. Skolnick, S. L. Liew, A. G. Cullis, and M. Hopkinson. Quantum-confined Stark shifts of charged exciton complexes in quantum dots. *PHYSICAL REVIEW B*, 70(20), NOV 2004.

[86] P. Dalgarno, J. Smith, J. McFarlane, B. Gerardot, K. Karrai, A. Badolato, P. Petroff, and R. Warburton. Coulomb interactions in single charged self-assembled quantum dots: Radiative lifetime and recombination energy. *Physical Review B*, 77(24), 2008.

[87] M. Baier, F. Findeis, A. Zrenner, M. Bichler, and G. Abstreiter. Optical spectroscopy of charged excitons in single quantum dot photodiodes. *PHYSICAL REVIEW B*, 64(19), NOV 15 2001.

[88] X. Zhou, S. Sanwlani, W. Liu, J. H. Lee, Zh. M. Wang, G. Salamo, and M. F. Doty. Spectroscopic signatures of many-body interactions and delocalized states in self-assembled lateral quantum dot molecules. *PHYSICAL REVIEW B*, 84(20), NOV 11 2011.

[89] M. F. Doty, M. E. Ware, E. A. Stinaff, M. Scheibner, A. S. Bracker, I. V. Ponomarev, S. C. Badescu, V. L. Korenev, T. L. Reinecke, and D. Gammon. Spin interactions in InAs quantum dots and molecules. *Physica Status Solidi B-Basic Solid State Physics*, 243:3859–3863, 2006.

[90] C. Hermannstadter, G. J. Beirne, M. Witzany, M. Heldmaier, J. Peng, G. Bester, L. Wang, A. Rastelli, O. G. Schmidt, and P. Michler. Influence of the charge carrier tunneling processes on the recombination dynamics in single lateral quantum dot molecules. *Physical Review B*, 82:085309, 2010.

[91] J. I. Climente, M. Korkusinski, G. Goldoni, and P. Hawrylak. Theory of valence band holes as luttinger spinors in vertically coupled quantum dots. *Physical Review B*, 78:115323, 2008.

[92] M. F. Doty, J. I. Climente, A. Greilich, M. Yakes, A. S. Bracker, and D. Gammon. Hole-spin mixing in InAs quantum dot molecules. *Physical Review B*, 81:035308, 2010.

[93] J. Planelles, J I Climente, F. Rajadell, M F Doty, A. S. Bracker, and D. Gammon. Effect of strain and variable mass on the formation of antibonding hole ground states in InAs quantum dot molecules. *Physical Review B*, 82(15):155307, 2010.

[94] X. R. Zhou, J. H. Lee, G. J. Salamo, M. Royo, J. I. Climente, and M. F. Doty. Coulomb interaction signatures in self-assembled lateral quantum dot molecules. *Phys. Rev. B*, 87:125309, Mar 2013.

[95] S. Brown, T. Kennedy, D. Gammon, and E. Snow. Spectrally resolved overhauser shifts in single GaAs/$Al_xGa_{1-x}As$ as quantum dots. *Physical Review B*, 54(24):R17339–R17342, 1996.

[96] H. Kim, T. C. Shen, D. Sridharan, G. S. Solomon, and E. Waks. Magnetic field tuning of a quantum dot strongly coupled to a photonic crystal cavity. *Applied Physics Letters*, 98(9):091102, 2011.

[97] S. Raymond, S. Studenikin, A. Sachrajda, Z. Wasilewski, S. Cheng, W. Sheng, P. Hawrylak, A. Babinski, M. Potemski, G. Ortner, and M. Bayer. Excitonic energy shell structure of self-assembled InGaAs/GaAs quantum dots. *Physical Review Letters*, 92(18), 2004.

[98] F. Gagel and K. Maschke. Finite-difference approach to edge-state transport in quantum wires and multiterminal devices. *Phys. Rev. B*, 52:2013–2019, Jul 1995.

[99] Y. Sidor, B. Partoens, F. M. Peeters, N. Schildermans, M. Hayne, V. V. Moshchalkov, A. Rastelli, and O. G. Schmidt. High-field magnetoexcitons in unstrained GaAs/al_xga_1-xAs quantum dots. *Phys. Rev. B*, 73:155334, Apr 2006.

[100] J. I. Climente and J. Planelles. Characteristic molecular properties of one-electron double quantum rings under magnetic fields. *Journal of Physics-Condensed Matter*, 20(3), 2008. 259EW Times Cited:5 Cited References Count:47.

[101] U. Hohenester and E. Molinari. Excitonic and biexcitonic states in semiconductor quantum dots. *physica status solidi (a)*, 178(1):277–282, 2000.

[102] J. van Bree, A. Yu Silov, P. M. Koenraad, M. E. Flatt, and C. E. Pryor. g factors and diamagnetic coefficients of electrons, holes, and excitons in InAs/inp quantum dots. *Physical Review B*, 85(16), 2012.

[103] N. A. J. M. Kleemans, J. van Bree, M. Bozkurt, P. J. van Veldhoven, P. A. Nouwens, R. Notzel, A. Y. Silov, P. M. Koenraad, and M. E. Flatte. Size-dependent exciton g factor in self-assembled InAs/inp quantum dots. *Physical Review B*, 79(4), 2009. 401YB Times Cited:13 Cited References Count:32.

[104] X. Zhou and M. Doty. Design of 4-electrode optical device for application of vector electric fields to self-assembled quantum dot complexes. *Journal of Applied Physics*, 116(16):163101, 2014.

[105] W. Liu, A. S. Bracker, D. Gammon, and Matthew F. Doty. Dynamic hole trapping in InAs/AlGaAs/InAs quantum dot molecules. *Phys. Rev. B*, 87:195308, May 2013.

[106] J. D. Mar, X. L. Xu, J. J. Baumberg, A. C. Irvine, C. Stanley, and D. A. Williams. Voltage-controlled electron tunneling from a single self-assembled quantum dot embedded in a two-dimensional-electron-gas-based photovoltaic cell. *Journal of Applied Physics*, 110(5):053110, 2011.

[107] M. Kaniber, M. F. Huck, K. Muller, E. C. Clark, F. Troiani, M. Bichler, H. J. Krenner, and J. J. Finley. Electrical control of the exciton-biexciton splitting in self-assembled InGaAs quantum dots. *Nanotechnology*, 22(32):325202, 2011.

[108] M. M. Vogel, S. M. Ulrich, R. Hafenbrak, P. Michler, L. Wang, A. Rastelli, and O. G. Schmidt. Influence of lateral electric fields on multiexcitonic transitions and fine structure of single quantum dots. *Applied Physics Letters*, 91(5):051904, 2007.

[109] A. J. Bennett, M. A. Pooley, R. M. Stevenson, M. B. Ward, R. B. Patel, A. Boyer de la Giroday, N. Skold, I. Farrer, C. A. Nicoll, D. A. Ritchie, and A. J. Shields. Electric-field-induced coherent coupling of the exciton states in a single quantum dot. *Nature Physics*, 6(12):947–950, 2010.

[110] J. M. Woodall, G. D. Pettit, T. N. Jackson, C. Lanza, K. L. Kavanagh, and J. W. Mayer. Fermi-level pinning by misfit dislocations at GaAs interfaces. *Phys. Rev. Lett.*, 51:1783–1786, Nov 1983.

[111] S. Tiwari, S. L. Wright, and J Batey. Unpinned GaAs mos capacitors and transistors. *IEEE ELECTRON DEVICE LETTERS*, 9(9):488–490, SEP 1988.

[112] J. H. Lee, Z. M. Wang, V. G. Dorogan, Y. I. Mazur, and G. J. Salamo. Evolution of various nanostructures and preservation of self-assembled InAs quantum dots during GaAs capping. *IEEE Transactions on Nanotechnology*, 9(2):149, 2010.

[113] P. D. Ye, G. D. Wilk, B. Yang, J. Kwo, S. N. G. Chu, S. Nakahara, H. J. L. Gossmann, J. P. Mannaerts, M. Hong, K. K. Ng, and J. Bude. GaAs metal-oxide-semiconductor field-effect transistor with nanometer-thin dielectric grown by atomic layer deposition. *Applied Physics Letters*, 83(1):180, 2003.

[114] Y. Xuan, H. C. Lin, and P. D. Ye. Simplified surface preparation for gaas passivation using atomic layer-deposited high-kappa dielectrics. *IEEE TRANSACTIONS ON ELECTRON DEVICES*, 54(8):1811–1817, AUG 2007.

[115] A. G. Baca, F. Ren, J. C. Zolper, R. D. Briggs, and S. J. Pearton. A survey of ohmic contacts to iii-v compound semiconductors. *Thin Solid Films*, 308-309:599–606, 1997.

Appendix A

DEVICE FABRICATION RECIPE OF LQDMS DIODE

A.1 Lift-off Recipe for 1-micron Interdigitated Pattern

Solvent clean: Mount wafer on spinner. Spin at 3000 rpm with ramp 1000 rpm for 45 seconds. Spray Acetone, Methanol and iso-propanol for 10 seconds respecticvely.

Coat resist:

Stop the spinner, drip NR9-1000PY photoresist to fully cover the surface of the wafer.

Spin at different rates to get a flat surface of photoresist:

- Spin at 75 rpm with ramp 500 rps for 6 seconds.

- Spin at 5000 rpm with ramp 1000 rps for 40 seconds.

Soft bake at 100 C for 60 seconds.

Expose pattern with dose 70-85 mW/ cm^2 in the channel with wavelength= 365 nm.

Hard bake at 100 C for 60 seconds.

Develop pattern in the solution of DI water: RD6= 1:3 for 9-10 s. Note: do not shake the wafer in the solution. Flush the sample with water after exposure.

Metal coating: 8 nm of Ti and 120 nm of Al are deposited on the patterned top surface of the sample. The Ti layer is deposited first for adhension and the Al is coated as opaque mask and electrodes including bonding pads. Ideally, electron beam evaporator is used to deposit metal thin films because the metal hits the sample vertically and the lift-off process is relative easy. Physical vapor deposition (PVD) is another possible approach when the metal film is thin and feature size is relative large (over 10 μms).

Lift off: soak the sample in IPA or acetone overnight to get the best pattern. If necessary, use ultrasonic cleaner to accelerate the lift off process.

A.2 Ohmic Back Contact

Two different recipes for electron beam evaporation of Ohmic back contact have been used in our sample preparation and both work very well in our n-doped GaAs substrates. Recipe I consumes less gold and recipe II contains fewer steps. To achieve an Ohmic contact with good quality, rapid thermal annealing (RTA) is required in most recipes.[115] A high annealing temperature might cause the redistribution of the materials and lead to the change of the QDs' geometry and energy structure. Defects introduced by annealing will also cause the decrease of the photon emission intensity. Therefore, it is necessary to avoid any RTA at a temperature higher than the anneal temperature during MBE growth. For the recipes provided below, a 30 sec annealing in an RTA at 410 C is used.

Table A.1: Recipe I: Order and thickness of materials for Ohmic back contact

Sequence	Matals	Thickenss (nm)
1	Ni	5
2	Ge	17
3	Au	33
4	Ni	15
5	Au	20

Table A.2: Recipe II: Order and thickness of materials for Ohmic back contact

Sequence	Matals	Thickenss (nm)	Deposition rate (A/s)
1	Ni	5	0.1
2	Ge	17	0.5
3	Au	200	1.2

A.3 Mounting and Wire Bonding

1. Using conductive epoxy to stick the backside of the sample onto the sample holder.

2. Heat the sample in 120 C oven for 30 minutes.

3. Take out the sample and wait until cool down. Observe the sample under an optical microscope. Use a pin to soak the well-mixed conductive epoxy. Dip the epoxy drop on a bonding pad on the sample and a gold pad on the sample holder. Make sure that there is a small bulk of epoxy on both pads.

4. Cut a section of gold wire with appropriate length and use the pin to carefully transfer this gold wire section to connect the two epoxy bulks. Both sides of the gold wire should buried in epoxy.

5. Dip a larger bulk of conductive epoxy on the corner of the sample holder to short one pad with the gold substrate of the holder.

6. Heat the sample to 120 C in the oven for another 30 minutes.

7. Connect the two feet that are being used on the sample header to the electric leads. Check the IV curve to see if it shows a diode curve.

Appendix B

OPERATION PROCEDURE FOR THE CRYOSTAT SYSTEMS

B.1 Measuring Laser Power Densities Incident on the Sample

It is very important to know the laser power density that is actually incident on the QDs to acquire information such as quantum yield. However, it is difficult to measure the laser power at the position of the LQDMs system, which is inside the cold finger of the closed-cycle cryostat system. To figure out the actual laser power density that excites the QDs, we have done a series of rough measurements on the different parts of the PL system. Here is a summary of our measurements.

- When the laser power shown by the power stablizer is 176 mW, the laser power measured at the position of the NIR objective is 37.5 mW. Therefore, the main optical path (not including the objective) will reduce the laser power by 4.7 times.

- The laser powers measured before and after the objective are 172 mW and 60 mW, respectively. The objective will reduce the laser power by 2.9 times.

- The laser powers measured before and after the quartz window on the cold-finger of the cryostat are 340 mW and 270 mW. The quartz window will reduce the laser power by 1.3 times.

- Overall, the ratio between the laser power shown on the power stablizer and the actual laser power hitting the sample should be 17.8:1. The diameter of the laser spot is usually around 10 um. It can be calculated that when the laser power is recorded as 1 mW, the actual laser power density hit on the sample surface should be 71.3 W/ cm^2.

It is impossible to measure the scattering caused by the electrodes on the surface and other layer structures above the QDs and we have to neglect it in our discussion.

For the laser power density in the magneto-cryostat system, the meausrement is even harder and is unlikely to be done without dissassembling the whole system. We simply compare the laser power between the two systems at the point the PL intensities of ground and first states cross each other. Since the optical systems reduce the PL intensities in ground and excited shells by the same percent, it can be deduced that this comparison identifies comparable laser power densities for the two systems.

B.2 General SOP for the Closed-cycle Cryostat

B.2.1 Cooling Down

1. Seal the cold-finger of the cryostat by using vacuum grease. Tightly screw on the cap of the chamber. Check all the wires and tube connections between the compressor, the cool pac and the expander.

2. Connect the pump to the closed cycle cryostat and turn it on, using only the rough pump for a few seconds.

3. Slowly open the valve while the pump is running until the valve is fully opened.

4. Purge the close cycle cryostat with helium gas: (you only need to do this if you have made a sample change or the instrument has been unused for a very long time)

a. Open all the valves for the helium gas, set the pressure to 1.6psi. b. Wait 10 seconds, and then decrease the pressure to 0.25 psi, open the vent valve on the cryostat. c. Repeated 4-5 times.

5. Turn on the cool pac and then turn on the compressor. Set the helium gas flow at the bellows to 0.6 psi.

6. Pump until pressure reaches 1E-1, then turn on the turbo pump.

7. Wait for a few minutes. Pump until pressure reaches 4E-4, then turn on the coolpac and the compressor, in that order. Look at the temperature sensor, see the temperature decrease.

7. When the temperature goes down to 150K, close the pumping valve and shut down the pump. Make sure the temperature is still decreasing at the same rate before disconnecting the turbo pump.

B.2.2 Shut off

When shutting off the whole system, first turn off the compressor, then the cool pac. The temperature will increase after that. Before changing the sample:

1. Shut off the whole system; wait until the whole system is back to room temperature.

2. Open the main valve of the cryostat to balance the air pressure inside and outside the cryostat.

3. Open the main cap of the chamber.

B.2.3 Common Questions

Q: What should I do in power failure?

A: Make sure the switches for the compressor and cool pac are turned off. If the duration of the power loss is very short (less than 10 minutes), we can turn the cool pac and compressor back on when the power supply is restored.

Q: When should I shut-down the whole system and call for maintenance?

A: 1) When water is leaking from the tubes connect compressor and coolpac.

2) When the compressor keeps turning on and off back and forth by itself: this means the coolpac is not functioning correctly and the compressor is turning off as it detects over-heating.

Q: What should I check if the system is not working properly?

A: Check Sakai- resource for manuals.

Appendix C

REPRINT PERMISSION LIST

Permissions for reprinting figures published in journals were provided by the respective publishers. A list for all the permissions is attached.

Copyright Clearance Center RightsLink®

My Orders My Library My Profile

Welcome zxinr@udel.edu Log out | Help

My Orders > Orders > All Orders

My Orders

Orders Billing History Payable Invoices

SEARCH

Date Range: From 12-Nov-2014 To 12-Feb-2015

Order Number: Go

View: All Pending Offer Ready Completed Canceled Denied Credited Filter

Results: 1-12 of 12

Order Date	Article Title	Publication	Type Of Use	Order Status	Order Number
12-Feb-2015	Design of 4-electrode optical device for application of vector electric fields to self-assembled quantum dot complexes	Journal of Applied Physics	Thesis/Dissertation	Completed	3566710557127
12-Feb-2015	Epitaxially Self-Assemblied Quantum Dot Pairs	Advanced Optical Materials	Dissertation/Thesis	Completed	3566710062889
12-Feb-2015	Optical Signatures of Coupled Quantum Dots	Science	Thesis / Dissertation	Completed	3566701427759
12-Feb-2015	Vertically Self-Organized InAs Quantum Box Islands on GaAs(100)	Physical Review Letters	Thesis/Dissertation	Completed	3566701296817
12-Feb-2015	Optical Signatures of Coupled Quantum Dots	Science	Thesis / Dissertation	Completed	3566700570434
12-Feb-2015	Peculiar many-body effects revealed in|[nbsp]|the|[nbsp]|spectroscopy of highly charged quantum|[nbsp]|dots	Nature Physics	reuse in a dissertation / thesis	Completed	3566700223422
12-Feb-2015	High speed optical modulation in Ge quantum wells using quantum confined stark effect	Frontiers of Optoelectronics	Thesis/Dissertation	Completed	3566691402716
12-Feb-2015	Semiconductor Clusters, Nanocrystals, and Quantum Dots	Science	Thesis / Dissertation	Completed	3566691181024
12-Feb-2015	Self-assembled quantum dots in a nanowire system for quantum photonics	Nature Materials	reuse in a dissertation / thesis	Completed	3566691039574
12-Feb-2015	Top-gate defined double quantum dots in InAs nanowires	Applied Physics Letters	Thesis/Dissertation	Completed	3566690734357
12-Feb-2015	Chaotic Dirac Billiard in Graphene Quantum Dots	Science	Thesis / Dissertation	Completed	3566681274572
12-Feb-2015	Spins in few-electron quantum dots	Reviews of Modern Physics	Thesis/Dissertation	Completed	3566680883053